INFORMATION TO USERS

This manuscript has been reproduced from the microfilm master. UMI films the text directly from the original or copy submitted. Thus, some thesis and dissertation copies are in typewriter face, while others may be from any type of computer printer.

The quality of this reproduction is dependent upon the quality of the copy submitted. Broken or indistinct print, colored or poor quality illustrations and photographs, print bleedthrough, substandard margins, and improper alignment can adversely affect reproduction.

In the unlikely event that the author did not send UMI a complete manuscript and there are missing pages, these will be noted. Also, if unauthorized copyright material had to be removed, a note will indicate the deletion.

Oversize materials (e.g., maps, drawings, charts) are reproduced by sectioning the original, beginning at the upper left-hand corner and continuing from left to right in equal sections with small overlaps. Each original is also photographed in one exposure and is included in reduced form at the back of the book.

Photographs included in the original manuscript have been reproduced xerographically in this copy. Higher quality 6" x 9" black and white photographic prints are available for any photographs or illustrations appearing in this copy for an additional charge. Contact UMI directly to order.

UMI

A Bell & Howell Information Company
300 North Zeeb Road, Ann Arbor MI 48106-1346 USA
313/761-4700 800/521-0600

Reproduced with permission of the copyright owner. Further reproduction prohibited without permission.

FAST MAGNETIC RESONANCE IMAGING TECHNIQUES FOR CARDIOVASCULAR DISEASE

A DISSERTATION
SUBMITTED TO THE DEPARTMENT OF ELECTRICAL ENGINEERING
AND THE COMMITTEE ON GRADUATE STUDIES
OF STANFORD UNIVERSITY
IN PARTIAL FULFILLMENT OF THE RQUIREMENTS
FOR THE DEGREE OF
DOCTOR OF PHILOSOPHY

Gerard Terrence Luk-Pat
October 1998

UMI Number: 9924460

UMI
300 North Zeeb Road
Ann Arbor, MI 48103

I certify that I have read this thesis and that in my opinion it is fully adequate, in scope and quality, as a dissertation for the degree of Doctor of Philosophy:

Dwight G. Nishimura

(Dwight G. Nishimura) Principal Advisor

I certify that I have read this thesis and that in my opinion it is fully adequate, in scope and quality, as a dissertation for the degree of Doctor of Philosophy:

Albert Macovski

(Albert Macovski)

I certify that I have read this thesis and that in my opinion it is fully adequate, in scope and quality, as a dissertation for the degree of Doctor of Philosophy:

Ivan R Linscott

(Ivan R. Linscott)

Approved for the University Committee on Graduate Studies:

Thomas Wasow

Abstract

Cardiovascular disease, which can manifest as heart attack and stroke, is the leading cause of death in industrialized nations. Magnetic resonance imaging (MRI) allows minimally-invasive detection of the effects of cardiovascular disease such as narrowing of blood vessels by atherosclerotic plaque and the resulting changes in blood velocity. MRI is routinely employed for imaging problems of the central nervous system and the musculoskeletal system, such as brain tumors and knee-ligament tears. However, MRI is not yet widely accepted for imaging the cardiovascular system because image quality can be severely compromised by a number of motion sources such as patient fidgeting, breathing and cardiac motion.

Fast MRI, which can acquire a two-dimensional image in less than one second, can avoid these motion problems. However, fast MRI can be crippled by artifacts from blood flow and imperfections in the magnetic fields used for imaging. In this thesis, a linear-systems approach to MRI was used to obtain novel fast-MRI techniques for which these artifacts are negligible. This linear-systems approach is based in the frequency domain since the underlying physical phenomenon is a resonant frequency of the hydrogen

nucleus which depends on the magnetic-field strength, allowing us to say that MRI data is acquired in the Fourier domain.

This thesis offers three contributions to cardiovascular MRI: (i) Echo-planar imaging (EPI) is a popular fast MRI technique that suffers from signal dropouts and ghosting in the presence of blood flow. By exploiting the relative importance of the low spatial frequencies in the image, EPI was modified to dramatically reduce these artifacts. In particular, partial-flyback EPI reduces sensitivity to flow in one direction and inside-out EPI reduces sensitivity to flow in the orthogonal direction. (ii) Velocity imaging can have long scan times because three or more dimensions are required: two spatial dimensions and one or more velocity dimensions. Previous incarnations of a fast technique that acquires velocity images in real time, with typical frame rates of 30/s, suffer from excessing blurring caused by magnetic-field imperfections. This technique was modified so that field imperfections cause a simple shift of the image instead of blurring. (iii) Atherosclerotic-plaque imaging currently uses techniques that focus on the degree of narrowing of the blood vessel. However, it is believed that the internal structure of the lesion can be a more useful predictor of which lesions will rupture and thereby cause sudden events such as stroke. Imaging the internal structure of plaque lesions is challenging because they have irregular geometries and widths of only a few millimeters. Moreover, signal from flowing blood can obscure signal from the lesion since it is typically much brighter. A novel imaging technique was designed, combining signal-excitation methods and fast-imaging methods to produce three-dimensional images with sub-millimeter resolution and flow suppression, all in a reasonable scan time.

Acknowledgements

Counting the pages in this thesis, I sadly realized that there was only one page for every two weeks I had spent at Stanford. But my time here was not so much filled with pages but with good memories and with good friendships.

At work

I'd like to thank Prof. Mark Godfrey Mungal of Mechanical Engineering for agreeing to chair my orals even though I didn't provide any coffee for that morning's proceedings!

I'd like to thank Dr. Ivan Linscott for actually being interested in reading my thesis (when it seemed that no one else would) and for his genuinely helpful comments.

I'd like to thank the National Institutes of Health and the National Science Foundation for their financial support and General Electric Medical Systems for financial support and for providing MRSRL with a clinical scanner that was available to us engineering types twenty-four hours a day.

I am grateful to John Kosek and other members of the pathology laboratory of the Palo Alto VA for help in obtaining *ex-vivo* specimens of atherosclerotic plaque and their histology.

I am also grateful to Shin-Yi Yen and Sandy Napel for software and computing resources used in obtaining oblique views of the 3D atherosclerotic-plaque images.

I'd like to thank my advisor, Dwight Nishimura, for showing me that one need not be arrogant to be very smart, nor a dramatic orator to be a great lecturer, that no one is too exalted to answer the phone or to serve cake, and that one can inspire tremendous effort without directly asking for it (as such, I have learned to interpret "Dwight-speak"). I would also like to thank him for the many times he said "come in" when I knocked on his door even though the lights were off and the sign said "out"; never once did I see any signs of irritation. Finally, I am eternally grateful to Dwight for letting me sneak into his research group at a time when leaving Stanford was not a ridiculous idea.

I'd like to thank my associate advisor, Al Macovski, for setting the tone of this lab: work hard, achieve a lot and then try to pretend that you are worthless and not so smart. I don't even think I am aware of even ten percent of what he has accomplished in his amazing career.

I'd like to thank Bob Hu for for reading my papers, for sharing his visions of what research was all about and for other insights into MRI life. I was lucky to be around someone who is as skillful in a cardiology clinic as in an engineering lab. (And all the while I would be wondering how much sleep he had gotten that day and what company he was going to start next.)

I'd like to thank John Pauly for allowing me to walk into his office at random times to borrow a journal or, more often, to seek out hidden regions of MRI. Thank you for showing me your co-operative, non-confrontational approach to research.

I'd like to thank Steve Conolly for showing me the value of being thorough and for answering my questions even though they had nothing to do with what he was working on. And for the following pearl of sports widsom: "You can play at the same level as you get older, you just have to accept more pain ..."

I'd like to thank Craig Meyer for organizing the MRSRL softball team every year, and guilt-tripping me into playing (except for the year that the team won the league championship; coincidence you say?), for teaching me the deep, dark secrets of Epic programming and for euthanizing his fish right in front of me!

I'd like to thank Dwight, Al, Bob, John, Steve and Craig for creating such a wonderful working environment. I doubt that I'll find a better place to work, ever. Here I have learned that very smart and successful people can also be, quite simply, very nice people. How is it that so much good research can come out of such an easy-going place?

I nominate Garry Gold for the title of "hardest working man in MRI." He hath given us so many storied moments. In lieu of full quotations, I provide here a smattering of key words or phrases: "excellent", "this is *hard*" and "those must be the fingers." And thank you so very much for introducing me to the pathology lab; I did so enjoy that.

I'd like to thank Eric Olcott for being just so excited about scanning patients. No doubt I'd still be scanning phantoms (or my beleaguered friends) without his enthusiasm and perseverance in recruiting patients.

From my past research life, I'd like to thank Fouad Tobagi for teaching me the value of being methodical in research and for teaching me, mayhap sometimes more than I wanted to know, about giving presentations.

It's been great to be part of the MRSRL gang of students; being immersed daily with this bunch of characters is the next best thing to living in a dormitory. I will remember them in these ways (and in no particular order):

- Pablo for his legacy of artwork and software and for running around the lab in circles when he finally got 3D cones to work!
- Elfar for being very generous with his time and advice, for always being very easy to talk to and for having a family where no one (himself, Veronica or Aldis) has the same last name.
- Patrick for showing us how to get married in only a few months and then how to balance addiction to X-pilot and addiction to his wife, Andrea.
- Todd for whatever part he played in sneaking me into this lab: much appreciated. Also, for showing me how to wrangle free stuff from airlines, how to sincerely be friends with so many people and, lest we forget, for having stupid opinions that I could make fun of. I'm glad you married Sandra for, one of these days, I think she will finally teach you that 55 degrees Fahrenheit is not the optimal temperature for humans.
- Sanjay for entertaining us with his various mishaps and rare illnesses, many incurred because of his astonishing reef tank. And for showing me that the way to get parking at Stanford is not to get up earlier but rather to upgrade your parking permit!
- Krishna for connecting us to the first generation who never needed quarters to play "Space Invaders", for being the first person to use the

words, "Say what?" in group meeting and for lending me the musical works of M'Chelle N'deg'cello, Prince and Maxwell.

- Glen for showing us how to prepare talks and posters in one day, schedule orals in one week and perhaps write a Ph. D. thesis in one month. How jealous was I? More importantly, how many kids will you and Barbara have?
- Adam for showing us how to sail the South Pacific, for always reading my computer screen (stop that!) and for showing us a dazzling array of shots in pool.
- Hatsumi for ensuring that I didn't quench the magnet while we refilled the cryogens, for being the only other person in the lab who was interested in "Babylon 5" and for that wonderful outdoor wedding that you and Rick treated us to.
- Jean for always stirring welcome conversation, especially when the work atmosphere was really intense, for allowing/making me move to lab before I graduated (I'm glad I did) and for defining lunch as a bagel with two little packs of jam.
- Dan for his quick wit and easy-going manner and for letting me stay in EV 139A (whose stove he cleaned every Sunday). He is perhaps the only man who never fell during his first day on roller blades, a day which took him up and down the five floors of the Panama Street parking structure. One of these days, Laurie's fabulous cooking *will* make you fat.
- Hossein for introducing me to Persian restaurants in the Bay Area. Salty yogurt mixed with soda water is actually not bad.
- Wally for being so generous with his time and good humor and for providing the most memorable quote of my Sydney trip [we are on a beach,

reclining on deck chairs, sipping piña coladas], "Look at us: twenty thousand dollars a year and here we are in the South Pacific."

- Lai-Chee for proving to me that one *can* subsist on bread alone and live in the Bay Area without a car or a TV; and for our long talks in Durand 303.
- Chi-Ming for taking over my old desk and not putting a single book on any of the shelves :)
- Shreyas for bringing the word "heinous" into everyday use (and at times, "Can I *stick* you in the magnet?" was also used daily) and for eliminating me from the running for the title of "best-dressed student." And for introducing me to the Drudge Report. Did I want to read it? Perhaps. Perhaps not.
- Hao for demonstrating the reality of e-mail in Chinese characters.
- Brian for organizing an ice-hockey session for all of us in Vancouver, for spending the most nights ex-cabin on our Whitsundays trip and for always being ready to strike up a conversation with a, "W'cha up to?"
- Greig for many conversations about soccer and ice hockey and for showing us what real electrical engineers do.
- Sylvia for working out in a gym with Jerry Rice while asking him, "Who is this Roger Craig fella?"
- Lily for being so enthusiastic, for organizing and often cooking so many great lunches and for saving us from the Stanford bureaucracy.
- Trish for regaling us with tales of Daphne and for also saving us from the Stanford bureaucracy.

Beyond work

I'd like to thank my wonderful wife, Peggy, for her love and support during all of my years here at Stanford; for teaching me to be punctual, to be considerate of others and the real value of giving gifts.

I'd like to thank my Mom and Dad for "raising me right", for showing me the value of hard work, for giving me my faith and for blessing me with such an easy-going childhood.

I'd also like to thank Ma and Pa Su and Lester for immediately accepting me into their family.

I'd like to thank my good friend, Steve Lee, for living across the street, for over-working the bartender at my wedding before giving a great speech and for introducing me to roller-blade hockey. I *will* defeat you on PlayStation's 1024-bit machine.

I'd also like to thank all of my friends here in the Bay Area from these walks of life: Rains and Escondido Village, particularly Keish and Rick; MIT; soccer; volleyball; roller hockey (where I re-lived my childhood days in Trinidad, playing soccer in the sun for hours on end).

Finally, I'd like to thank God for allowing me to work in this wonderful lab and for giving me such great friends and family. Dear God, bless and keep them all. Without you, I have done nothing.

Gerry Luk Pat
October 6, 1998
Stanford University

Contents

List of Tables

List of Figures

Chapter 1

Introduction

1.1 Imaging of cardiovascular disease

Cardiovascular disease is the leading cause of death in industrialised nations. For example, in the United States in 1994, cardiovascular disease claimed over 955,000 lives, or 42% of all deaths [1]. In comparison, the second leading cause of death, cancer, claimed 537,000 lives, or 24% of all deaths [1]. Cardiovascular disease affects the heart and blood vessels. Its major consequences include congestive heart failure, heart attack, stroke and ruptured aneurysms.

In general, imaging of the human body is important for the diagnosis and prognosis of disease and for treatment planning. Imaging goals for cardiovascular disease can be illustrated by considering congestive heart failure, where the objective might be to detect abnormal cardiac-wall motion or deficiencies in the volume of blood output during each cardiac cycle. Imaging goals for cardiovascular disease can also be illustrated by considering stroke, where the objective might be to estimate the narrowing of the carotid arteries or the resulting changes in blood velocity through the carotid bulb.

For imaging of cardiovascular disease, current clinical practice employs X-ray angiography, ultrasound and, to a limited extent, nuclear medicine. While X-ray angiography has good contrast and excellent spatial and temporal resolution, it requires invasive catheterization for the introduction of contrast dye and exposure to potentially-harmful doses of ionizing radiation. Also, it can produce misleading images since it forms two-dimensional images by projecting through a three-dimensional object. Ultrasound imaging is inexpensive and also has excellent spatial and temporal resolution. However, its view of the body is limited by the available acoustic windows wherein, for example, the heart may be occluded by the lungs. Also, it suffers from considerable operator dependence and from speckle noise which is correlated to the image. Nuclear medicine directly shows disease since the administered radioactive material is mostly absorbed by either the diseased areas or, in some regions of the body such as the heart, the non-diseased areas. Unfortunately, it has coarse spatial resolution, a poor signal-to-noise ratio and requires a linear accelerator to produce the necessary radioactive material.

MRI is a promising alternative for cardiovascular imaging. It has relatively high resolution and excellent soft-tissue contrast, can image nearly all parts of the body and is non-toxic. Also, through various natural and external contrast mechanisms, it can produce several types of images. MRI is routinely employed for imaging problems of the central nervous system and the musculoskeletal system, such as brain tumors and knee-ligament tears. From 1991 to 1995, the annual number of MRI studies in the United States was 7 million or more [2]. Unfortunately, MRI examinations are relatively expensive, with the cost of an examination ranging from $300 to $1000 [2]. Furthermore, conventional techniques are not optimal for cardiovascular imaging. This thesis addresses the second problem, as outlined in the next section.

1.2 Fast MRI of cardiovascular disease

Conventional MRI, which requires up to several minutes for a two-dimensional image, works well for imaging the central nervous system and the musculoskeletal system. However, for imaging the cardiovascular system, there are a number of motion sources such as respiratory and cardiac motion which can severely compomise the image quality of conventional MRI. Indeed, the resulting ghosting and blurring may render the image useless. Fast MRI, which can acquire a two-dimensional image in less than one second, can avoid these motion problems. However, blood flow and imperfections in the magnetic fields used for imaging can produce ghosting, blurring and signal loss which may render fast MRI useless. This thesis will present novel imaging techniques for which these artifacts are negligible.

In general, an MRI technique consists of two phases: signal excitation and data acquisition. The design of imaging techniques in this thesis will explore both the data-acquisition phase and, to a lesser extent, the signal-excitation phase.

It can be said that data acquisition occurs in the frequency domain because the fundamental physical phenomenon is a resonant frequency of the hydrogen nucleus which depends on the magnetic-field strength. From this frequency-domain perspective, data acquisition in MRI can be analyzed using a linear-systems approach. Now all of the tools of linear systems [3] such as Fourier transforms and sampling theorems can be used in the analysis of MRI. Linear-systems analysis of MRI is typically restricted to the spatial dimensions of the image. In this thesis, artifacts caused by blood flow and magnetic-field imperfections will be analyzed by considering velocity and resonant-frequency dimensions of the image. In general, artifacts are produced because data is acquired in a multi-dimensional Fourier space and images are made by projecting that data onto only a few of those dimensions. It is this collapse of many dimensions into a few dimensions which results in artifacts. Following this analysis, data-acquistion schemes will be designed to make these artifacts negligible.

While signal excitation is, in general, a non-linear process, there are excitation schemes based on exact descriptions and linear approximations of the excitation process. This thesis employed such excitation schemes to reduce imaging time and to suppress unwanted signal, even in the presence of magnetic-field imperfections.

1.3 Outline

The rest of this thesis is structured as follows. The specific contributions of this thesis, as achieved through imaging-technique design, are described in this section.

Chapter 2: Overview of MRI

A description of nuclear magnetic resonance (NMR) is followed by its generalization to MRI. The equations describing the excitation and acquisition of the MR signal are presented and the applicability of linear-systems analysis is demonstrated.

Chapter 3: Reducing flow artifacts in echo-planar imaging

The first contribution of this thesis is showing how to avoid signal dropouts and ghosting caused by blood flow in echo-planar imaging (EPI), which is a popular fast MRI technique. By exploiting the importance of low spatial frequencies in the image, the data-acquisition technique will be modified to virtually eliminate these artifacts. Portions of this chapter have previously been published in Luk Pat *et al.* [4].

Chapter 4: Real-time velocity imaging

The second contribution of this thesis is showing how to avoid blurring caused by magnetic-field imperfections in a velocity-imaging technique which produces images in real-time at a rate of 30 frames/s. For velocity imaging, scan times can be long since three or more dimensions are required: two spatial and one or more velocity dimensions. A fast technique will be described that acquires velocity images in real time, that is, with temporal resolutions of about 30 frames/sec. This technique was designed to avoid blurring from magnetic-field imperfections. Portions of this chapter have been accepted for publication as Luk Pat *et al.* [5].

Chapter 5: Atherosclerotic-plaque imaging

The third contribution of this thesis is showing how to acquire images of the internal structure of atherosclerotic-plaque lesions in a reasonable scan time. For imaging of atherosclerotic plaque, current techniques focus on the degree of narrowing of the blood vessel. However, it is believed that the internal structure of the lesion can be a more useful predictor of which lesions will rupture and thereby cause sudden events such as stroke. Imaging the internal structure of plaque lesions requires high-resolution, three-dimensional imaging because the lesions have widths of only a few millimeters and irregular geometries. This can mean long scan times since a three-dimensional image can be thought of as a number of two-dimensional images. Moreover, signal from flowing blood can obscure signal from the lesion since it is typically much brighter.

Signal-excitation techniques will be used to (i) restrict the signal-producing region to a cylinder, reducing the scan time, and (ii) suppress the signal from flowing blood. These excitation techniques will be combined with a fast image-acquisition technique which experiences negligible distortion from magnetic-field imperfections. The end result is a technique that acquires three-dimensional images with sub-millimeter resolution and flow suppression, all in a reasonable scan time. Portions of this chapter have been submitted for publication as Luk Pat *et al.* [6].

Chapter 6: Summary

The contributions of this thesis are summarized and conclusions and suggestions for future work are presented.

Chapter 2

Introduction to MRI

This chapter provides a brief introduction to MRI with the simple goal of providing a context for the rest of this thesis. A brief historical overview is presented first. The physics of magnetic resonance are described followed by an explanation of how images are formed. Some of the additional complexities introduced by human physiology, non-ideal instruments and the need to distinguish among different types of tissue are discussed. This chapter owes a great deal to similar tutorials by Walter Block [7] and Adam Kerr [8] as well as to the textbook that is in preparation by Dwight Nishimura [9], the last of which provides a detailed introduction to MRI.

2.1 Historical overview

The physical phenomenon underlying MRI is nuclear magnetic resonance (NMR). Nuclei with an odd number of nucleons, where a nucleon is a proton or a neutron, possess a net magnetic moment and consequently exhibit a resonant frequency in the presence of an external magnetic field. This was discovered independently by research groups led by Purcell [10] and

Bloch [11]. NMR is an important technique in its own right and is widely used to examine molecular structures in physics, chemistry and biology since it does not destroy the object being studied.

It can be considered that MRI came into being in 1973 when Lauterbur showed how NMR could be used to make images by making the resonant frequency different for each spatial location in the object [12]. The doorway for engineering analysis of MRI was opened in 1974 when Fourier transforms were used to reconstruct MR images based on Lauterbur's technique [13]. During the 1970s, MRI was mostly developed in academic institutions, in the United Kingdom. In the 1980s, as clinical uses of MRI became economically promising, the combined resources of industry and academia spurred dramatic improvments in image quality which continue to this day.

Today, MRI is used for non-destructive imaging of humans, animals and excised specimens. In the laboratory, its uses include chemical analysis and the interrogation of biological processes. In the clinic, it is routinely employed for imaging problems of the central nervous system and musculoskeletal system, such as brain tumors and knee-ligament tears. For abdominal and cardiovascular imaging, clinical use is not as widespread and these are active areas of research.

2.2 Physical basis for MRI

As stated above, the physical phenomenon underlying MRI is NMR. While a complete description of NMR requires quantum mechanics, a classical-mechanics treatment is adequate for our discussion. Nuclei which exhibit NMR can be visualized as spinning charged spheres that give rise to a small magnetic moment; we will often refer to them as "spins." For biological specimens, interesting nuclei are ^{1}H, ^{13}C, ^{19}F, ^{23}Na, and ^{31}P. In the human body, the population of ^{1}H is the most abundant species, because the body consists largely of water, and the most sensitive species, because it produces the largest signal per nucleus. Since the imaging of ^{1}H protons forms the basis of clinical MRI, it will be the sole concern of this thesis.

2.2.1 Resonance condition

In the absence of any external magnetic field, the magnetic moments of water ^{1}H protons are randomly aligned, as shown in Fig. 2.1a, and no net macroscopic magnetic moment exists. However, in the presence of an external field B_0, the spins align in parallel and antiparallel states, as illustrated in Fig. 2.1b. This results in a net magnetic moment, M, pointing in the direction of the external field. According to MR convention, this direction is referred to as the longitudinal axis or z axis.

If this moment, M, is perturbed from its equilibrium position, it will

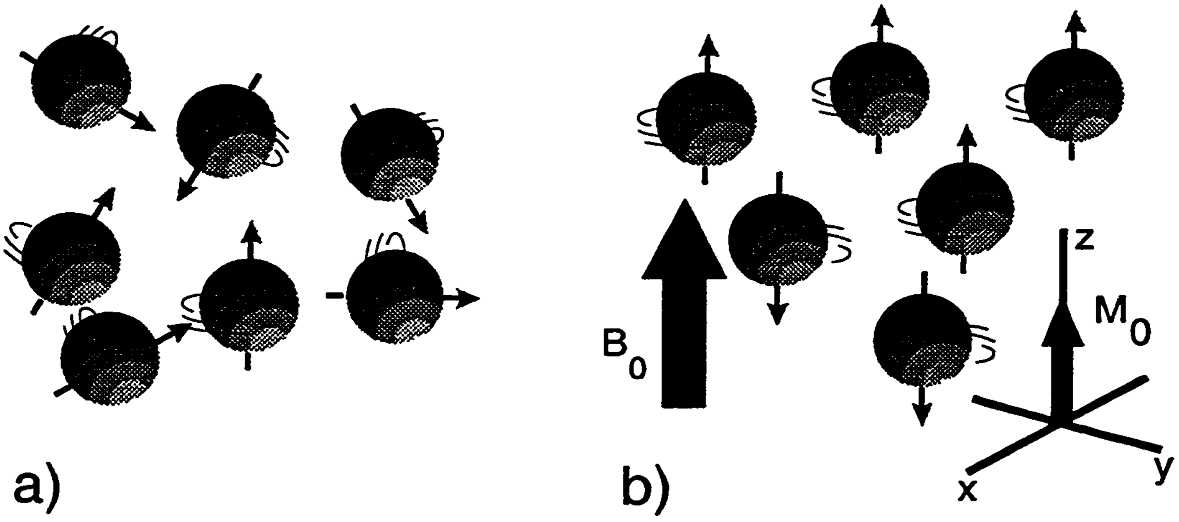

Figure 2.1: (a) Protons in the absence of an external field align randomly. (b) In an external field, protons align in two states with a net magnetization, M_0, parallel to the external field, B_0.

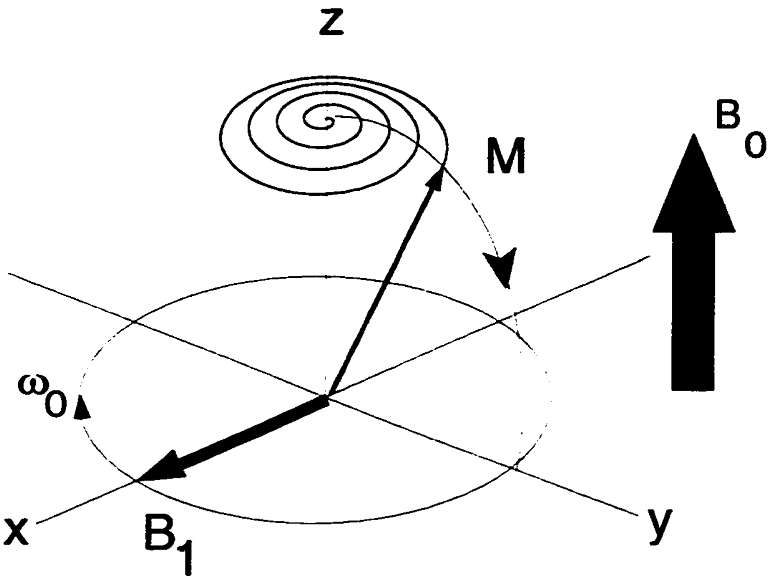

Figure 2.2: RF perturbation applied at the resonant frequency, ω_0, in the transverse plane tips the magnetization into the transverse plane where it rotates at the resonant frequency, ω_0.

precess around the z axis at a resonant frequency,

$$\omega_0 = \gamma B_0. \tag{2.1}$$

This is known as the Larmor frequency. The gyromagnetic ratio, γ, is a constant for each species, measuring 42.57 MHz/T for ^{1}H.

This perturbation can be accomplished by applying a radiofrequency (RF) magnetic pulse, B_1, rotating in the x-y plane at the resonant frequency, ω_0, as shown in Fig. 2.2. This RF pulse can be configured to tip the magnetization, M, into the x-y plane, also known as the transverse plane. Such an RF pulse is referred to as a 90° pulse since it rotates the magnetization through 90° in, for example, the y-z plane. In the transverse plane, the magnetization, M, continues to rotate at the Larmor frequency and produces a signal in a receiver coil through Faraday induction, as shown in Fig. 2.3.

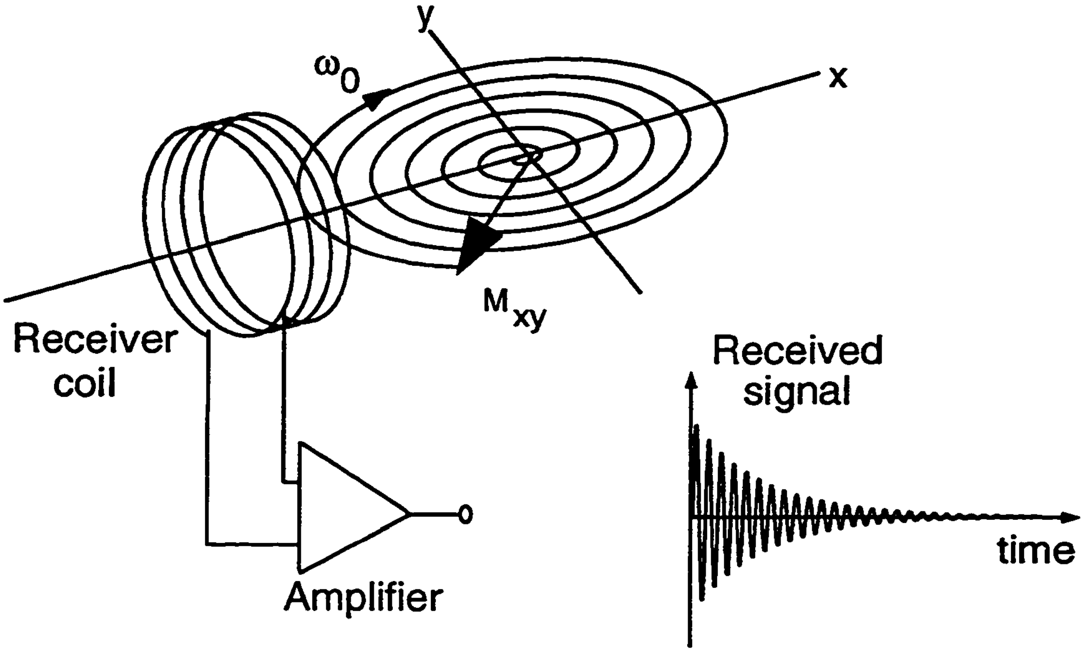

Figure 2.3: Rotating transverse magnetization creates a time-variant magnetic field which induces an electric signal in a receiver coil.

2.2.2 Signal relaxation

After the magnetization, M, is perturbed, it will eventually return to its equilibrium position. Suppose the magnetization has an initial amplitude, M_0, and is perturbed or excited by a 90° RF pulse. The transverse component, shown as M_{xy} in Fig. 2.4, decays exponentially to zero with time constant, T_2, as described by this equation:

$$M_{xy} = M_0 \, e^{-t/T_2} \tag{2.2}$$

T_2 decay is produced by the interaction of the nuclear spins with each other. It does not change the energy of the spin system but rather increases its disorder, reducing its ability to produce a coherent signal [14]. This T_2 decay means that we cannot observe the signal forever after just one perturbation; typically, multiple perturbations are needed for one image. The observation time after a given perturbation is typically on the order of T_2. For human tissue that is of clinical interest, T_2 can be less than 1 ms but typically is on the order of 10 ms to 100 ms. In addition, the longitudinal component, shown as M_z in Fig. 2.4, recovers exponentially with time constant, T_1, as described by this equation:

$$M_z = M_0 \left(1 - e^{-t/T_1}\right) \tag{2.3}$$

This T_1 recovery arises because the nuclear spin interacts with the entire solid or liquid lattice; energy that was absorbed by the spin system from the perturbing RF source is transferred to the lattice [14]. This T_1 recovery means that, if one perturbation follows too closely after another, there may be insufficient signal. The time between perturbations is typically on the order of T_1 and, for human tissue that is of clinical interest, T_1 is on the order of 100 ms to 1 second. T_1 and T_2 decay are also significant in distinguishing tissue types which have different T_1 and T_2 values, such as muscle versus blood or healthy tissue versus malignant tumor.

The perturbation and relaxation behavior of the magnetic moment is

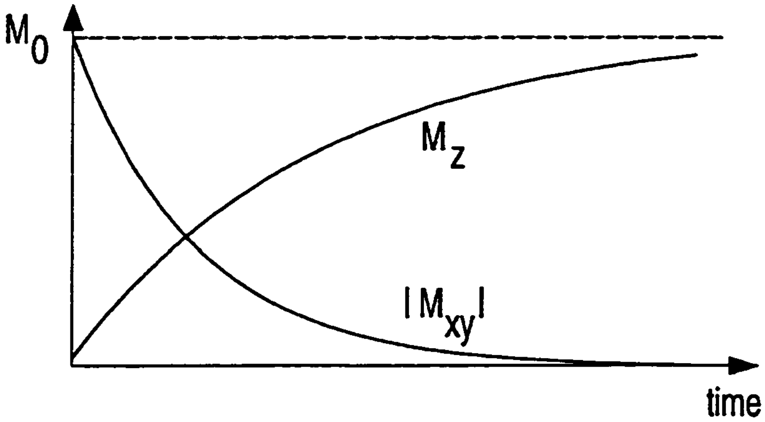

Figure 2.4: Transverse magnetization, $|M_{xy}|$, and longitudinal magnetization, M_z, following a 90° pulse.

nicely described by the Bloch equation given below:

$$\frac{d\mathbf{M}(t)}{dt} = \mathbf{M}(t) \times \gamma\mathbf{B} - \frac{\left(M_z(t) - M_0\right)\mathbf{k}}{T_1} - \frac{\left(M_x(t)\mathbf{i} + M_y(t)\mathbf{j}\right)}{T_2} \qquad (2.4)$$

where $\mathbf{M}(t) = M_x(t)\mathbf{i} + M_y(t)\mathbf{j} + M_z(t)\mathbf{k}$ and M_0 is the initial magnitude of the moment. The cross-product term on the right-hand side of Eq. 2.4 describes how external magnetic fields, such as RF fields, can change the direction of the magnetization vector. The second and third terms of this equation describe how the longitudinal and transverse components of **M** return to equilibrium with time constants T_1 and T_2, respectively.

2.3 Forming images

In both NMR and MRI, the static magnetic field, B_0, and the RF field, B_1, are used to create and perturb the spins so we can record their signals as they return to equilibrium. However, unlike in NMR, MRI uses additional magnetic fields to distinguish spins in different spatial locations, thereby creating images.

2.3.1 Fourier space

The additional magnetic fields used in MRI are known as gradient fields and they make the resonant frequency vary linearly in space. For example, Fig. 2.5 demonstrates the total external magnetic field without and with an x gradient. Without the x gradient, the resonant frequency is independent of x and is given by Eq. 2.1. For the two objects shown in Fig. 2.5, the received signal consists of a single frequency and its Fourier transform

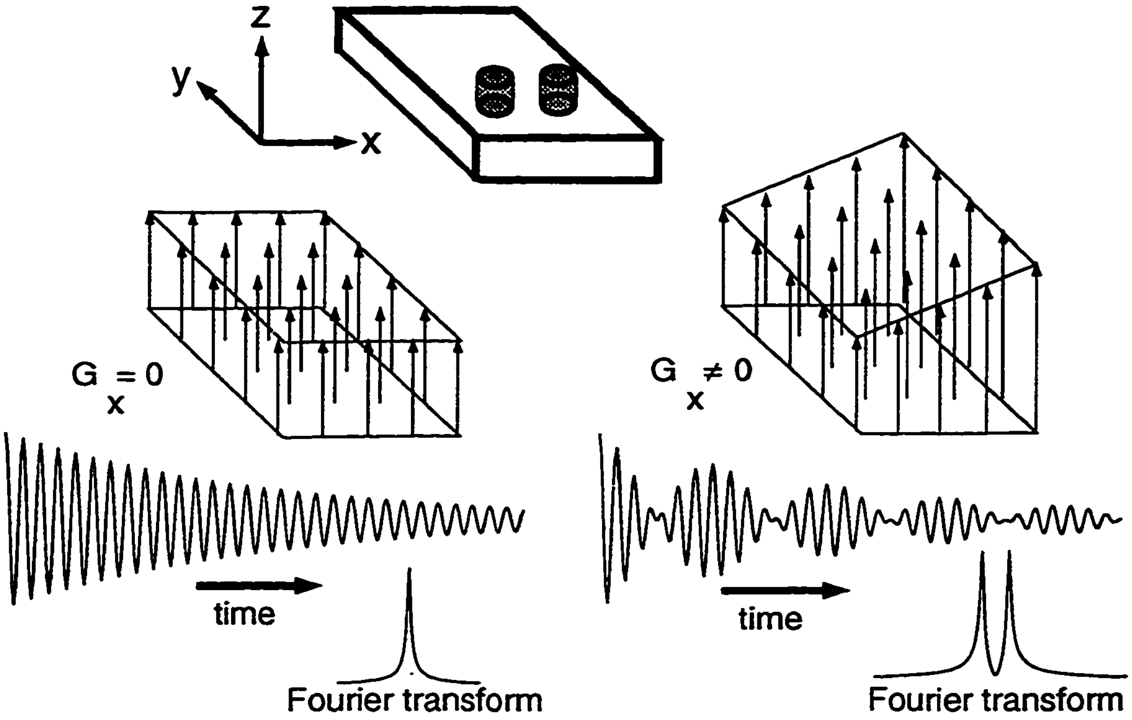

Figure 2.5: When a gradient is applied, the frequency of a spin becomes dependent on spatial position. A Fourier transform decodes phase information into positional information.

therefore consists of only a single peak. With the *x* gradient turned on, the resonant frequency depends linearly on *x* as follows:

$$\omega = \gamma\left(B_0 + G_x x\right) \tag{2.5}$$

where G_x is the slope of the applied gradient field. Now, the spins in the two objects resonate at two different frequencies, the received signal displays an interference pattern of these two frequencies and its Fourier transform shows two peaks.

Now consider an ensemble of spins distribute over multiple *x* locations. The received signal consists of many frequencies and is given below:

$$s(t) = \int m(x)\, e^{-i2\pi f(x)t} dx \tag{2.6}$$

where $m(x)$ is the number of spins at x, $f(x)$ is the resonant frequency at x and signal relaxation has been ignored. Inserting Eq. 2.5, we get

$$s(t) = \int m(x)\, e^{-i\gamma(B_0+G_x x)t} dx \tag{2.7}$$

$$= e^{-i\gamma B_0 t} \int m(x)\, e^{-i\gamma G_x t x} dx \tag{2.8}$$

After demodulating the received signal to remove the $e^{-i\gamma B_0 t}$ term, we can write the demodulated signal as

$$s_1(t) = \int m(x)\, e^{-i\gamma G_x t x} dx \tag{2.9}$$

This can be re-written as

$$s_1(t) = \int m(x)\, e^{-i2\pi k_x(t) x} dx \tag{2.10}$$

where

$$k_x(t) = \frac{\gamma}{2\pi}\, G_x\, t \tag{2.11}$$

Equation 2.10 is very similar to the following equation,

$$M(k_x) = \int m(x)\, e^{-i2\pi k_x x} dx \tag{2.12}$$

which introduces $M(k_x)$ as the Fourier transform of $m(x)$ where x is the spatial variable and k_x is the spatial-frequency variable. By comparing Eqs. 2.10 and 2.12, we can say that sampling $s_1(t)$ in time is equivalent to sampling $M(k_x)$ in k_x. Therefore, it can be said that MRI data is acquired in the Fourier domain, or "*k*-space" as it is known in the MRI literature [15, 16].

This Fourier-space interpretation allows a linear-systems approach to MRI. It can be generalized to include multiple spatial dimensions since, in general, MRI systems use three gradient fields, one each for the x, y and z directions. It can also be generalized to include a resonant-frequency dimension, which is the spectroscopic dimension used in NMR, and motion dimensions which describe, for example, velocities in the x, y and z directions.

2.3.2 Gradient-recalled-echo imaging

The simplest MR imaging technique is gradient-recalled-echo imaging. It acquires an image of a slice by first exciting that slice then acquiring a two-dimensional (2D) image of that slice.

An RF pulse that excites only a slice is used to reduce the imaging task from three dimensions to two dimensions. For example, to selectively excite the spins in a thin slab perpendicular to the z axis, as shown in Fig. 2.6, we use an amplitude-modulated RF pulse accompanied by a field gradient in the z direction [17]. To an approximation, the shape of the slab along z, or the slice profile, is the Fourier transform of the RF envelope [18, 19].

Once we have excited the desired slice along z, we use gradient fields in the x and y directions to acquire an image in the x-y plane. The demodulated received signal can be written as follows:

$$s(t) = \iint m(x,y)\, e^{-i2\pi\left[k_x(t)x + k_y(t)y\right]}\, dx\, dy \qquad (2.13)$$

where signal relaxation has been ignored and k_x and k_y are the time integrals of the x and y gradients, respectively:

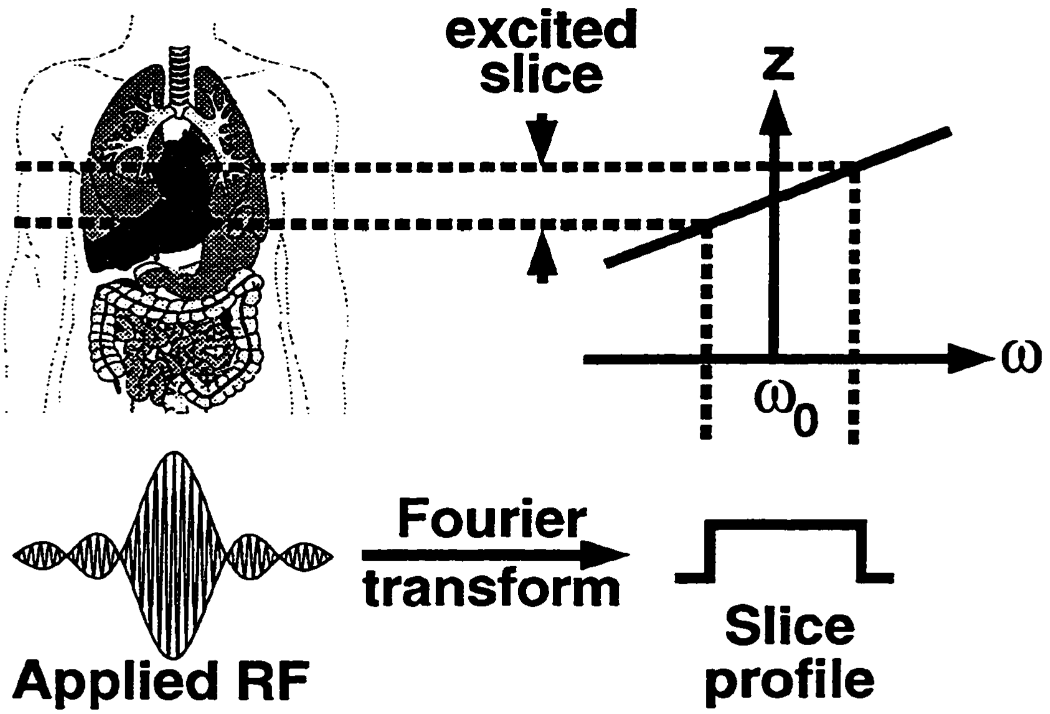

Figure 2.6: A gradient applied simultaneously with an RF pulse limits excitation to those spins resonating at frequencies within the bandwidth of the RF pulse. Spins made to resonate by the gradient at frequencies outside the RF pulse bandwidth are left unaffected.

$$k_x(t) = \int_0^t \frac{\gamma}{2\pi}\, G_x(\tau)\, d\tau \tag{2.14}$$

$$k_y(t) = \int_0^t \frac{\gamma}{2\pi}\, G_y(\tau)\, d\tau \tag{2.15}$$

In gradient-recalled-echo imaging, a rectangular region of *k*-space is used to produce an image. As shown in Fig. 2.7, this rectangular region is acquired one line at a time. For each line, we begin at the origin of *k*-space and travel along a diagonal path to the left edge of that line. Data acquisition occurs as we move from the left edge of that line to the right edge. This sequence of events in *k*-space is reflected in the waveform diagram of Fig. 2.8:

(a) For each line, RF and G_z waveforms similar to those in Fig. 2.6 are used to excite the same slice.

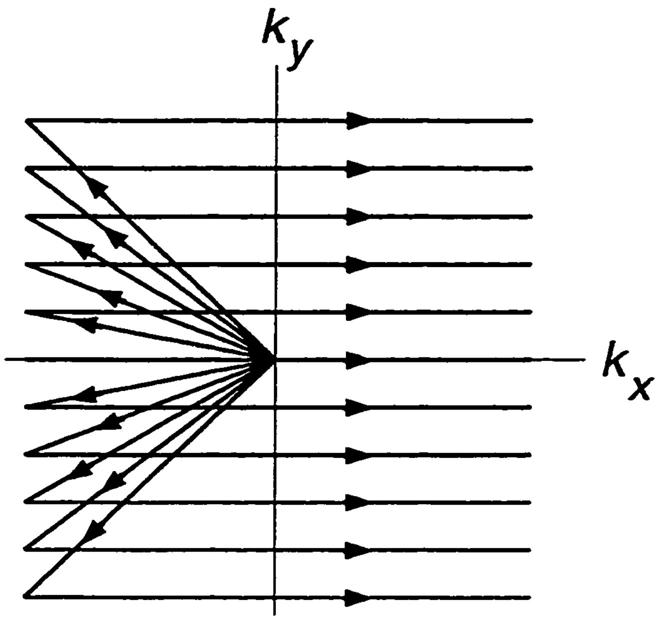

Figure 2.7: The k-space trajectory for gradient-recalled-echo imaging. One line of constant k_y is acquired after each excitation.

(b) The diagonal path is produced by the G_y waveform and the negative-amplitude portion of the G_x waveform. For each excitation, the G_y waveform has a fixed amplitude and moves the k-space trajectory vertically. In Fig. 2.8, the step-ladder appearance of the G_y waveform is meant to connote that different G_y amplitudes are used for different excitations. The negative-amplitude portion of the G_x waveform moves the k-space trajectory to the left edge of the desired line.

(c) The positive-amplitude portion of the G_x waveform moves the k-space trajectory from left to right. During this time, data acquisition occurs as shown by the 'DAQ' line in Fig. 2.8.

In the MRI literature, G_z is known as the slice-selection gradient, G_y as the phase-encode gradient and G_x as the readout gradient.

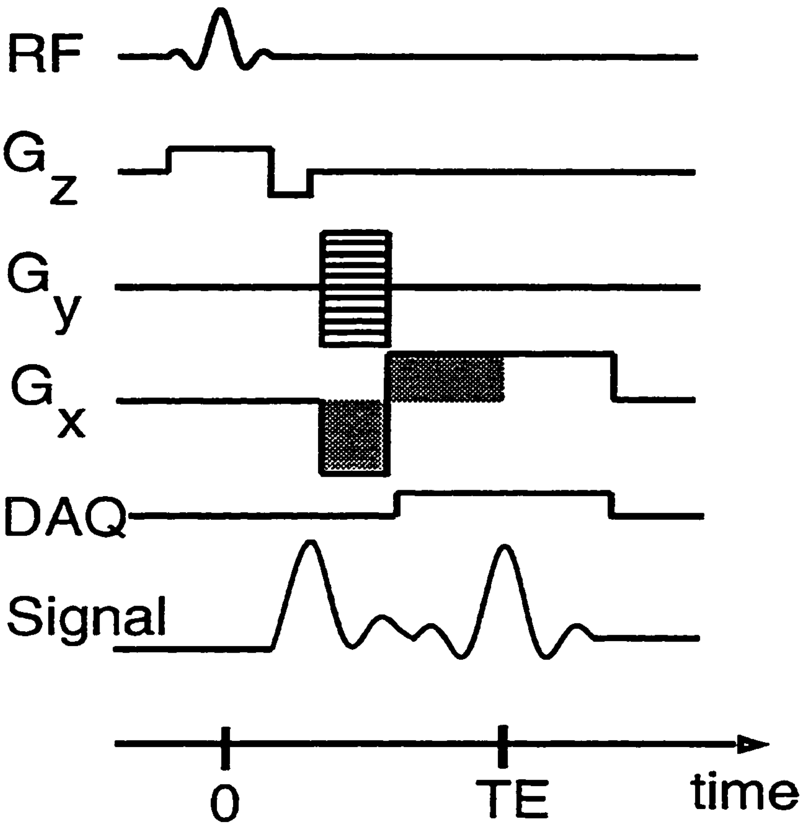

Figure 2.8: The gradient recalled echo imaging sequence. The RF and G_z waveforms excite a slice in z. Data is acquired while G_x is positive. This sequence is repeated at intervals of TR, with a different amplitude for G_y in each interval. The gradient-recalled echo occurs at a time, TE, after the RF excitation.

This imaging technique is known as gradient-recalled-echo imaging for the following reasons. In Fig. 2.8, the received signal has two peaks. The first peak is discarded because it does not occur along the desired k-space line. However, data is acquired during the second peak which is formed when the trajectory passes through $k_x = 0$. That is, it is formed at that instant in time when the area under the negative-amplitude portion of G_x exactly matches the area under the positive-amplitude portion of G_x; these matching areas are shaded in Fig. 2.8. This second peak is known as a gradient-recalled echo or gradient echo since the signal peak has been recalled by manipulating the x

gradient. The time at which the gradient echo occurs is called the echo time or TE.

2.3.3 Sampling requirements

As described in Section 2.3.1, data is acquired in *k*-space and then Fourier transformed to produce an image. This section discusses two aspects of the *k*-space data sampling that affect image formation, using the gradient-recalled-echo imaging of the previous section as an example.

2.3.3.1 Resolution

The spatial resolution of an image is determined by the width of the region acquired in *k*-space. For example, Fig. 2.7 shows that a rectangular region of *k*-space is acquired. Spatial resolution in the y direction is determined by the width of that rectangle in the k_y direction. Similarly, spatial resolution in the x direction is determined by the width of that rectangle in the k_x direction. Limiting data acquisition to a rectangular region in *k*-space is equivalent to multiplying $M(k_x,k_y)$, the two-dimensional Fourier transform of $m(x,y)$, by a rectangle which can be written as

$$\Pi\left(\frac{k_x}{W_{k_x}}\right)\Pi\left(\frac{k_y}{W_{k_y}}\right) \tag{2.16}$$

where

$$\Pi(q)=\begin{cases}1 & \text{for } |q|\leq 1/2\\ 0 & \text{otherwise}\end{cases} \tag{2.17}$$

W_{k_x} = width of the rectangle in the k_x direction

W_{k_y} = width of the rectangle in the k_y direction

This is further equivalent to convolving *m(x,y)* with the two-dimensional Fourier transform of that rectangle as given by

$$\mathrm{sinc}\left(W_{k_x} x\right)\mathrm{sinc}\left(W_{k_y} y\right) \tag{2.18}$$

This can be regarded as an impulse response since it would be the image produced by a single spin which was located at $(x,y) = (0,0)$. By convention, spatial resolution in the x or y direction is defined as the distance from the center of this impulse response to the first zero in that direction and is given by

$$\Delta x = \frac{1}{W_{k_x}} \tag{2.19}$$

$$\Delta y = \frac{1}{W_{k_y}} \tag{2.20}$$

2.3.3.2 Field-of-view

Because of the sampling of $M(k_x,k_y)$, there is replication of $m(x,y)$. The distance between two adjacent replications of $m(x,y)$ is the field-of-view. If $m(x,y)$ is wider than the field-of-view then replications of $m(x,y)$ will overlap and *aliasing* is said to occur. The field-of-view is determined by the sampling density in k-space. For example, Fig. 2.7 shows that the rectangular region of k-space is sampled in the k_y direction. Although not shown, sampling also occurs in the k_x direction; this was alluded to in the discussion of Eq. 2.12 which remarked that sampling $s_1(t)$ in time is equivalent to sampling $M(k_x,k_y)$ in k_x. This k-space sampling is equivalent to multiplying $M(k_x,k_y)$ by an impulse train which can be written as

$$III\left(\frac{k_x}{\Delta_{k_x}}\right)III\left(\frac{k_y}{\Delta_{k_y}}\right) \tag{2.21}$$

where

$$III(q)=\begin{cases}1 & \text{when } q \text{ is an integer}\\ 0 & \text{otherwise}\end{cases} \tag{2.22}$$

Δ_{k_x} = distance between samples in the k_x direction

Δ_{k_y} = distance between samples in the k_y direction

This is further equivalent to convolving $m(x,y)$ with the two-dimensional Fourier transform of that impulse train which is given by

$$III\left(\Delta_{k_x}x\right)III\left(\Delta_{k_y}y\right) \tag{2.23}$$

The field-of-view is then given as

$$FOV_x=\frac{1}{\Delta_{k_x}} \tag{2.24}$$

$$FOV_y=\frac{1}{\Delta_{k_y}} \tag{2.25}$$

An anti-aliasing filter can be used during data acquisition. In gradient-recalled-echo imaging, data is acquired while travelling in the k_x direction. Therefore, the anti-aliasing filter will limit the field-of-view in the x direction. This may be more easily understood by considering the physical situation. During data acquisition, the resonant frequencies of the spins depend only on x location because only the x gradient is active. Since the anti-aliasing filter only passes a certain range of frequencies, spins that are at distant x locations will not be seen in the acquired data.

2.4 Imaging in the real world

There are a number of factors affecting the quality of MR images that are introduced by human physiology and by imperfections in the magnetic fields used for imaging.

2.4.1 Off-resonance effects

Thus far, we have assumed a perfectly uniform magnetic field, B_0, and thus, in the absence of gradient fields, a perfectly uniform resonant frequency. In practice, resonant frequencies will vary across a human subject for three reasons: (i) inhomogeneities in the main field, which for current superconducting 1.5-T magnets, produce maximum frequency offsets of about 21 Hz; (ii) differences in bulk magnetic susceptibility, in particular, air-tissue interfaces which produce a frequency offset of 800 Hz in a 1.5-T magnet; and (iii) chemical shift differences between the hydrogen nuclei in water and the hydrogen nuclei in fat, which is generally considered to be 220 Hz in a 1.5-T magnet.

Off-resonance can have a significant effect on magnetic resonance images. It causes unwanted phase to accumulate in *k*-space which can produce signal loss, geometric distortion, ghosting or blurring. After demodulation, the phase of the signal received from an on-resonant spin located at $x = x_0$ is given by:

$$\begin{aligned} \phi_{on}(t) &= \int_0^t \gamma G_x(\tau)\, x_0 \, d\tau && (2.26) \\ &= x_0 \int_0^t \gamma G_x(\tau)\, d\tau && (2.27) \end{aligned}$$

This phase is used to encode position. However, for an off-resonant spin whose frequency is offset by $\Delta\omega$, the phase is given by

$$\phi_{off}(t) = \int_0^t \left[\gamma G_x(\tau)\, x_0 + \Delta\omega\right] d\tau \tag{2.28}$$

$$= x_0 \int_0^t \gamma G_x(\tau)\, d\tau + \int_0^t \Delta\omega \; d\tau \tag{2.29}$$

While the first term is used to encode position, the second term is unwanted and can produce artifacts in the image.

More formally, the second term in Eq. 2.29 can be used to add a resonant-frequency dimension to the k-space description of MRI. Let us define

f = resonant frequency

which is related to $\Delta\omega$ by

$$\Delta\omega = 2\pi f \tag{2.30}$$

We can now write the received signal after demodulation as

$$s_1(t) = \int m(x,f)\, e^{-i2\pi[k_x(t)x + k_f(t)f]} dx\, df \tag{2.31}$$

where the magnetization, m, is now a function of x and f. The k-space duals of x and f are given as

$$k_x(t) = \tfrac{\gamma}{2\pi} \int_0^t G_x(\tau)\, d\tau \tag{2.32}$$

$$k_f(t) = t \tag{2.33}$$

The effects of the unwanted phase produced by off-resonance will be examined more closely in succeeding chapters.

2.4.2 Flow effects

Until now, we have also assumed stationary spins but, in practice, there is motion of spins since various fluids circulate throughout the human body including blood, cerebrospinal fluid and extra-cellular fluid. In cardiovascular imaging, we are mainly concerned with the flow of blood. Since blood flow is driven by the cardiac cycle, it is pulsatile: a plot of velocity versus time shows a peak associated with systolic contraction and a period of slow flow associated with diastolic expansion. The velocity-time profile can be affected by the geometry of the vascular system and the elasticity of the blood vessels; all of which can be affected by disease. Typical velocities in healthy subjects are 100 cm/s for peak flow in the carotid artery [20] and 25 cm/s for peak flow in the popliteal artery [21].

Like off-resonance, flow causes unwanted phase to accumulate in *k*-space which can produce signal loss, geometric distortion, ghosting or blurring. The phase of a stationary spin located at $x = x_0$ is given by Eq. 2.27. This phase is used to encode position. However, for a spin which starts at $x = x_0$ but which moves with a velocity, v, in the x direction the phase is given by

$$\phi_{moving}(t) = \int_0^t \gamma G_x(\tau)(x_0 + v\tau)\, d\tau \tag{2.34}$$

$$= x_0 \int_0^t \gamma G_x(\tau)\, d\tau + v\int_0^t \gamma \tau\, G_x(\tau)\, d\tau \tag{2.35}$$

While the first term is used to encode position, the second term is unwanted and can produce artifacts in the image.

More formally, the second term in Eq. 2.35 can be used to add a velocity dimension to the *k*-space description of MRI [22] . We can write the received signal after demodulation as

$$s_1(t) = \int m(x,v)\, e^{-i2\pi[k_x(t)x+k_v(t)v]} dx\, dv \tag{2.36}$$

where the magnetization, *m*, is now a function of *x* and *v*. The *k*-space duals of *x* and *v* are given as

$$k_x(t) = \tfrac{\gamma}{2\pi} \int_0^t G_x(\tau)\, d\tau \tag{2.37}$$

$$k_v(t) = \tfrac{\gamma}{2\pi} \int_0^t \tau\, G_x(\tau)\, d\tau \tag{2.38}$$

The effects of the unwanted phase produced by velocity will be examined more closely in succeeding chapters. It should be noted that the Doppler shift is negligible for velocities encountered in the human body.

It should also be noted that, in general, the location, *x*, of a spin at a time, *t*, can be written as

$$x(t) = x_0 + vt + at^2 + \ldots + x^{(n)}t^n + \ldots \tag{2.39}$$

where a is acceleration and $x^{(n)}$ is the nth order of motion. For $x^{(n)}$, the *k*-space dual can be written as

$$k_{x^{(n)}}(t) = \tfrac{\gamma}{2\pi} \int_0^t \tau^n\, G_x(\tau)\, d\tau \tag{2.40}$$

This is called the nth gradient moment. As noted in Section 2.2.2, data-acquisition times in MRI are usually on the order of milliseconds, that is, t « 1, so that gradient moments diminish as the order of motion increases.

Therefore, in this thesis, we will focus on the first order of motion, which is velocity.

2.4.4 SNR

As we will see in Chapter 5, image SNR becomes scarce as we strive for sub-millimeter resolution. In MRI, noise has two main sources: (i) thermal noise in the receiver coil and (ii) thermal noise from fluctuating magnetic fields in the body since the body is a conductive medium. In the MRI literature, the signal-to-noise ratio (SNR) is defined as follows:

$$\mathrm{SNR} = \frac{\text{signal amplitude}}{\text{standard deviation of noise}} \tag{2.41}$$

While a complete description of noise in MR is beyond the scope of this chapter, it is useful to summarize the analysis presented by Nishimura [9].

Both instrument and image-sequence parameters affect the resultant SNR of an image. Instrument parameters affecting SNR can be simplified to expressions involving only B_0. If, as in most situations, body noise dominates coil noise, we have

$$\mathrm{SNR} \propto B_0 \tag{2.42}$$

Image-sequence parameters affecting SNR are more relevant to this thesis since these are more easily changed than the strength of the main field, B_0. Analysis of the SNR for a particular volume element of the image, or voxel, yields this expression [23]:

$$\mathrm{SNR} \propto (\Delta x)\,(\Delta y)\,(\Delta z)\,\sqrt{T_{DAQ}}\;\; f(\rho, T_1, T_2) \tag{2.43}$$

where Δx, Δy and Δz are the voxel widths in each dimension and T_{DAQ} is the total data-acquisition time for the entire image. The final term, $f(\rho, T_1, T_2)$, is an image-sequence-dependent function of the spin density, ρ, and the relaxation properties of the spins in the voxel. Some of the image-sequence parameters affecting this function are the excitation flip angle, echo time and repetition time. Equation 2.43 shows that SNR decreases as the image resolution increases, that is, as the voxel widths decrease.

2.5 Image contrast

Image contrast is useful in distinguishing tissue types such as muscle versus blood or healthy vessel wall versus diseased vessel wall. This section introduces techniques that will be used for atherosclerotic-plaque imaging in Chapter 6.

2.5.1 T_1 and T_2 contrast

In addition to the spatial concentration of ^1H protons, differences in T_1 and T_2 values can also be used to generate contrast. For the gradient-recalled-echo imaging sequence, image contrast is affected by two parameters. The first is repetition time or TR, the delay between succesive excitations. Differences in T_1 are amplified by using shorter values for TR, allowing less T_1 recovery, as shown in Fig. 2.9a. The second is echo time or TE, the delay between the excitation and the instant at which the gradient echo forms. Differences in T_2 are amplified by using longer values for TE, allowing more T_2 decay, as shown in Fig. 2.9b.

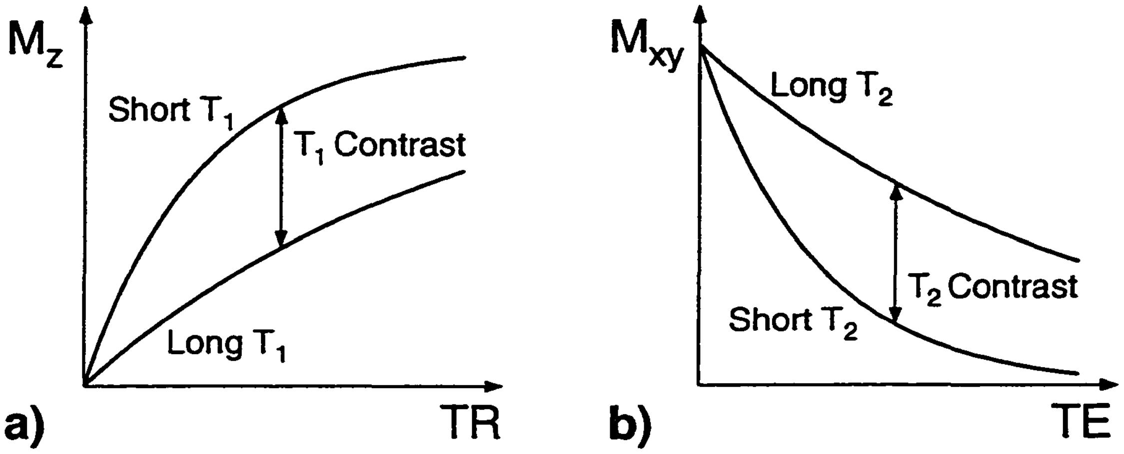

Figure 2.9: T_1 and T_2 contrast: (i) T_1 contrast between two species with different T_1s depends on TR and (ii) T_2 contrast between two species with different T_2s depends on TE.

2.5.2 Spin-echo imaging

For a given value of T_2, adequate T_2 weighting requires a TE on the order of T_2. However, some T_2 values may be long enough that, at the appropriate TE, off-resonance causes excessive signal loss in a gradient-recalled-echo sequence. This signal loss can be avoided by using spin-echo imaging which records spin echoes [24] rather than gradient echoes.

To consider how spin echoes are formed, it is first useful to visualize how off-resonance causes signal loss. This can be done with a rotating-frame model in which the frame of reference rotates at the Larmor frequency. In the laboratory frame which we have been using, the frequency of rotation is given by

$$\omega_{\mathrm{lab\_frame}} = \omega_0 + \Delta\omega \qquad (2.44)$$

where $\Delta\omega$ is the deviation of the resonant frequency from the Larmor frequency. In the rotating frame, the Larmor frequency is ignored and the frequency of rotation is given by

$$\omega_{\text{rotating\_frame}} = \Delta\omega \tag{2.45}$$

Therefore, in the rotating frame, when spins are tipped into the transverse plane, those that are exactly on-resonance remain stationary while those that are off-resonance rotate at a frequency, $\Delta\omega$. We will denote the transverse axes in this rotating frame by x' and y'.

Consider a number of spins with a range of resonant frequencies all

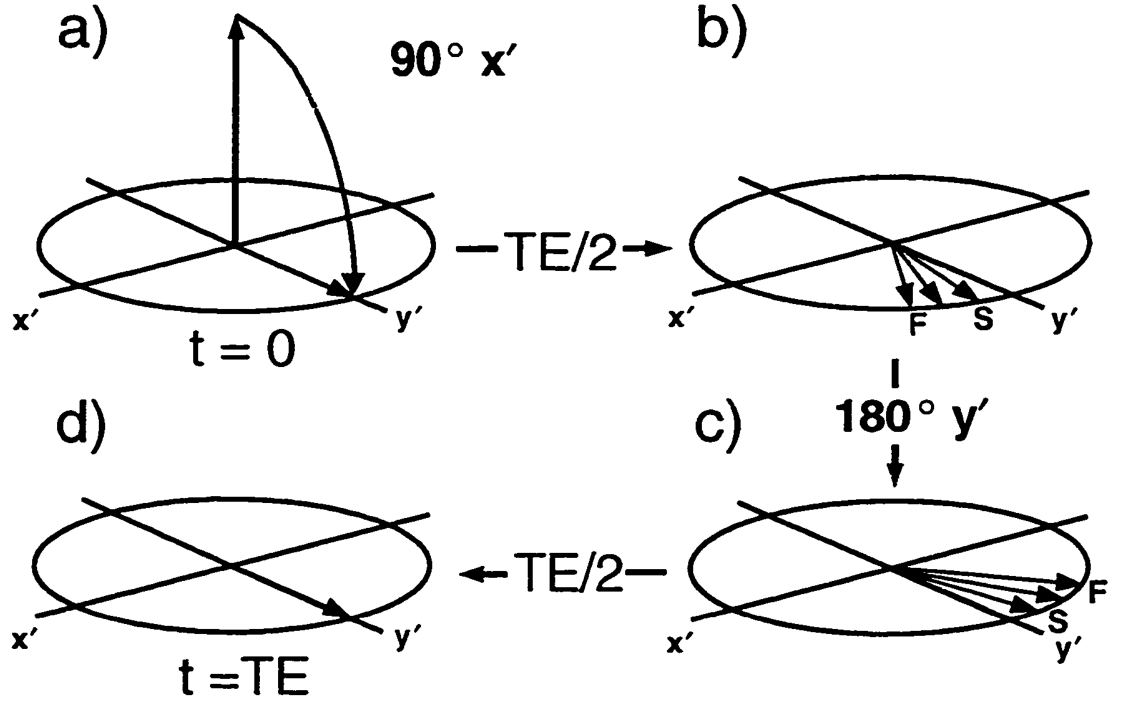

Figure 2.10: This sequence illustrates the principles of spin-echo formation in the rotating frame. (a) At time, t = 0, a 90° RF pulse tips the magnetization into the transverse plane. (b) At time, t = TE/2, variations in resonant frequency cause the spins to disperse. This dispersion decreases the net magnetic moment. (c) An additional 180° RF pulse rotates the spins about the x' axis. (d) At time, t = TE, the spins re-align, forming a spin echo.

higher than ω_0, as shown in Fig. 2.10. In this illustration, all gradient fields have been turned off. Immediately after a 90° RF excitation about the x' axis, all spins are aligned, as shown in Fig. 2.10a. After a time, TE/2, the spins are dispersed, as shown in Fig. 2.10b. The spins rotate in the clockwise direction with the spin labelled 'F' rotating faster than the spin labelled 'S.' If data is acquired at this time, there will be signal loss. Because MR images consist of macroscopically-sized voxels or volume elements, the signal from a particular voxel is given by the vector sum of the spins in that voxel. Phase variations in that voxel will reduce the magnitude of the vector sum.

To avoid this signal loss, a spin echo can be formed by using an additional 180° RF pulse to refocus off-resonant spins. Between Fig. 2.10b and Fig. 2.10c, this additional RF pulse rotates the spins 180° about the y' axis.

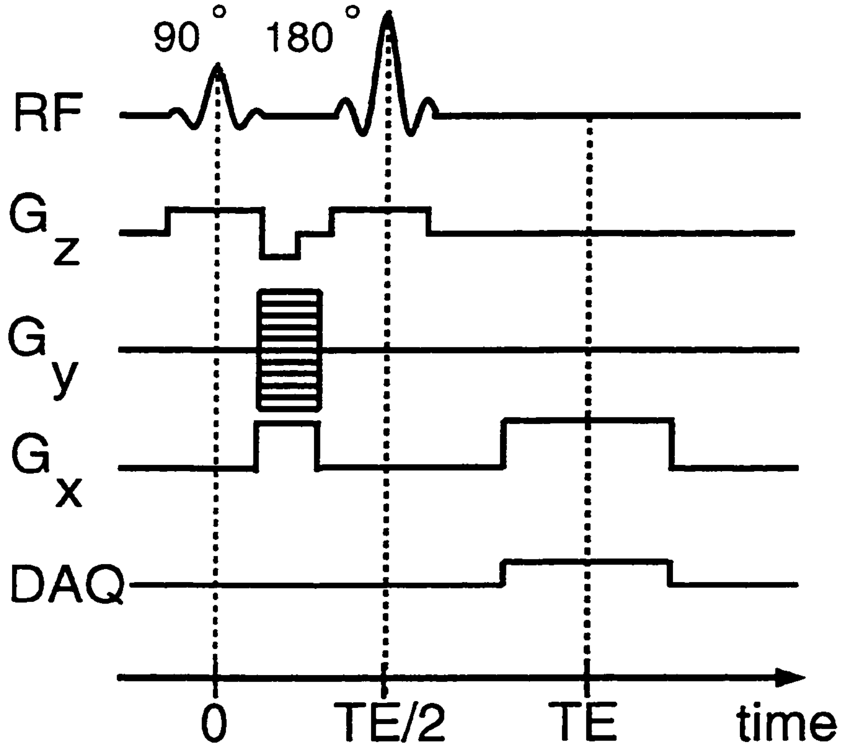

Figure 2.11: The gradient-recalled-echo imaging sequence shown earlier is transformed into a spin-echo sequence through the addition of a 180° RF pulse which refocuses off-resonant spins.

Between Fig. 2.10c and Fig. 2.10d, the spin labelled 'F' catches up to the spin labelled 'S.' Finally, in Fig. 2.10d, the spins are again aligned. This event is known as a spin echo and it occurs at a time, TE, after the initial 90° RF excitation.

The additional RF and gradient waveforms necessary in spin-echo imaging are shown in Fig. 2.11. An extra G_z lobe is used to make the 180° RF pulse slice-selective. Note that the G_y waveforms and the initial G_x waveform have been inverted. Since the 180° RF pulse flips the spins, gradients occuring before this 180° pulse must be inverted relative to their amplitudes in gradient-recalled-echo imaging.

2.5.3 Inversion nulling

Inversion nulling is a particular form of T_1 weighting which voids the signal from species with a given value of T_1. It uses a preparatory 180° excitation prior to the 90° excitation, as shown in Fig. 2.12. In spin-echo imaging, a 180° excitation is used to refocus magnetization already in the transverse plane. However, in inversion nulling, the 180° excitation is used to invert the longitudinal magnetization. A delay of TI between the 180° excitation and the 90° excitation allows the magnetization to recover along z, as shown in Fig. 2.12. Signal is produced when the 90° excitation tips the longitudinal magnetization into the transverse plane. However, for the value of T_1 that is to be nulled, the value of TI is chosen so that the longitudinal magnetization is zero at the time of the 90° excitation. Therefore, for this value of T_1, no magnetization is rotated into the transverse plane and no signal is produced. The 90°-180° sequence is repeated at intervals of TR.

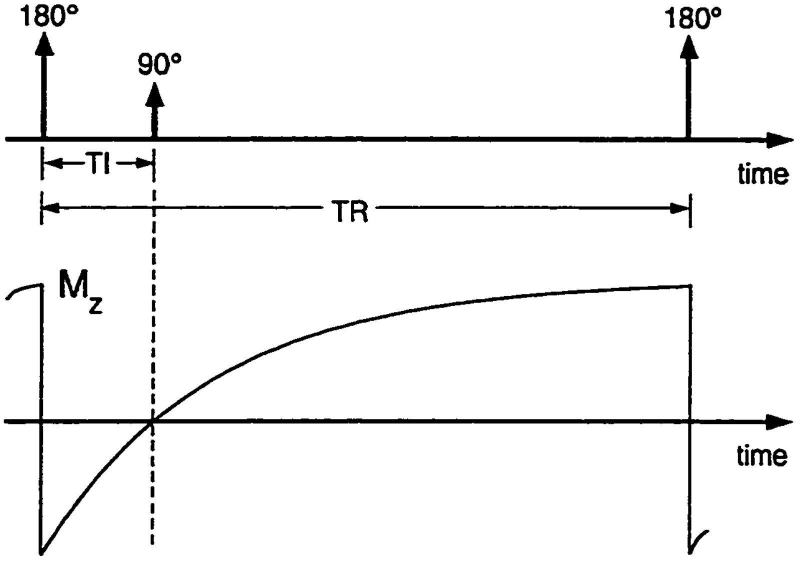

Figure 2.12: Inversion nulling: (a) A 180° pulse inverts the longitudinal magnetization, M_z. A time, TI, elapses for M_z recovery. At the time of the 90° pulse, M_z is zero. (b) Time course of M_z.

For example, it is often desirable to suppress the signal from fat because fat is rarely of clinical interest and its large chemical shift can produce artifacts. This can be done using inversion nulling since, at a field strength of 1.5 T, the T_1 of fat is about 260 ms while the T_1 of muscle is about 800 ms.

2.6 Summary

In summary, for ^1H protons, an external magnetic field creates a physical state for which there is a resonant frequency. If this state is disturbed by an RF pulse, signals are induced in a receiver coil at that resonant frequency. By using additional magnetic fields, we can make the resonant frequency vary linearly with position. Thus, MRI data is acquired in frequency space with spatial position being mapped to frequency. In other words, MRI data is acquired in frequency space or in the Fourier domain, allowing a linear-systems approach to MRI. This Fourier domain can be expanded to include not only spatial position but also motion and resonant frequency.

Chapter 3

Reducing Flow Artifacts In Echo-Planar Imaging

3.1 Introduction

Echo-planar imaging (EPI) is a fast imaging technique that was first proposed in 1977 [25]. Unlike the 2DFT imaging depicted in Fig. 2.7, EPI acquires several lines in *k*-space after each RF excitation by connecting the horizontal lines of Fig. 2.7 with vertical segments, as shown in Fig. 3.1. Therefore, EPI has a shorter scan time than conventional 2DFT imaging since it needs fewer excitations to acquire an image. However, because it was conceived as a single-shot technique which acquires all of its data after only a single RF excitation, its early use was hampered by poor spatial resolution, poor off-resonance properties and obtrusive ghosting [26].

Spatial resolution and off-resonance properties have been improved through the development of multi-shot or interleaved EPI [27-30], more powerful gradient systems and faster data sampling. Ghosting in EPI has been largely eliminated through the development of calibration techniques, as will be described in Appendix A, and through the use of shielded gradients [31].

The use of EPI for cardiac imaging revealed a sensitivity to flow artifacts [32, 33]. Even with interleaved EPI, the long data acquisition after each RF excitation encourages flow artifacts [34]. Using a multi-dimensional *k*-space which has velocity and resonant-frequency dimensions in addition to spatial dimensions, we analyzed these flow artifacts then searched for modifications of the EPI trajectory that would significantly reduce these artifacts. We will present two ways to improve the flow properties of EPI that exploit the relative importance of the data at the center of *k*-space.

First, we addressed artifacts due to flow in the readout direction or x direction. These can be reduced by using a "flyback" trajectory [35], which uses only the even echoes from the EPI echo train. Unfortunately, this approximately doubles the imaging time. We propose "partial-flyback" where, at the center of *k*-space, only even echoes are used and, elsewhere, both even and odd echoes are used. By adjusting the fraction of *k*-space acquired with flyback (the flyback ratio), we gained improved flow properties at the expense of slightly worse off-resonance properties and longer imaging time. We note that partial-flyback is similar in spirit to the work presented by Cao *et al.* [36] which addresses flow compensation in the phase-encode direction for 2DFT imaging.

Second, we addressed artifacts due to flow in the phase-encode direction or y direction. These can be reduced by using a partial *k*-space acquisition, which uses less phase-encoding before the center of *k*-space is acquired [33, 37]. Unfortunately, with partial *k*-space acquisition, synthesis of the missing data produces its own artifacts [38]. As an alternative, we used "inside-out" EPI where data collection begins at the center of *k*-space, with separate interleaves to acquire the top and bottom halves of *k*-space. This has better phase-encode flow properties than a partial *k*-space acquisition since there is less phase-encoding before the center of *k*-space is acquired. We note that some early EPI sequences began data acquisition at the center of *k*-space but only acquired one half of *k*-space [25, 39].

This chapter examines the flow and off-resonance properties of partial-flyback EPI and inside-out EPI. Section 3.3 defines the *k*-space trajectories discussed in this chapter and Section 3.2 presents the multi-dimensional *k*-space used to analyze flow and off-resonance properties. Sections 3.4, 3.5 and 3.6 respectively analyze the effects of readout flow, phase-encode flow and off-resonance. The choice of flyback ratio is discussed in Section 3.7. In Section 3.8, our implementation of the EPI trajectories is described and phantom and *in-vivo* results are shown in Section 3.9. The discussion in Section 3.10 includes a comparison of EPI and spiral imaging.

3.2 *k*-space trajectories

This section presents *k*-space diagrams of the EPI trajectories that will be considered in this chapter. These diagrams are intended as definitions of these trajectories. We note that interleaved EPI is used throughout this chapter and that our discussions are easily extended to single-shot EPI. Figures 3.1-3.2 show these trajectories. All trajectories start at the *k*-space origin, indicated by the black dot. The arrows indicate the k_x-direction during data acquisition.

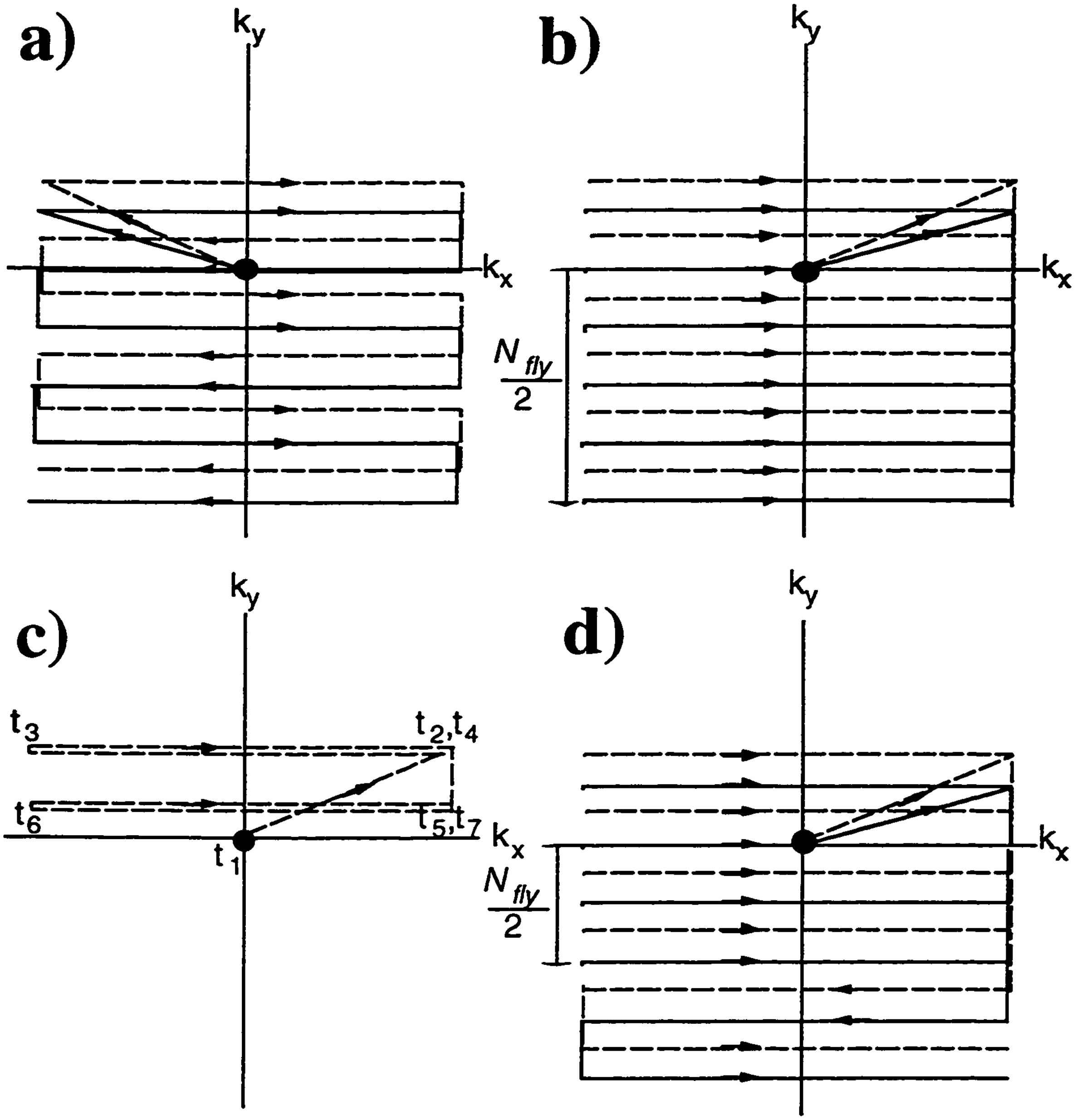

Figure 3.1: Partial-Fourier EPI trajectories that acquire 75% of k-space. Two interleaves are used with one interleaf drawn as a solid line and the other as a dashed line. The black dot indicates the k-space origin and the arrows indicate the k_x-direction during data acquisition. (a) No flyback. (b) 100% flyback. (c) More detailed look at how one interleaf of the 100% flyback trajectory acquires its first two data lines. t1 to t2: Trajectory moves to top-right corner of acquired k-space. t2 to t3: Flies back to left edge of k-space. t3 to t4: Acquires first data line. t4 to t5: Blips down, skipping a line which is acquired by the other interleaf. t5 to t6: Flies back to left edge of k-space. t6 to t7: Acquires second data line. (d) 50% flyback.

"Partial-Fourier EPI" denotes the use of partial k-space acquisition with EPI. A two-interleaf partial-Fourier EPI trajectory is depicted in Fig. 3.1a. One interleaf is drawn as a solid line and the other as a dashed line. Compared to a full k-space acquisition which begins at a corner of k-space, phase-encode flow artifacts are reduced because there is less phase-encoding before the center of k-space is acquired.

Flyback partial-Fourier EPI, depicted in Fig. 3.1b, reduces artifacts due to readout-flow by acquiring data in only one k_x-direction [35]. Note that all of the arrows in Fig. 3.1b point in the same direction. This trajectory is referred to as a flyback trajectory since, after acquiring one line of data, it "flies back" before acquiring another line of data. The even echoes are used since they enjoy far more velocity-compensation than the odd echoes. Figure 3.1c provides a more detailed look at how one interleaf acquires its first two data lines. From points t1 to t2, the trajectory moves to top-right corner of acquired k-space. From t2 to t3, it flies back to left edge of k-space. From t3 to t4, it acquires the first data line. From t4 to t5, it blips down, skipping a line which is acquired by the other interleaf. From t5 to t6, it flies back to left edge of k-space. From t6 to t7, it acquires the second data line.

The use of flyback with EPI approximately doubles the time to acquire an image. Therefore, we propose using "partial-flyback" where flyback is used only near the center of k-space. Figure 3.1d shows partial-flyback partial-Fourier EPI. In the bottom-half of k-space, $N_{fly}/2$ data lines are acquired with flyback and the rest are acquired without flyback. Note that the top-half of k-space is a truncated reflection of the bottom half about $k_y = 0$. By adjusting N_{fly}, imaging time can traded for reductions in flow artifacts.

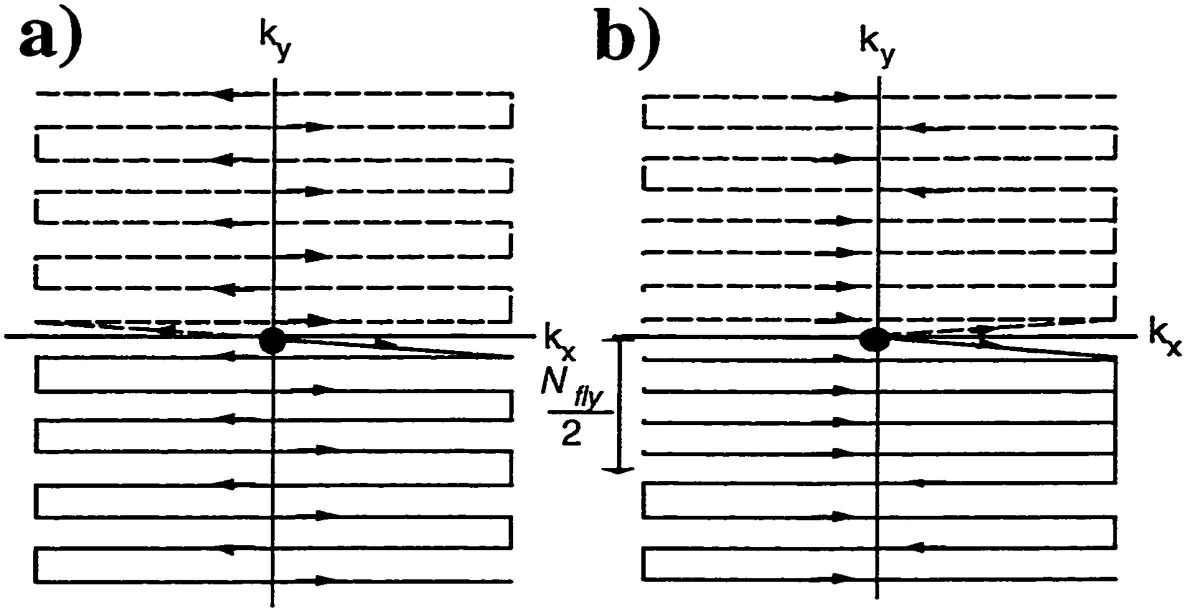

Figure 3.2: Inside-out EPI trajectories. Two interleaves are used with one interleaf drawn as a solid line and the other as a dashed line. One interleaf acquires the top-half of k-space and the other interleaf acquires the bottom-half. The black dot indicates the k-space origin and the arrows indicate the k_x-direction during data acquisition. (a) No flyback. (b) 50% flyback.

One problem with partial-Fourier EPI is that the missing data has to be synthesized, producing artifacts. We use "inside-out EPI" as an alternative to partial-Fourier EPI that does not require data synthesis. Furthermore, compared to partial-Fourier EPI, there is less phase-encoding before the center of k-space is acquired, reducing the phase-encode flow artifacts. As depicted in Fig. 3.2a, inside-out EPI begins data acquisition at the center of k-space, using separate interleaves to acquire the top and bottom halves of k-space. As with partial-Fourier EPI, artifacts from readout flow can be a problem. Partial-flyback is also applied to inside-out EPI and is shown in Fig. 3.2b. In each half of k-space, $N_{fly}/2$ data lines are acquired with flyback and the rest are acquired without flyback.

3.3 Multi-dimensional *k*-space

For the analysis of flow and off-resonance properties, we used a multi-dimensional *k*-space which has spatial dimensions, velocity dimensions and a resonant-frequency dimension, as described in Section 2.4. For flow properties, only velocity effects are shown although we will briefly discuss the effects of higher-order flow. Following Section 2.4, in the presence of flow [22] and off-resonance, the MRI signal equation can be written as:

$$s(t) = \int m(x,y,u,v,f)\, e^{-i2\pi[k_x(t)x + k_y(t)y + k_u(t)u + k_v(t)v + k_f(t)f]}\, dx\, dy\, du\, dv\, df \qquad (3.1)$$

where

x = readout-direction location
u = x-direction velocity
y = phase-encode-direction location
v = y-direction velocity
f = off-resonant frequency,

and

$$k_x(t) = \frac{\gamma}{2\pi}\int_0^t G_x(\tau)\, d\tau, \qquad (3.2)$$

$$k_y(t) = \frac{\gamma}{2\pi}\int_0^t G_y(\tau)\, d\tau, \qquad (3.3)$$

$$k_u(t) = \frac{\gamma}{2\pi}\int_0^t \tau\, G_x(\tau)\, d\tau, \qquad (3.4)$$

$$k_v(t) = \frac{\gamma}{2\pi}\int_0^t \tau\, G_y(\tau)\, d\tau, \qquad (3.5)$$

$$k_f(t) = \mathrm{t}. \qquad (3.6)$$

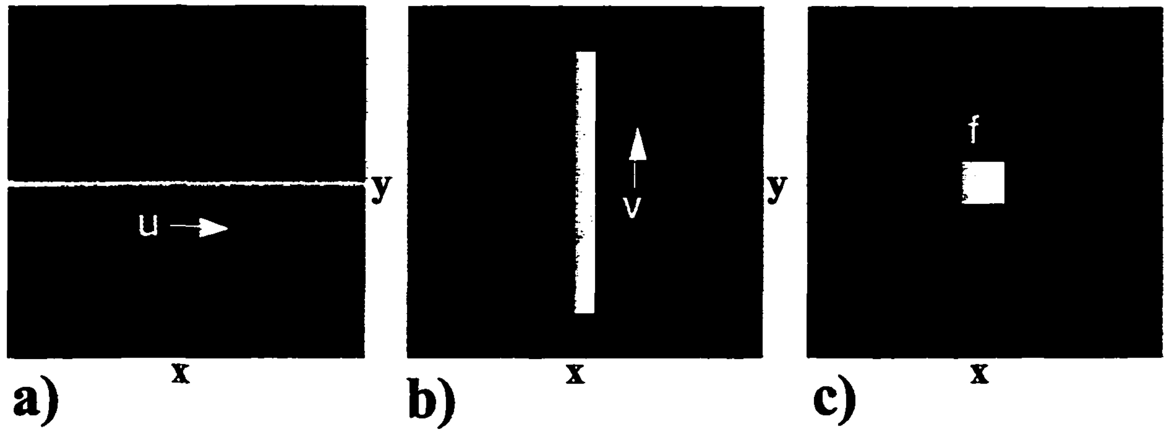

Figure 3.3: Ideal versions of the objects used to demonstrate flow and off-resonance properties. (a) A tube with readout-direction velocity, u, as indicated by the arrow. (b) A tube with phase-encode-direction velocity, v, as indicated by the arrow. (c) A square with an off-resonant frequency, f (no flow).

For each trajectory considered in this chapter, we will examine k_u, k_v and k_f and simulate their effects on simple objects. For reference, ideal versions of these objects are shown here. Figure 3.3a shows a tube with flow in the readout direction. It will be used to demonstrate readout-flow properties. Figure 3.3b shows the tube used to demonstrate phase-encode-flow properties; it has flow in the phase-encode direction. A square with no flow is shown in Fig. 3.3c and is used to demonstrate off-resonance properties.

3.4 Readout-flow properties

This section examines the artifacts due to readout flow in (i) partial-Fourier EPI with no flyback, (ii) partial-Fourier EPI with partial-flyback and (iii) inside-out EPI with partial-flyback. The number of interleaves is kept constant. For the partial-Fourier trajectories, the image-reconstruction method is described in Appendix B.

We will see why readout-direction flow produces ghosting and signal loss. Then we will then show how partial-flyback reduces these artifacts by being more careful about acquiring the important low spatial-frequency data.

3.4.1 Partial-Fourier EPI with no flyback

For EPI, k_u varies with both k_x and k_y. However, the effects of the k_x variation are negligible compared to those of the k_y variation. This is because the time required to traverse the desired k_y width is much longer than the time required to traverse the desired k_x width. Therefore, we can analyze the effects of k_u by examining its profile along the k_y-axis. For partial-Fourier EPI with no flyback, Fig. 3.4a shows k_u along the k_y-axis for a sixteen-interleaf sequence. There are three effects:

1. The periodicity of k_u produces ghosting in the image. This periodicity is due to the left-right alternation of the k_x-direction.
2. The non-zero values of k_u produce signal loss. There is intra-voxel dephasing when a range of velocities is present in one voxel.
3. The non-zero values of k_u produce ghosting. Velocity variations from TR to TR produce phase variations in k_y which result in ghosting.

Figure 3.5a shows a simulated image of a tube in the readout direction with constant-velocity flow of 25 cm/s. Since only one velocity is simulated, signal loss due to velocity dephasing and ghosting caused by TR-to-TR velocity variations are not revealed. However, the ghosting is very evident.

Higher-order flow such as acceleration and jerk also causes ghosting and signal loss. Along the k_y-axis, the higher-order moments of the readout gradient also oscillate. For example, along k_y, the second moment oscillates between positive and negative values while its absolute value increases linearly with k_y.

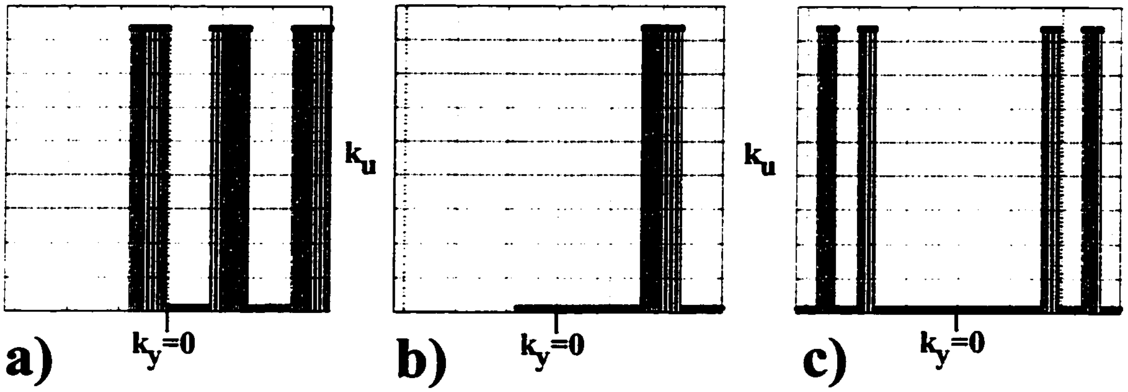

Figure 3.4: Readout-flow properties: k_u vs. k_y for k_x=0. Simulation parameters are: image size of 128x128, 16 interleaves, 80 lines acquired for the two partial-Fourier trajectories, 64 flyback lines for the two partial-flyback trajectories. (a) No-flyback partial-Fourier EPI: The periodicity of k_u produces ghosting and signal loss in the image. (Since this is a partial-Fourier acquisition, k_u does not have values for all of k_y < 0.) (b) Partial-flyback partial-Fourier EPI: Partial-flyback reduces the periodicity of k_u near the center of k-space and thus reduces ghosting in the image. (c) Partial-flyback inside-out EPI: Partial-flyback reduces the periodicity of k_u near the center of k-space.

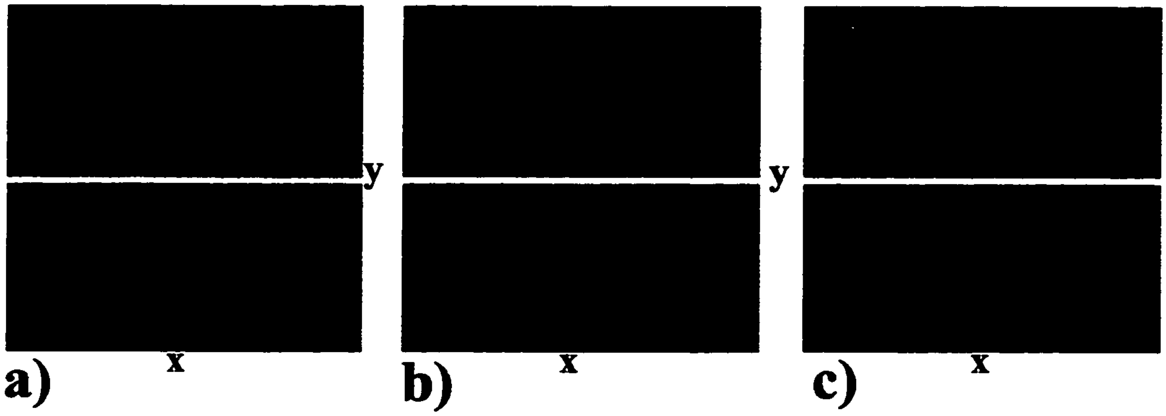

Figure 3.5: Readout-flow properties: Simulated images of a tube with constant-velocity flow of 25 cm/s in the readout direction. The ideal object is shown in Fig. 3.3a. Simulation parameters are the same as in Fig. 3.4. (a) No-flyback partial-Fourier EPI: The image shows severe ghosting. 11.0 ms readout per interleaf. (b) 50% flyback partial-Fourier EPI: Partial-flyback reduces ghosting in the image. 16.5 ms readout per interleaf. (c) 50% flyback inside-out EPI: Partial-flyback reduces ghosting in the image. 26.4 ms readout per interleaf.

3.4.2 Partial-Fourier EPI with partial-flyback

For partial-Fourier EPI where 50% of k-space is acquired with flyback, Figure 3.4b shows k_u along the k_y-axis. Near the center of k-space, k_u is not periodic and is almost zero. This reduces all three effects described in Section 3.4.1:

1. k_u is not periodic for low values of k_y. Hence, for the low spatial frequencies, readout-flow causes no ghosting.
2. k_u is almost zero for low values of k_y. Hence, for the low spatial frequencies, readout-flow causes negligible signal loss.
3. k_u is almost zero for low values of k_y. Hence, for the low spatial frequencies, TR-to-TR variations in readout-flow cause negligible ghosting.

In Fig. 3.5b, the simulated-tube image shows that ghosting is greatly reduced. There is some ghosting of the high-spatial frequencies but no ghosting of the important low spatial frequencies. Since only one velocity is simulated, the reduction in signal loss and the reduction in ghosting from TR-to-TR velocity variations are not revealed.

For the tube in Fig. 3.5b, ninety-five percent of the energy in k-space is contained within the flyback region. Therefore, to reduce readout-flow artifacts, it is sufficient to use a flyback ratio of less than 100%. The choice of flyback ratio will be discussed in Section 3.7.

Partial-flyback also reduces the ghosting due to higher-order flow since, at the low spatial frequencies, there is no oscillation of the higher-order moments along the k_y-axis.

3.4.3 Inside-out EPI with partial-flyback

One problem with partial-Fourier EPI is that the missing data has to be synthesized as described in Appendix B, producing artifacts. As an alternative to partial-Fourier EPI, inside-out EPI has two advantages. First, it does not use partial *k*-space acquisition and so does not require data synthesis. Second, and more significantly, it has superior phase-encode flow properties. The phase-encode flow properties will be discussed in Section 3.5.3. This section examines the readout flow properties.

As with partial-Fourier EPI, the use of partial-flyback with inside-out EPI can significantly reduce the ghosting and signal loss due to readout-flow. For inside-out with 50% flyback, Fig. 3.4c shows k_u along the k_y-axis for a sixteen-interleaf sequence. Figure 3.5c shows the simulated image of the tube with readout flow. As in Section 3.4.2, the ghosting is virtually eliminated with 50% flyback. Again, since only one velocity is simulated, the reduction in signal loss and the reduction in ghosting from TR-to-TR velocity variations are not revealed.

For higher-order flow properties, the comparison between partial-Fourier EPI and inside-out EPI is similar to the comparison for velocity properties.

3.5 Phase-encode-flow properties

This section examines the artifacts due to phase-encode flow for the three trajectories used in Section 3.4. We will show why flow in the phase-encode direction produces signal loss. Then we will show that inside-out EPI has less signal loss because it begins data acquisition at the center of *k*-space.

3.5.1 Partial-Fourier EPI with no flyback

For EPI, k_v varies only with k_y. and not at all with k_x. This is because the y gradient is inactive while k_x is changing. For partial-Fourier EPI with no flyback, Fig. 3.6a shows k_v versus k_y. There are three effects:

1. The curvature of k_v produces some blurring and ringing.
2. The non-zero values of k_v produce signal loss when a range of velocities is present in one voxel.
3. The non-zero values of k_v produce ghosting. Velocity variations from TR to TR produce phase variations in k_y which result in ghosting.

There are small discontinuities in k_y because of differences between the interleaves. However, the resulting ghosting is negligible since the discontinuities have been greatly reduced by the sliding readout delays used to avoid off-resonance ghosting, as described in Section 3.8.1.

Figure 3.7a shows a simulated image of a tube in the phase-encode direction with constant-velocity flow of 25 cm/s. The blurring and ringing are visible only at the y-edges of the tube. Within the tube, these effects are inconspicuous since they are in the direction of the flow. Velocity compensation is used to make k_v=0 at k_y=0 which would minimize signal loss due to velocity dephasing and ghosting caused by TR-to-TR velocity variations. However, the effect of velocity compensation is not demonstrated since only one velocity is simulated.

In more realistic situations, while velocity-compensation reduces signal loss due to velocity, it worsens the artifacts from higher-order flow. Because of interleaving, the higher-order moments have discontinuties which produce ghosting. With velocity-compensation, the discontinuties are larger and produce more ghosting.

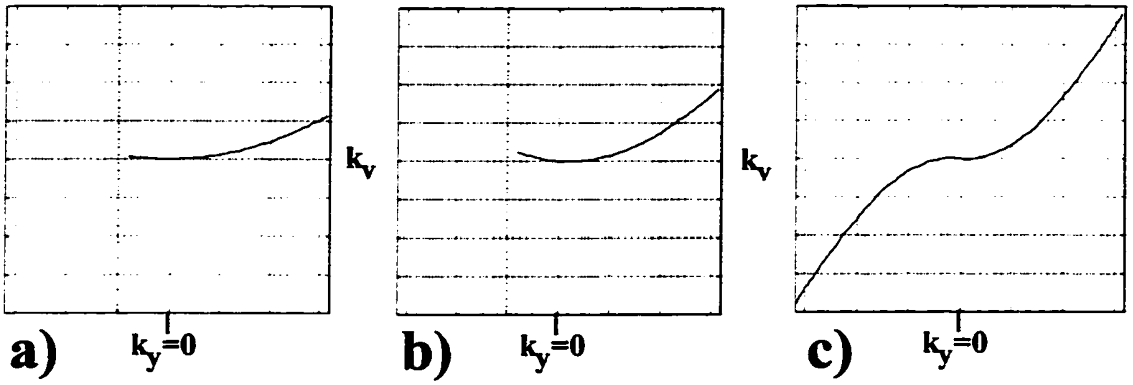

Figure 3.6: Phase-encode-flow properties: k_v vs. k_y. Simulation parameters are the same as in Fig. 3.4. (a) No-flyback partial-Fourier EPI: The curvature of k_v produces blurring and ringing in the image but these effects are inconspicuous. (Since this is a partial-Fourier acquisition, k_v does not have values for all of $k_y < 0$.) (b) Partial-flyback partial-Fourier EPI: There is more curvature of k_v than with no-flyback. (c) Partial-flyback inside-out EPI: There is even more curvature of k_v than with partial-Fourier EPI.

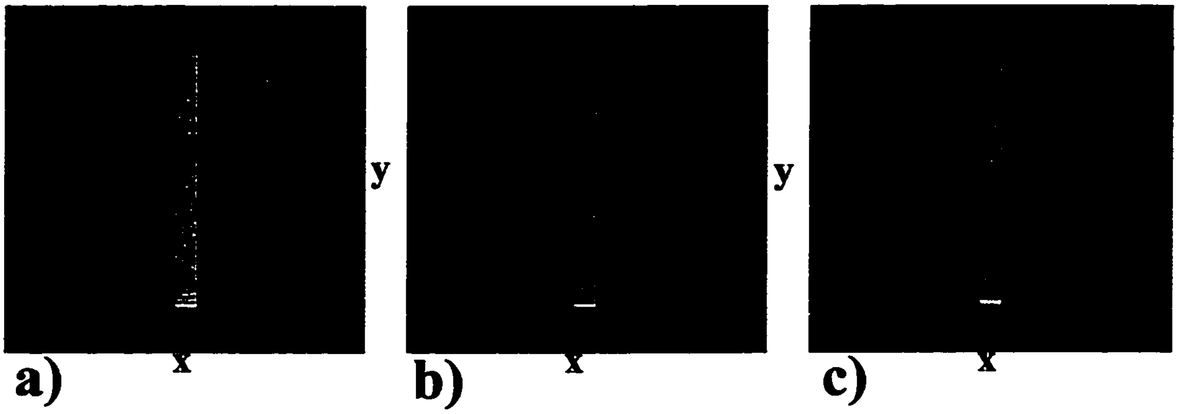

Figure 3.7: Phase-encode-flow properties: Simulated images of a tube with constant-velocity flow of 25 cm/s in the phase-encode direction. The ideal object is shown in Fig. 3.3b. Simulation parameters are the same as in Fig. 3.4. (a) No-flyback partial-Fourier EPI: The blurring and ringing are inconspicuous except at the y-edges. (b) Partial-flyback partial-Fourier EPI: Slightly more blurring and ringing than with no-flyback. (c) Partial-flyback inside-out EPI: Somewhat more blurring and ringing than with partial-Fourier EPI.

3.5.2 Partial-Fourier EPI with partial-flyback

While partial-flyback improves the readout flow properties, for a constant number of interleaves, it increases the data acquisition time per interleaf. This slightly worsens the phase-encode flow properties.

For partial-Fourier EPI with 50% flyback, Fig. 3.6b shows k_v versus k_y. Because of the longer data acquisition time, k_v has greater curvature and a larger maximum value. This produces slightly more blurring and ringing, as shown in Fig. 3.7b.

The longer data acquisition time also increases the curvature and amplitude of the higher-order moments, producing more blurring and ringing. Second, the longer TE increases the size of the discontinuities in the moments, producing more ghosting. Therefore, as the flyback ratio increases, flow in the phase-encode direction produces worse artifacts.

3.5.3 Inside-out EPI with partial-flyback

Compared to partial-Fourier EPI, inside-out EPI suffers less from phase-encode flow artifacts because there is less phase-encoding before the center of k-space is acquired.

For inside-out EPI with 50% flyback, Fig. 3.6c shows k_v versus k_y. Compared to Fig. 3.6b, k_y has greater curvature and a larger maximum value. Consequently, Fig. 3.7c shows more blurring and ringing at the y-edges of the tube than Fig. 3.7b.

This is because inside-out EPI has a longer "effective readout time" than partial-Fourier EPI. We define the effective readout time as the time to travel from the top of k-space to the bottom of k-space. For our 50% flyback inside-out sequence, each interleaf has a data acquisition time of 26.4 ms. This is the time to traverse 50% of *k*-space. Hence the effective readout time from top to bottom is (2 x 26.4) or 52.8 ms. For our 50% flyback partial-Fourier sequence, each interleaf has a data acquisition time of 16.5 ms. This is the time to traverse 62.5% of *k*-space. Hence the effective readout time is (100/62.5 x 16.5) or 26.4 ms.

A consideration of the higher-order flow is important. For partial-Fourier EPI, there is more gradient action before the center of *k*-space is acquired. This increases the values of the higher-order gradient moments at $k_y=0$, producing more signal loss. The extra gradient action also increases the size of the discontinuities in the moments, producing more ghosting.

3.6 Off-resonance properties

This section examines the artifacts due to off-resonance in partial-Fourier EPI with no flyback, partial-Fourier EPI with partial-flyback and inside-out EPI with partial-flyback. We will see off-resonance causes a shifting of the image for partial-Fourier EPI and blurring or ghosting for inside-out EPI.

3.6.1 Partial-Fourier EPI with no flyback

For EPI, k_f varies with both k_x and k_y. However, the time required to traverse the desired k_y width is much longer than the time required to traverse the desired k_x width. Therefore, we can usually ignore the k_f evolution along k_x since this produces x-shifts of much less than one pixel [40]. For partial-Fourier EPI with no flyback, Fig. 3.8a shows k_f versus k_y. There are two effects:

1. The slope produces shifts and density changes in the phase-encode direction.
2. The non-zero values of k_f produce signal loss when there is a range of off-resonances in one voxel. This is more commonly described as T_2^* decay.

Figure 3.9a shows a simulated image of a square with 30 Hz off-resonance. The shift of the square is a fairly benign effect. Since only one off-resonant frequency is simulated, signal loss due to off-resonance is not revealed.

3.6.2 Partial-Fourier EPI with partial-flyback

With partial-flyback, off-resonance properties worsen because of the abrupt change between the flyback region and the non-flyback region.

For 50% flyback partial-Fourier EPI, Fig. 3.8b shows k_f versus k_y. The most obvious feature is the change in slope where the flyback region ends. This occurs because, in the flyback region, we travel along k_y at half the speed that we do in the non-flyback region. There are three effects on the image:

1. The slope change produces blurring since the high spatial-frequencies are shifted by half as much as the low spatial frequencies.
2. The larger slope of k_f in the flyback region produces larger shifts in the phase-encode direction.
3. The larger values of k_f can produce more signal loss (more T_2^* decay).

Figure 3.9b shows a simulated image of a square with 30 Hz off-resonance. For this amount of off-resonance, there is little difference from Fig. 3.9a.

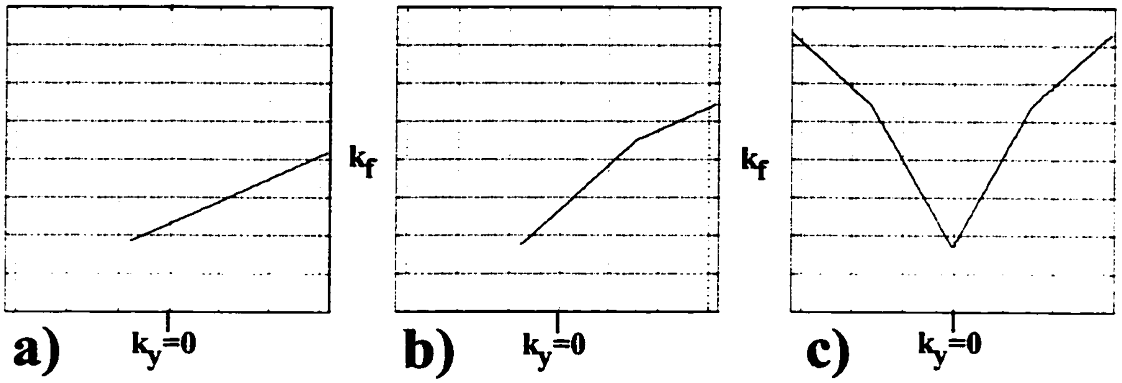

Figure 3.8: Off-resonance properties: k_f vs. k_y. Simulation parameters are the same as for Fig. 3.4. (a) No-flyback partial-Fourier EPI: The slope of k_f produces a shift of the image in the phase-encode direction - a fairly benign effect. (b) Partial-flyback partial-Fourier EPI: The change in slope of k_f causes slight blurring in the image. (c) Partial-flyback inside-out EPI: The change in slope at k_y =0 causes blurring in the image.

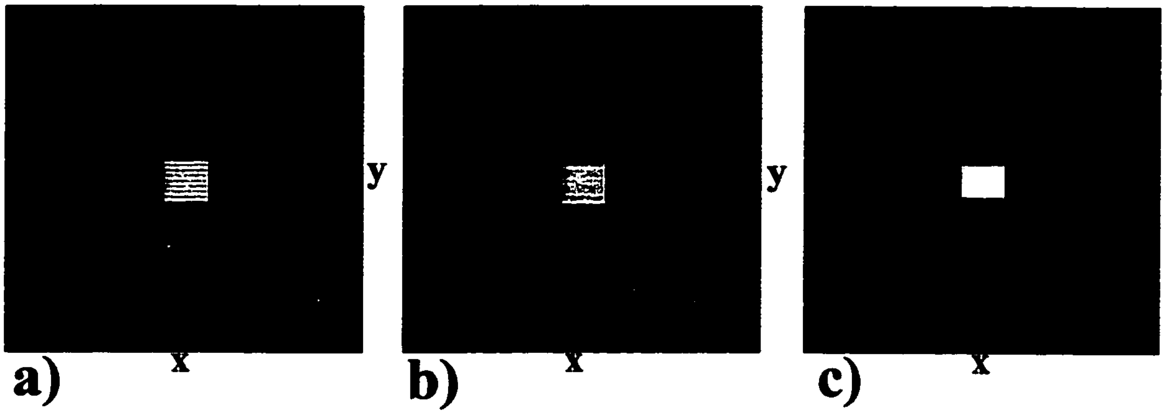

Figure 3.9: Off-resonance properties: Simulated images of a square with 30 Hz off-resonance. The ideal object is shown in Fig. 3.3c. Simulation parameters are the same as for Fig. 3.4. (a) No-flyback partial-Fourier EPI: The shift of the image in the phase-encode direction is inconspicuous. (b) Partial-flyback partial-Fourier EPI: For this amount of off-resonance, there is little difference from the no-flyback case. (c) Partial-flyback inside-out EPI: The image shows blurring.

With a larger flyback ratio, the values of k_f are larger, producing more signal loss. However, there may be less blurring if the slope-change moves out of the high-amplitude part of k-space. See Section 3.7 for more details.

3.6.3 Inside-out EPI with partial-flyback

For inside-out EPI, off-resonance produces worse geometric distortion but less signal loss than partial-Fourier EPI. Starting data acquisition at the center of k-space produces an abrupt change at the center of k-space but also results in a shorter TE.

For 50% flyback inside-out, Fig. 3.8c shows that k_f versus k_y resembles a 'v' shape. This is because the inside-out k-space trajectory travels in both the positive and negative k_y directions. Consequently, one half of k-space forms an image which is shifted in one y-direction while the other half of k-space forms an image which is shifted in the other y-direction. Figure 3.9c shows the resultant blurring of the image.

Hence, for inside-out EPI, off-resonance produces more annoying geometric distortion than for partial-Fourier EPI. It is imperative to reduce this distortion during image reconstruction. Traditional correction schemes [41] cannot be applied since the artifacts are not simple shifts in the y-direction. Instead, we apply the method proposed by Noll *et al.* [42] for trajectories such as circular spirals and projection reconstruction. For each image voxel, a field map is used to estimate the resonant frequency and any off-resonant phase in k-space is removed. Following Noll *et al.* [42], the reconstruction time is reduced by ignoring the off-resonant phase evolution along k_x. Further details can be found in Luk Pat *et al.* [43].

On the other hand, inside-out's off-resonance properties are superior to partial-Fourier's in one respect. A comparison of Fig. 3.8c with Fig. 3.8b shows that inside-out's shorter TE produces a smaller value of k_f at $k_y = 0$. This means that off-resonance produces more signal loss for partial-Fourier than for inside-out.

3.7 Choosing the flyback ratio

The flyback ratio should be just large enough to yield good readout-flow and off-resonance properties but no larger; otherwise, the phase-encode-flow properties will be unnecessarily degraded. For good readout-flow and off-resonance properties, the flyback region should acquire a large fraction of the energy in *k*-space. Fortunately, most of the energy in *k*-space is typically found near the *k*-space origin.

It is difficult to quantify the effect of the flyback ratio. One possibility is to measure the difference between an ideal object and an object imaged with partial-flyback EPI. However, this can be misleading since the results depend on the object, the imaging trajectory and the sequence parameters. Nevertheless, some insight can be gained by simulating the simple tube of Fig. 3.4 with readout flow.

For the simulated tube of Fig. 3.4, a plot of the k-space energy within the flyback region versus the flyback ratio is shown in Fig. 3.10a. Figure 3.10b shows the relative error-energy versus flyback ratio for the simulation parameters of Section 3.4.3. The error-energy, ε, for a given flyback ratio, r, is defined as

$$\varepsilon(r) = \int (|m_{simulated}| - |m_{ideal}|)^2 \, dx \, dy \tag{3.7}$$

where

$m_{simulated}$ = simulated image of tube with x-velocity artifacts,

m_{ideal} = ideal image of tube.

The relative error-energy is defined as

$$\frac{\varepsilon(r)}{\varepsilon(r=0)}. \tag{3.8}$$

We found that a relative error-energy of 15% represents an image with very little artifact from readout flow and off-resonance. Figure 3.10 shows that the relative error-energy is reduced to 12% when the flyback region contains 95% of the energy in k-space. This corresponds to a flyback ratio of 50%.

For images of a tube, we propose the following criterion for choosing the flyback ratio: The flyback region should contain 95% of the energy in k-space. For a tube-width of 3 pixels, Figs. 3.10a-3.10b validate this criterion. For tube-widths of 8 pixels or less, we found that the proposed criterion limits the relative error-energy to 15%. Figure 3.10c shows the flyback ratios for various tube-widths as selected by the proposed criterion.

For general images, we argue that the criterion still applies: For a general image, the flyback ratio should depend on the object that is narrowest in the phase-encode direction. For this narrowest object, a tube of similar width is a reasonable model. Since the narrowest widths are typically 8 pixels or less, our proposed criterion applies to general images.

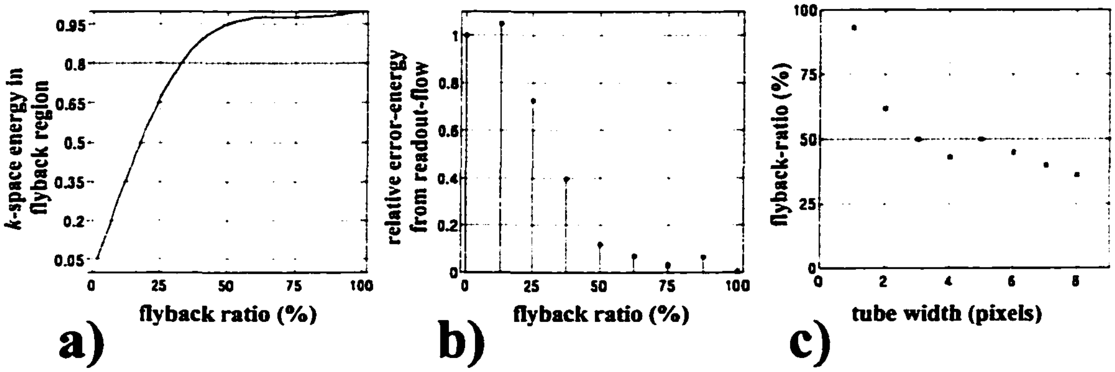

Figure 3.10: Effect of the flyback-ratio on the readout flow properties of partial-flyback inside-out EPI. Simulation parameters are the same as in Fig. 3.4. Tube-width in the phase-encode direction is 3 pixels in a and b and variable in c. (a) Fraction of the total *k*-space energy in the flyback region versus the flyback ratio. 95% of the energy in *k*-space is contained within the central 50% of *k*-space. (b) The relative error-energy versus the flyback ratio. For a flyback ratio of 50%, the relative error-energy is reduced to 12%. See Eqs. 3.7-3.8 for a definition of the relative error-energy. (c) The flyback ratio versus the tube width. The flyback ratio is chosen so that 95% of the *k*-space energy is in the flyback region.

Throughout this chapter, we assumed our images contained objects that were no narrower than 3 pixels. Consequently, Fig. 3.10c indicated a flyback ratio of 50%.

3.8 Implementation

We implemented the various EPI sequences on a GE Signa 1.5 T system. We used a gradient amplitude of 15 mT/m and a slew rate of 20 mT/m/ms. For all sequences, we used exponential ramps [44] and sampling on the G_x ramps to achieve shorter scan times than with linear ramps and no sampling on the G_x ramps. With exponential ramps, we achieved an average slew rate of 29 mT/m/ms which is about 50% greater

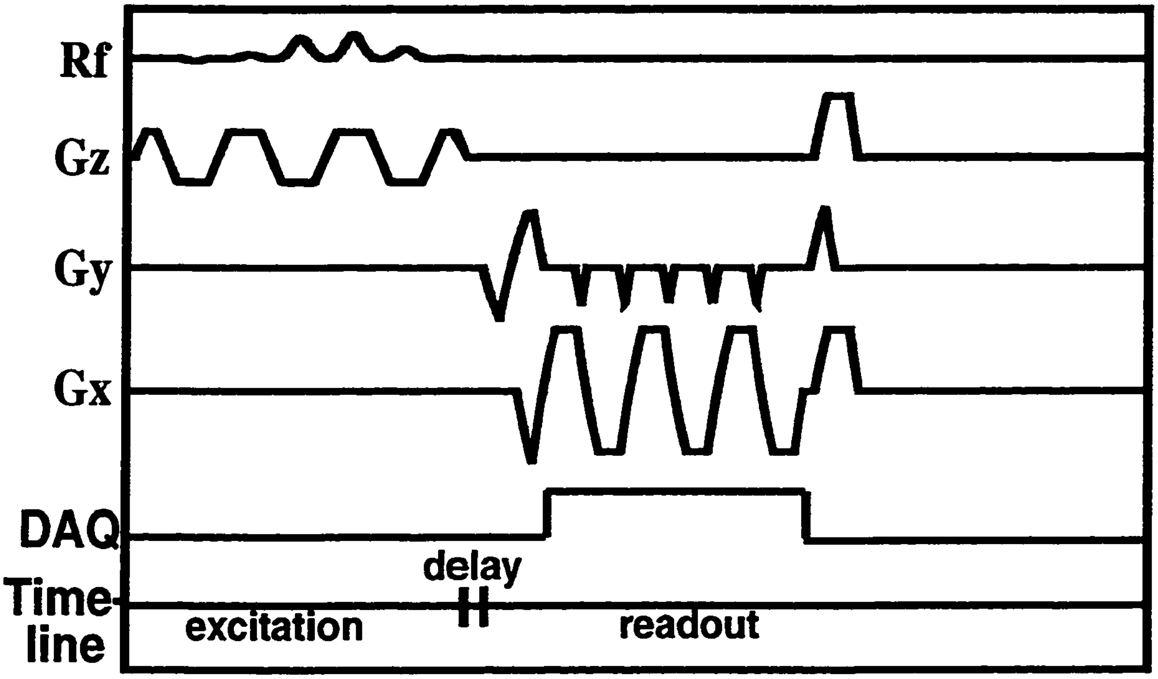

Figure 3.11: Pulse sequence diagram for no-flyback partial-Fourier EPI. This diagram corresponds to one interleaf of the trajectory in Fig. 3.1a. Six echoes are acquired after the RF excitation.

than with linear ramps. With sampled exponential ramps, our scan times were about 65% of the scan times with non-sampled linear ramps. We note that sampling on the ramps requires *k*-space interpolation. However, interpolation techniques are well understood and are computationally inexpensive [45].

3.8.1 No-flyback partial-Fourier EPI

Figure 3.11 shows the pulse sequence diagram for partial-Fourier EPI with no flyback. The RF and G_z axes depict the spectral-spatial RF excitation used for fat-suppression [46]. The waveform on the G_y axis begins with the bipolar lobe used for velocity compensation [32]. The DAQ axis shows that data is acquired during both positive and negative G_x trapezoidal lobes. A

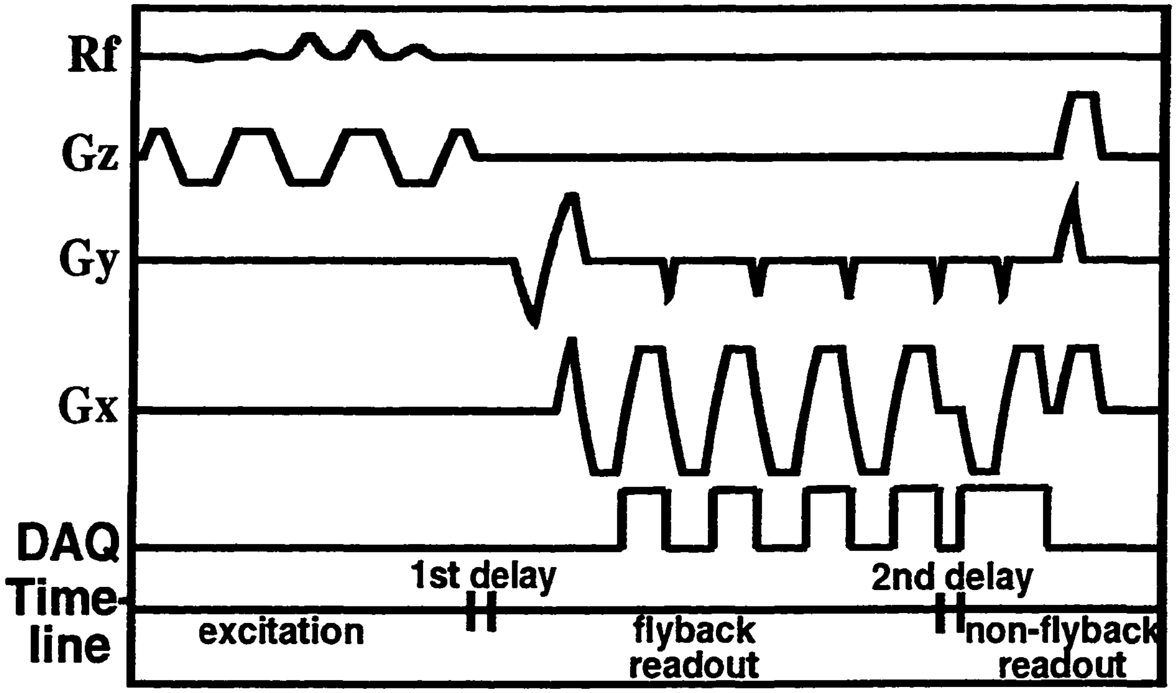

Figure 3.12: Pulse sequence diagram for 50% flyback partial-Fourier EPI. This diagram corresponds to one interleaf of the trajectory in Fig. 3.1d. Six echoes are acquired after the RF excitation, four with flyback.

single readout delay is used to reduce ghosting due to off-resonance [27, 30] and phase-encode flow. This delay occurs just after the spectral-spatial excitation and its duration is given in Appendix C. Transverse coherence artifacts are minimized by the use of a G_y rewinder, G_x and G_z killers and RF spoiling [47].

3.8.2 Partial-flyback partial-Fourier EPI

Figure 3.12 shows the pulse sequence diagram for partial-Fourier EPI with 50% flyback. The RF and G_z axes are the same as in Fig. 3.11. However, the DAQ axis now indicates a distinction between the flyback and non-flyback regions. For the flyback region, data is acquired only during the positive G_x trapezoids. A G_y blip occurs only after a positive G_x trapezoid. For the non-

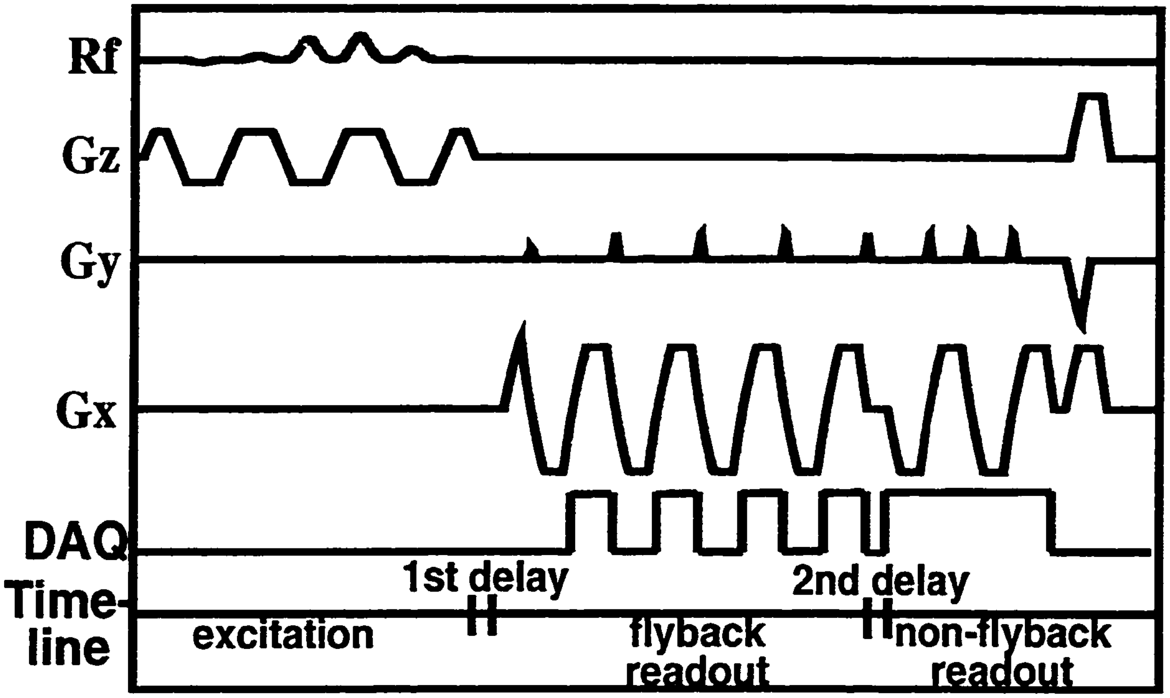

Figure 3.13: Pulse sequence diagram for 50% flyback inside-out EPI. This diagram corresponds to one interleaf of the trajectory in Fig. 3.2b. Eight echoes are acquired after the RF excitation, four with flyback.

flyback region, data is acquired during both positive and negative G_x trapezoids. A G_y blip occurs after every G_x trapezoid. For partial-flyback, two readout delays are used. The first delay occurs between the RF excitation and the readout waveforms. The second readout delay occurs between the last G_x flyback lobe and the first G_x non-flyback lobe. These delays are given in Appendix C. Note that a G_y blip occurs between the last G_x flyback lobe and the second readout delay. This makes k_v smoother than if the blip were placed after the second readout delay.

3.8.3 Partial-flyback inside-out EPI

Figure 3.13 shows the pulse sequence diagram for inside-out EPI with 50% flyback. Again, the RF and G_z axes are the same as in Fig. 3.11. The G_x

and DAQ axes are similar to those in Fig. 3.12, showing the flyback and non-flyback regions. However, the waveform on the G_y axis begins with a small unipolar lobe. Since data acquisition begins near the center of *k*-space, no velocity compensation is used. Again, two readout delays are used. Their durations are somewhat different than for partial-flyback partial-Fourier EPI and are given in Appendix C.

3.8.4 Positive-negative lobe ghosting

For any EPI trajectory, differences between the positive and negative gradient lobes can cause ghosting. To reduce this ghosting, we acquire calibration data with an RF excitation that precedes the imaging interleaves. This calibration acquisition uses the imaging pulse waveforms with the G_y waveform turned off [48]. Our use of this calibration data is described in detail in Appendix A.

For inside-out EPI requires not only correction of the differences between the even and odd echoes but also correction of the differences between the top and bottom halves of *k*-space. This top-bottom correction is described in Appendix A.

For partial-Fourier EPI, we observed that number of interleaves should exactly divide both the the number of phase encodes actually acquired and the number of phase encodes desired. For example, for the parameters given in the caption of Fig. 3.4, the number of interleaves, 16, exactly divides both the the number of phase encodes actually acquired, 80, and the number of phase encodes desired, 128. If either requirement is unsatisfied, there will be ghosting.

3.8.5 Field-map acquisition

With all sequences, a field map is derived from two low-resolution images each with different TEs. These images are acquired using the excitations preceding the imaging interleaves. This does not increase the scan time since these excitations are normally used to establish magnetization equilibrium. The field map sequence is partial-flyback inside-out EPI with two interleaves. The use of inside-out avoids spatial misregistration between the field map and the uncorrected image. The use of partial-flyback avoids signal loss due to flow. In all, four excitations are required for the field map: two for the first map image and two for the second map image.

3.9 Results

Here we present both flow-phantom images and cardiac images. Figure 3.14 shows images of two tubes and two bottles. In the tubes, there is pulsatile flow in the directions indicated by the arrows. In the bottles, there is no flow but there are signal voids caused by an air bubble in the center of each bottle. Data acquisition was gated to the pulsatile flow. Figure 3.14a was acquired with no-flyback partial-Fourier EPI. Flow ghosting replaces each tube with two strong ghosts and a number of weaker ghosts. In Fig. 3.14b, the use of 50% flyback effects a dramatic reduction in the flow ghosting. This shows that, for flow in the readout direction, partial-flyback reduces ghosting for higher-order flow as well as constant-velocity flow. Figure 3.14c was acquired with 50% flyback inside-out EPI. The B_0-inhomogeneity correction described in Luk Pat *et al.* [43] works well here but still leaves some blurring of the bottle corners. These results correspond well with the simulations of Section 3.4.

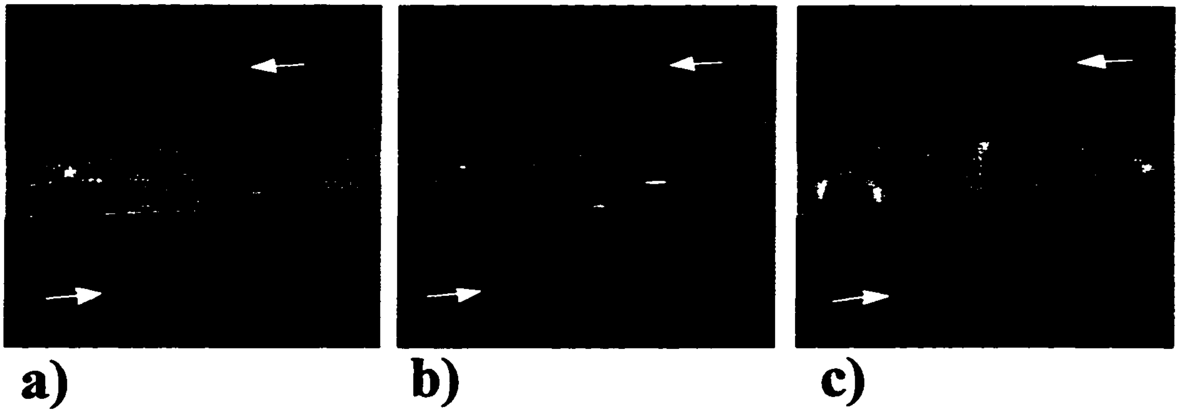

Figure 3.14: Images of two tubes and two bottles. In the tubes, there is pulsatile flow in the directions indicated by the arrows. In the bottles, there is no flow but there are signal voids caused by an air bubble in the center of each bottle. The use of 50% flyback dramatically reduces the flow ghosting. (a) No-flyback partial-Fourier EPI. (b) 50% flyback partial-Fourier EPI. (c) 50% flyback inside-out EPI. For each image, in-plane resolution is 1.2 mm, slice thickness is 10 mm and 16 interleaves were used with effective readout times per interleaf of 17.6 ms, 26.4 ms and 52.8 ms respectively. For the partial-Fourier images, 62.5% of *k*-space was acquired.

Figure 3.15 shows breath-held axial images of the heart of a normal volunteer acquired in late diastole. Figure 3.15a was acquired with no-flyback partial-Fourier EPI. Readout-flow artifacts appear as signal loss and ghosting along the septum and just inferior to the mitral valve. Figure 3.15b was acquired with 50% flyback partial-Fourier EPI. Here, the ghosting is eliminated and the signal loss is reduced. However, around the posterior edge of the heart, there is some ghosting and more signal loss than with no flyback. This is because of the worsened phase-encode flow properties. Nevertheless, the overall image quality improves with partial-flyback. Figure 3.15c was acquired with 50% flyback inside-out EPI and shows less signal loss than in Fig. 3.15b. This is due to the superior phase-encode-flow properties of inside-out EPI.

Figure 3.16 shows breath-held axial images of the heart of another normal volunteer; also acquired in late diastole. Figure 3.16a was acquired with no-flyback partial-Fourier EPI. In this image, readout flow is responsible for acute signal loss in the heart in the region just inferior to the mitral valve. In Fig. 3.16b, the use of 50% flyback dramatically eliminates this signal loss. Figure 3.16c was acquired with the 50% flyback inside-out sequence and shows even less signal loss than Fig. 3.16b.

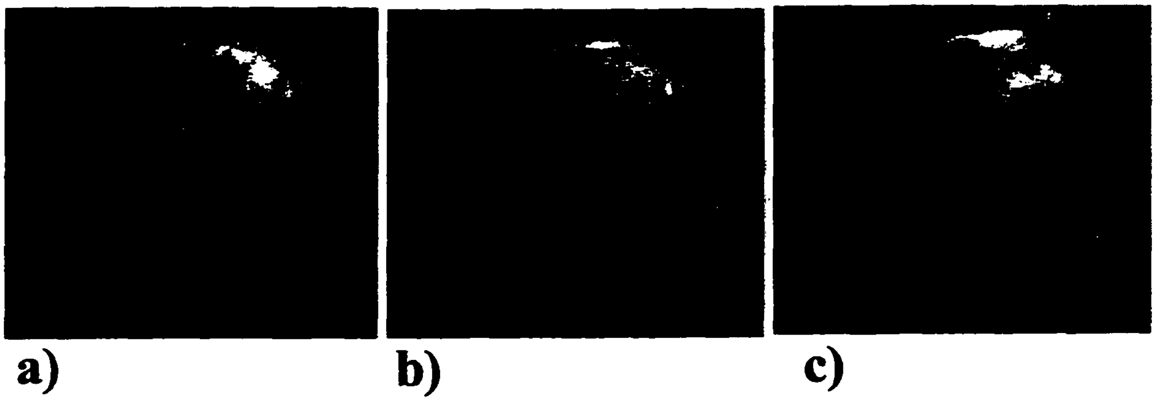

Figure 3.15: Breath-held, axial images of the heart of a normal volunteer. Data acquisition was gated to late diastole. Signal loss is reduced by the use of 50% flyback and inside-out. (a) No-flyback partial-Fourier EPI. (b) 50% flyback partial-Fourier EPI. (c) 50% flyback inside-out EPI. The image parameters are the same as in Fig. 3.14.

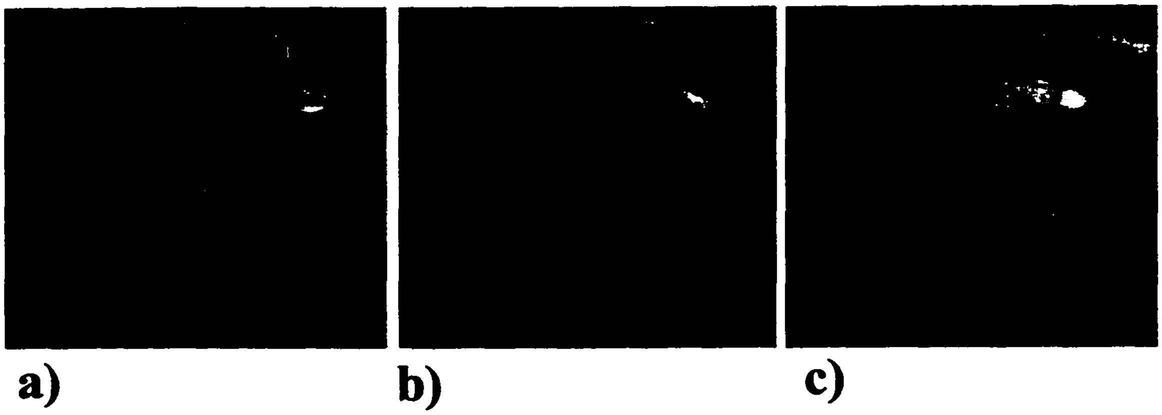

Figure 3.16: Breath-held, axial images of the heart of a normal volunteer. Data acquisition was gated to late diastole. Signal loss is reduced by the use of 50% flyback and inside-out. (a) No-flyback partial-Fourier EPI. (b) 50% flyback partial-Fourier EPI. (c) 50% flyback inside-out EPI. The image parameters are the same as in Fig. 3.14.

3.10 Discussion

3.10.1 Comparing the three sequences

With the number of interleaves constant, Table 3.1 summarizes the differences among the three sequences considered in this chapter.

For no-flyback partial-Fourier EPI, off-resonance produces a benign shift in the phase-encode direction. However, readout flow produces ghosting and signal loss since data is acquired in both the positive and negative k_x-directions. Phase-encode flow mostly produces signal loss since the phase-encoding gradients are active before the center of k-space is acquired.

For partial-flyback partial-Fourier EPI, off-resonance causes some blurring. This is because partial-flyback puts a 'knee' in the off-resonant phase. Readout-flow artifacts are less severe than for no-flyback partial-Fourier EPI since, for the important low spatial frequencies, data is acquired in only one k_x-direction. Phase-encode-flow artifacts are slightly worse than for no-flyback partial-Fourier EPI because the phase-encoding gradients are active for a longer time before the center of *k*-space is acquired.

For partial-flyback inside-out EPI, off-resonance produces blurring or ghosting. Starting data acquisition at the center of *k*-space puts another knee in the off-resonant phase at the center of *k*-space. However, it results in less signal loss from off-resonance since the TE is shorter. The readout-flow properties of partial-flyback inside-out EPI are essentially the same as those of partial-flyback partial-Fourier EPI. Phase encode flow properties are superior to those of no-flyback partial-Fourier EPI and partial-flyback partial-Fourier EPI since there is much less phase-encoding before the center of *k*-space is acquired. Finally, we emphasize that inside-out EPI does not use partial *k*-space acquisition and so is not susceptible to imperfections in data synthesis.

Sequence	Advantages	Disadvantages
No-flyback partial-Fourier EPI	Off-resonance produces a benign shift	Partial-Fourier reconstruction produces artifacts
Partial-flyback partial-Fourier EPI	Partial-flyback reduces readout-flow artifacts	Partial-Fourier reconstruction produces artifacts
Partial-flyback inside-out EPI	Partial-flyback reduces readout-flow artifacts Inside-out reduces phase-encode-flow artifacts	Off-resonance causes ghosting

Table 3.1: Advantages and disadvantages of the three EPI trajectories.

In summary, partial-flyback should be used in situations where there is significant flow in the readout direction. Inside-out EPI should be used in situations where there is significant flow in the phase-encode direction. However, in situations where the artifacts from conjugation reconstruction are tolerable, the superior off-resonance properties of partial-Fourier EPI are recommended.

3.10.2 EPI versus spiral imaging

In general, spiral imaging demonstrates better flow properties than echo-planar imaging [22]. This is because the spiral trajectory never ventures near the edges of *k*-space until it has acquired the central regions. In comparison, EPI collects k_x-edges of *k*-space very soon after the RF excitation.

Therefore, near the center of *k*-space, the gradient moments are smaller for spiral imaging than for EPI. Additionally, for a given field of view and spatial resolution, a spiral trajectory has a shorter data acquisition time. It makes more effective use of the gradient amplifiers since there are no sharp turns in *k*-space.

However, there are three scenarios in which EPI may offer advantages over spiral imaging. First, commercially-available gradient hardware now offers significant increases in slew rate which is more beneficial to EPI than to spiral imaging. Second, for imaging regions with significant B_0 inhomogeneity, the off-resonance artifacts of partial-Fourier EPI are less obtrusive than those of spiral imaging. Third, in the readout direction, it may be desirable to limit the field of view with the anti-aliasing filter. This is possible with EPI but not with spiral imaging.

3.10.3 Higher-performance gradients

Higher-performance gradients than the ones we used in acquiring our images are becoming available, for example, gradients with an amplitude of 40 mT/m and a slew rate of 150 mT/m/ms. These higher-performance gradients would have improved our imaging performance in the following ways.

For a given spatial resolution, the gradient waveform duration could have been shortened, increasing the number of number of images that could be acquired in a breath-hold. For example, for the 50% flyback inside-out parameters given in the caption of Fig. 3.4, the total data-acquisition time for all 16 interleaves could have been reduced from 420 ms to about 150 ms. Alternatively, for a given data-acquisition time, the resolution could have been increased; this is particularly significant for breath-held scans.

Continuing the example of the 50% flyback inside-out parameters given in the caption of Fig. 3.4, for a total data-acquisition time of 420 ms, the resolution could have been increased from about 1.6 mm to about 0.8 mm. Whether the waveform duration was shortened or the resolution was increased, these gradients would have provided greater speed through *k*-space, allowing less evolution of spurious phase produced by off-resonance and flow and therefore reducing the resulting artifacts.

For trajectories that use flyback, the higher-performance gradients may yield positive G_x lobes whose durations are too short to provide adequate SNR. Therefore, we may want to limit the amplitude of the positive G_x lobes, producing a gradient waveform where the negative G_x lobes are taller and thinner than the positive G_x lobes [49]. This would have changed the off-resonance behavior shown by Figs. 3.8b-3.8c: the slope change between the flyback region and the non-flyback region would have decreased, reducing the off-resonance blurring. Furthermore, with sufficient asymmetry between the durations of positive and negative G_x lobes, full flyback may make more sense than partial flyback.

3.11. Conclusions

Partial-flyback EPI allows significantly improved readout-flow properties at the expense of slightly worsened phase-encode-flow properties or increased imaging time, along with slightly worsened off-resonance properties. We recommend that the flyback region acquire 95% of the energy in *k*-space.

Partial-flyback was shown to improve partial-Fourier EPI and inside-out EPI. Indeed, it can be applied to any EPI trajectory. Inside-out EPI was shown to be a viable alternative to partial-Fourier EPI. Although it has worse off-resonance properties than partial-Fourier EPI, it demonstrates better flow properties. Furthermore, it does not suffer from the artifacts of partial *k*-space reconstruction.

Chapter 4

One-Shot Spatially-Resolved Velocity Imaging

4.1 Introduction

Quantitative velocity MRI can provide valuable information in many situations [50]. In cases of severe aortic stenosis, flow velocities approaching 6 m/s have been measured [51]. In evaluating left ventricular diastolic function and mitral valve disease, flow through the mitral valve and in the pulmonary vein are important [52, 53]. In normal peripheral vessels, flow is triphasic or biphasic whereas, in diseased peripheral vessels, flow can be monophasic with reduced maximum velocity [21, 54].

In MRI, quantitative velocity measurement can be achieved with Fourier-encoded velocity imaging (FEVI) which uses "velocity phase-encoding" in addition to encoding in two spatial dimensions [55, 56]. However, since it acquires a three-dimensional data set, acquisition times are long. Acquisition times can be reduced by using a cylindrical excitation [19] to restrict imaging to one spatial dimension [57, 58]. However, cardiac gating is still necessary.

Acquisition times can be further reduced by using phase-contrast imaging [59-61] with a cylindrical excitation [58, 62], eliminating the need for cardiac gating. However, since phase-contrast imaging produces only a single velocity value for each spatial location, velocity measurements are inaccurate when several velocities are present in one voxel.

Full velocity spectra without cardiac gating can be obtained with a technique which we call "bowtie imaging" because of the shape of the *k*-space trajectory. It employs a cylindrical excitation followed by data acquisition during a time-variant gradient [63, 64]. The time-variant gradient combines the full *k*-space coverage of FEVI with the short acquisition times of phase-contrast imaging. After each excitation, an image of velocity versus spatial location is obtained. For a given spatial location, a series of these images can be used to form an image of velocity versus time. We note that bowtie imaging can be viewed as an MRI equivalent of Doppler ultrasound imaging.

For bowtie imaging, the two-shot version of Irarrazabal *et al.* [64] is sensitive to off-resonance. This chapter presents a one-shot version of bowtie imaging which achieves better off-resonance properties and obtains higher temporal resolution for a given velocity resolution. In Section 4.2, the *k*-space trajectory of this technique is described. Section 4.3 presents our implementation of this technique and Section 4.4 presents phantom and *in-vivo* results. The discussion in Section 4.5 includes a comparison of bowtie imaging with other velocity-imaging techniques.

4.2 Theory

4.2.1 Velocity *k*-space trajectory

Bowtie imaging exists in a *k*-space which has one spatial dimension and one velocity dimension, as described in Section 2.4. For a constant velocity, v, in the x direction, the MRI signal equation for bowtie imaging is:

$$s(t)=\iint m(x,v)_{t=0}\ e^{-i2\pi[k_x(t)x+k_v(t)v]}\ dx\ dv. \tag{4.1}$$

where the magnetization, m, is a function of x and v as defined at a time, $t=0$, and

$$k_x(t)=\frac{\gamma}{2\pi}\int_{t_o}^{t} G_x(\tau)\ d\tau \tag{4.2}$$

$$k_v(t)=\frac{\gamma}{2\pi}\int_{t_o}^{t} \tau\ G_x(\tau)\ d\tau \tag{4.3}$$

where $G_x(t)$ is a time-variant gradient and t_o is the time when this gradient is turned on. In general, the gradient waveform is turned on before the instant at which we define m so that $t_o \leq 0$.

Using Eqs. 4.2-4.3, we can plot the trajectory in k_x-k_v space for a given gradient waveform. Figure 4.1 shows an oscillating G_x waveform, its zeroth moment, k_x, and its first moment, k_v, and a plot of k_v versus k_x. The k_x-k_v trajectory starts at the origin then traces the sequence of points from 't1' to 't6,' corresponding to the time labels on the plots of G_x, k_x and k_v. The trajectory oscillates about the *k*-space origin with the k_x amplitude remaining constant and the k_v amplitude increasing with time.

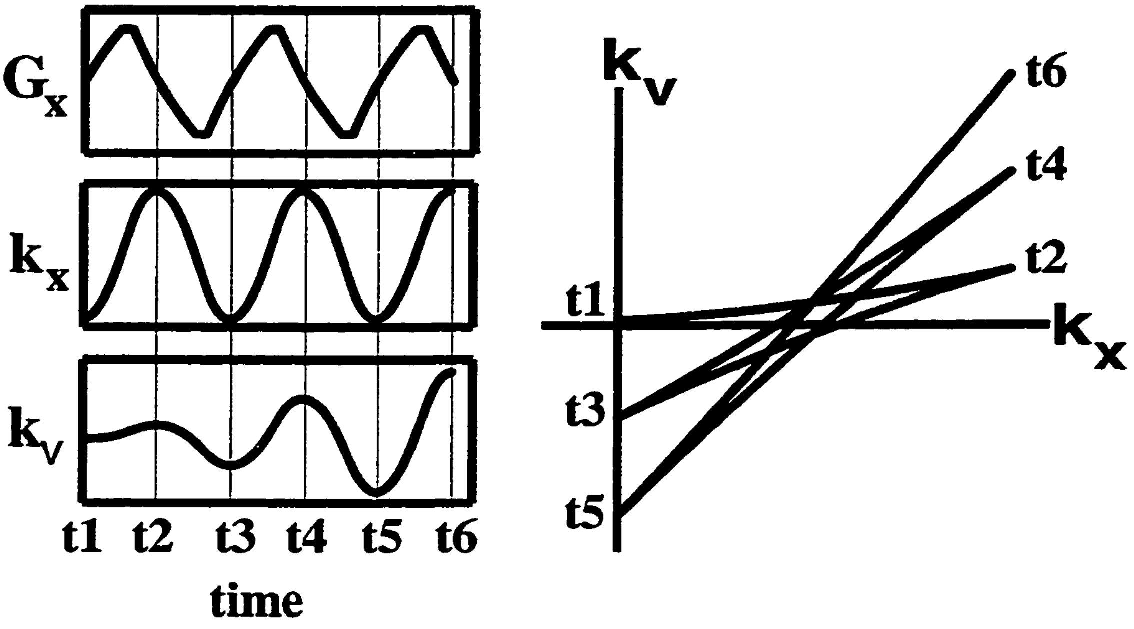

Figure 4.1: Time-variant gradient, G_x, zeroth moment, k_x, and first moment, k_v. The k_x-k_v trajectory starts at the k-space origin and traces the sequence of points from 't1' to 't6'. These points correspond to time instants on the plots of G_x, k_x and k_v.

The bowtie shape of the trajectory can be explained by the following observation. At any given time, the slope of the trajectory is 't' as given by Irarrazabal *et al.* [64]:

$$\frac{dk_v}{dk_x} = t. \tag{4.4}$$

This can be derived by differentiating Eqs. 4.2 and 4.3 then dividing. If we choose to define t1 as t = 0 then the first oscillation of G_x produces a 'spoke' whose initial slope is 0. Since time increases with each successive oscillation, the slope of each spoke increases. Near-vertical spokes will only appear as time approaches infinity and are therefore not achievable in practice.

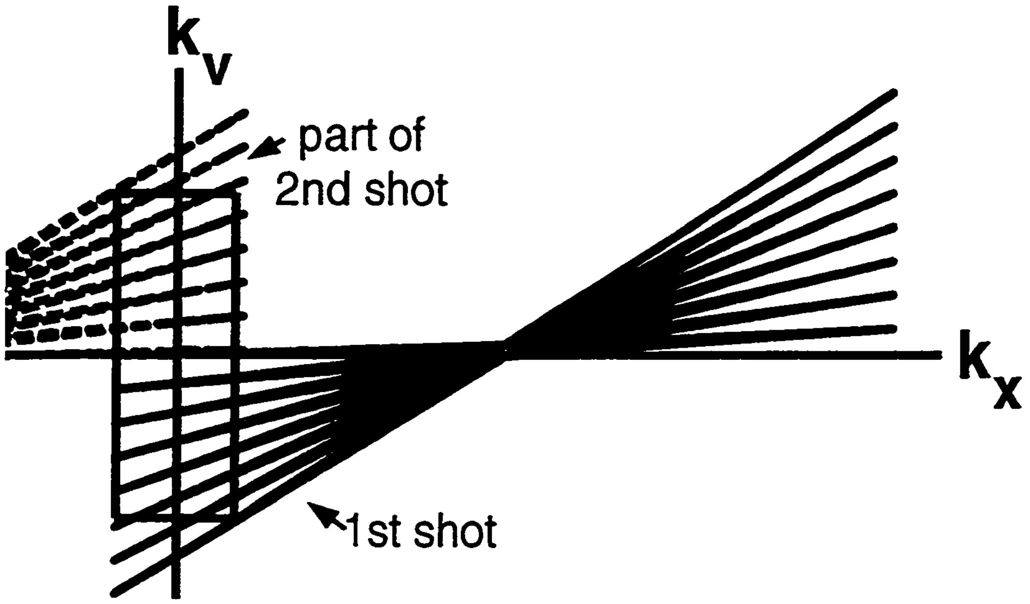

Figure 4.2: Two-shot imaging k_x-k_v trajectory corresponding to the G_x waveform in Fig. 4.6. The first shot acquires the bottom-half of *k*-space while the second shot acquires the top-half. Image reconstruction uses data from the rectangular region shown.

The bowtie shown only occupies two quadrants of *k*-space. The other two quadrants could have been filled with data acquired during 'negative time'. For example, if we had chosen t4 = 0 then the spokes joining t1 to t2, t2 to t3 and t3 to t4 would have negative slopes. This concept of negative time could be used to make a bowtie that is symmetric about k_v=0. However, for the one-shot imaging that we propose, this concept is not needed.

4.2.2 Two-shot imaging

Irarrazabal *et al.* [64] used two-shot imaging in which two excitations achieved full *k*-space coverage. The 1st excitation acquires, for example, the bottom half of *k*-space and the 2nd excitation, with the polarity of the readout gradient reversed, acquires the top half of *k*-space. Figure 4.2 shows the

k-space trajectory and the rectangular region from which data are taken for image reconstruction. The first excitation's trajectory is drawn in a solid line while the second excitation's is drawn in a dashed line. This trajectory corresponds to the G_x waveform in Fig. 4.6. This waveform is similar to that in Fig. 4.1 except that it is preceded by a small prewinder lobe. This prewinder shifts the bowtie along k_x so that the rectangle is centered on the k-space origin.

With this technique, a velocity image requires data from two excitations. By using the two most recent excitations, a velocity image can be produced after *every* excitation. Whiles this doubles the display rate, it does not double the temporal resolution. For improved temporal resolution and better off-resonance properties, we propose one-shot imaging.

4.2.3 One-shot imaging

In one-shot imaging, each excitation uses partial k-space coverage where only part of the k_v information is acquired. Figure 4.3 shows the k-space trajectory and the rectangular region corresponding to the G_x waveform in Fig. 4.7. The unipolar prewinder of Fig. 4.6 is replaced by a bipolar prewinder, whose net area is non-zero, which shifts the bowtie along both k_x and k_v. This k_v-shift allows 63% of the desired rectangle to be acquired.

Compared to two-shot imaging, one-shot imaging requires partial-Fourier reconstruction, such as described in Appendix B. However, one-shot imaging also has important advantages over two-shot imaging. First, it has superior off-resonance properties. Second, because it synthesizes part of the k-

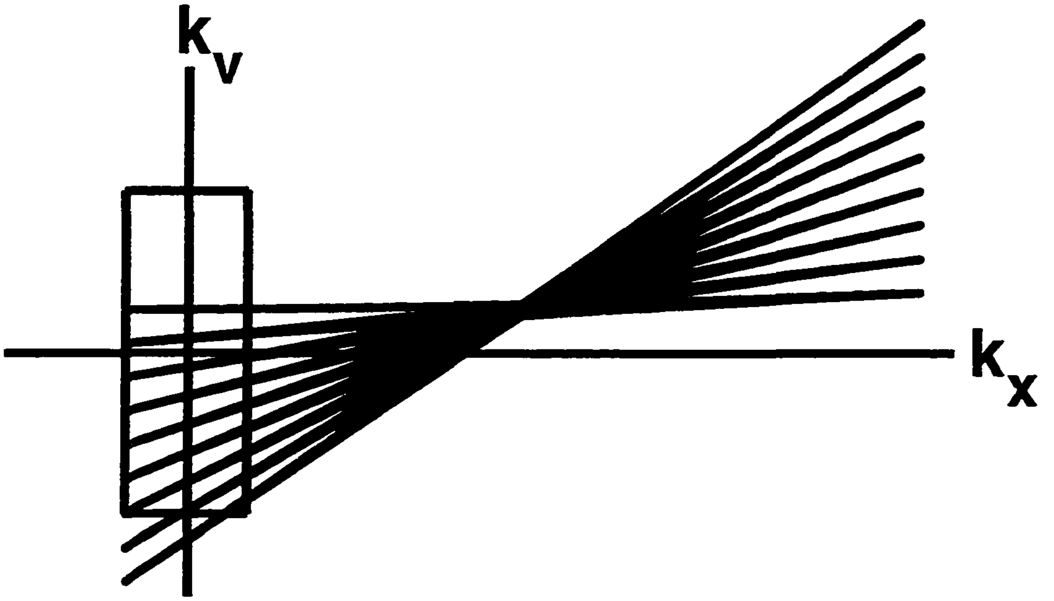

Figure 4.3: One-shot imaging k_x-k_v trajectory corresponding to the G_x waveform in Fig. 4.7. It acquires only part of the desired rectangular region. The unacquired data are synthesized using partial-Fourier reconstruction.

space data, it achieves higher temporal resolution for a given velocity resolution. These disadvantages and advantages will be discussed later.

4.2.4 Resolution and field-of-view

Image reconstruction uses data from a rectangular region of k-space. Since the data are not acquired on a Cartesian grid, gridding [45] is used to reconstruct the image. The spatial resolution is determined by the width of the rectangular region in the k_x direction. Similarly, the velocity resolution is determined by the width of the rectangle in the k_v direction. The velocity field-of-view is given by the largest k_v-spacing between the spokes. This typically occurs at the k_x-edge of the bowtie. The spatial field-of-view is given by the largest k_x-spacing between samples. This occurs when the gradient

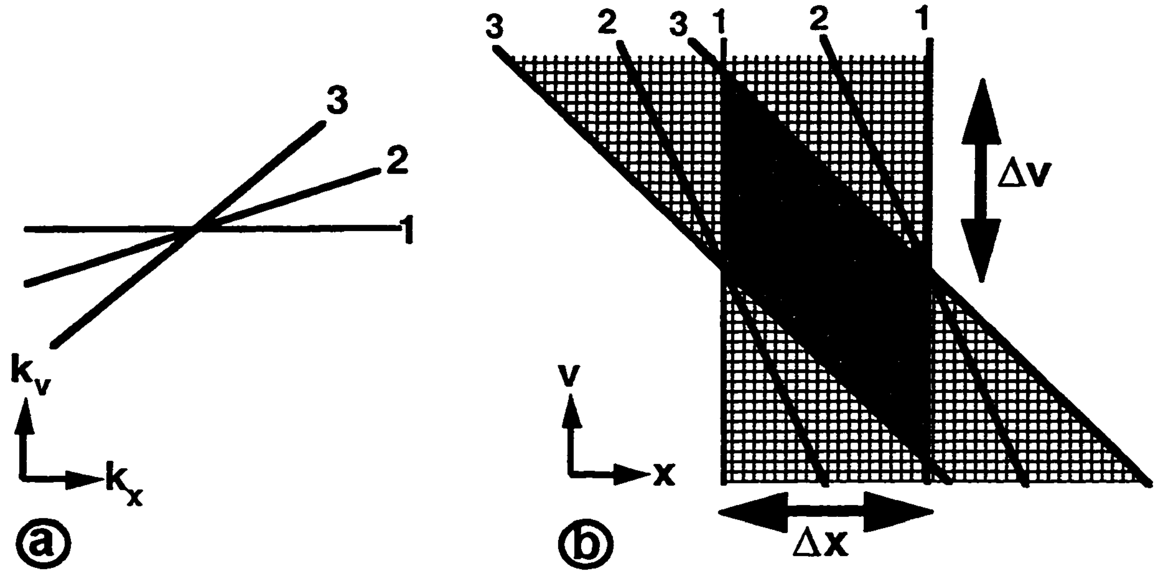

Figure 4.4: Anti-aliasing filter effects on the bowtie-imaging FOV. (a) k_x-k_v space: simplified trajectory with three spokes labelled '1' to '3'. (b) x-v space: filter limits the FOV of each spoke in the direction of that spoke. The darker shaded area is the intersection of the FOVs of all the spokes. The lighter shaded area plus darker shaded area is the union of the FOVs of all the spokes. Only the intersection of the FOVs contains useful signal.

amplitude is largest. We refer to the field-of-view defined by the *k*-space sampling density as the 'sampling-density FOV.'

Besides the maximum spacing between *k*-space samples, the field-of-view can also be limited by the anti-aliasing filter. These filter effects are analyzed in detail in Appendix D and the results are merely stated here. For each spoke, applying the anti-aliasing filter limits the field-of-view in the direction of that spoke, as shown in Fig. 4.4. The intersection of the fields-of-view of all the spokes in Fig. 4.4a is the darker shaded area in Fig. 4.4b and is referred to as the 'intersection FOV.' Only signal in this intersection FOV comes from a complete set of *k*-space data. The union of the fields-of-view of all the spokes in Fig. 4.4a consists of the lighter and the darker shaded areas in Fig. 4.4b and is referred to as the 'union FOV.' Signal in the lighter shaded area (inside the union FOV but outside the intersection FOV) represents spins which were within the filter bandwidth for only some of the spokes. Therefore, this signal comes from an incomplete set of *k*-space data and is not useful. If Δx and Δv are the dimensions of the intersection FOV as labelled in Fig. 4.4b, we can write $\Delta x = FOV_x$ and $\Delta v = FOV_x/t_{DAQ}$ where FOV_x is determined by the filter bandwidth and t_{DAQ} is the length of the data-acquisition period.

Therefore, the field-of-view can be limited by the *k*-space sampling density or by the anti-aliasing filter. If the object being imaged is smaller than the intersection FOV then the anti-aliasing filter is irrelevant and the field-of-view is limited by the *k*-space sampling density. However, if the object being imaged is larger than the intersection FOV then the field-of-view is limited to the intersection FOV. In this case, we note that (a) the *k*-space sampling density should be large enough to prevent aliasing in the intersection FOV and (b) the velocity field-of-view varies with *x*-location and is diminished if t_{DAQ} is lengthened.

4.2.5 Off-resonance

In previous chapters, we analyzed the effects of off-resonance by adding a resonant-frequency dimension to *k*-space. While this works well for stationary spins, we need to be more careful when considering moving spins. For a spin moving through a region of space where the off-resonance is spatially-variant, the resonant frequency of that spin varies with time. For a spin moving with constant velocity, v, the phase induced by the spatially-variant off-resonance, $f(x)$, can be expressed as $2\pi\phi(x,v,f,t)$ where

$$\phi(x,v,f,t) = (t-t_s)f(x) + \frac{v(t^2-t_s^2)}{2!}\frac{df}{dx} + \frac{v^2(t^3-t_s^3)}{3!}\frac{d^2f}{dx^2} + \ldots \qquad (4.5)$$

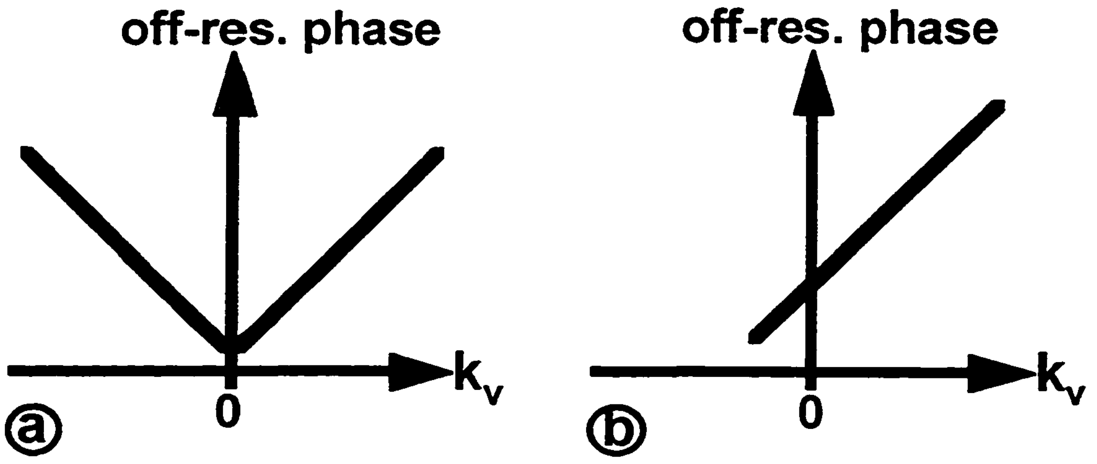

Figure 4.5: Off-resonant phase vs. k_v when k_x=0 and the off-resonant frequency is spatially invariant. (a) For two-shot imaging, the v-shaped profile results in blurring or ghosting along the v-direction of the image. (b) For one-shot imaging, the linear profile results in shifting along the v-direction of the image.

and t_s is the effective center of the excitation pulse. This equation is derived in Appendix E. The MR signal equation then becomes

$$s(t) = \iiint m(x,v,f)_{t=0}\, e^{-i2\pi[k_x(t)x+k_v(t)v+\phi(x,v,f,t)]}\, dx\, dv\, df \qquad (4.6)$$

Since we cannot write the $2\pi\phi(x,v,f,t)$ term in the form of $2\pi k_f(t)f$, our previous addition of a single resonant-frequency dimension to k-space is inadequate to analyze the effects of off-resonance on moving spins. Perhaps it is possible to use multiple resonant-frequency dimensions in k-space such that the k-space variables are $\{t, t^2, t^3, \ldots\}$ and the image-space variables are $\{f, df/dt, d^2f/dt^2, \ldots\}$ but this is a subject for future work.

For the present, we can gain some understanding of the effects of off-resonance in bowtie imaging by considering a situation in which f is constant. In such case, Eq. 4.5 reduces to the familiar form:

$$\phi(t) = (t - t_s)f. \qquad (4.7)$$

If we further assume that $fT << 1$, where T is the duration of one readout lobe, we can neglect the off-resonant-phase evolution along k_x and consider only its evolution along k_v. Under these conditions, Fig. 4.5 sketches the off-resonant phase against k_v for $k_x=0$. For two-shot imaging, Fig. 4.5a shows a 'v' shaped plot because one of the shots travels from the k-space origin to $+k_v$ while the other shot travels from the k-space origin to $-k_v$. Consequently, there is blurring along the v direction as shown in Fig. 4.11b. For one-shot imaging, Fig. 4.5b shows a linear plot since travel is only in one k_v-direction. Consequently, there is shifting along the v direction as shown in Fig. 4.11c. In general, the $fT << 1$ condition is usually satisfied. However, f is not usually constant. Therefore, in addition to the first-order effects discussed above, there can be smearing of the signal in the v direction.

It is possible to reduce off-resonance artifacts using a field map and the time-segmented deblurring of Noll *et al.* [42]. However, it is difficult to obtain a field map of flowing material. We estimated a field map from the phase difference of two x-v images with different TEs. However, manipulation of Eq. 4.5 shows that such a map is corrupted by velocity effects. Using only the $v=0$ signal can avoid these velocity effects but this strategy has two problems. First, the resonant frequency of the static material may not be that of the flowing material. Second, if a particular x-location contains static material with a range of off-resonant frequencies, the field map may be invalid at that x-location.

Section 4.4 shows some images with off-resonance correction. However, we found that such correction could be futile for two-shot imaging and was not necessary for one-shot imaging.

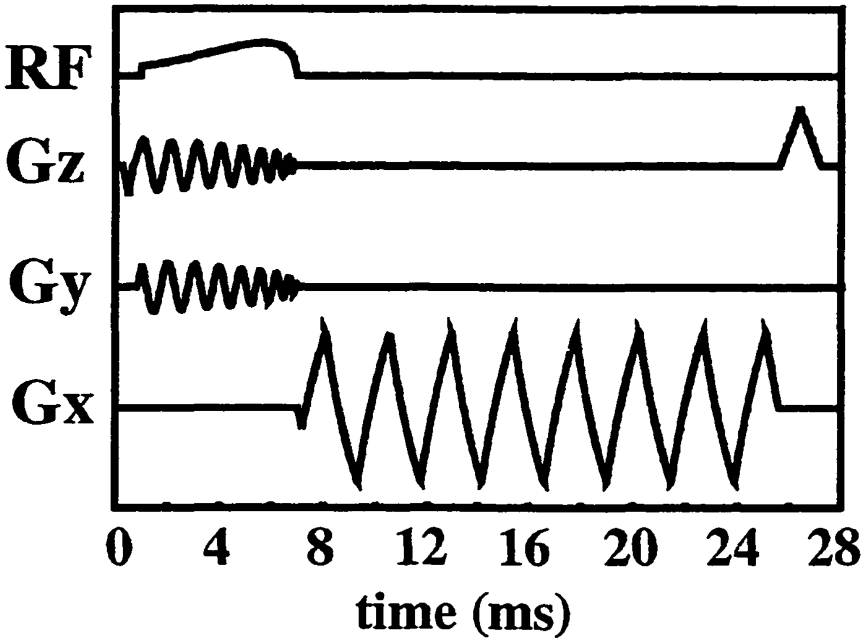

Figure 4.6: Pulse sequence diagram for two-shot imaging showing cylindrical excitation and oscillating readout gradient, G_x. The polarity of the readout gradient is alternated for each excitation.

4.3 Method

We implemented the one-shot and two-shot velocity imaging sequences on a GE Signa 1.5 T system. The gradient subsystem has a maximum amplitude of 22 mT/m and a slew rate of 20 mT/m/ms. The maximum sampling rate for data acquisition is 125 kHz.

Figures 4.6 and 4.7 show the pulse sequence diagrams for two-shot and one-shot velocity imaging, respectively. The RF, G_y and G_z axes depict the cylindrical RF excitation. In Fig. 4.6, the imaging waveform on the G_x axis begins with a unipolar prewinder used to appropriately center the k-space rectangle. In Fig. 4.7, a bipolar prewinder is used. For both imaging techniques, the G_z crusher was essential in providing a steady signal level from excitation to excitation. RF-phase spoiling was not required.

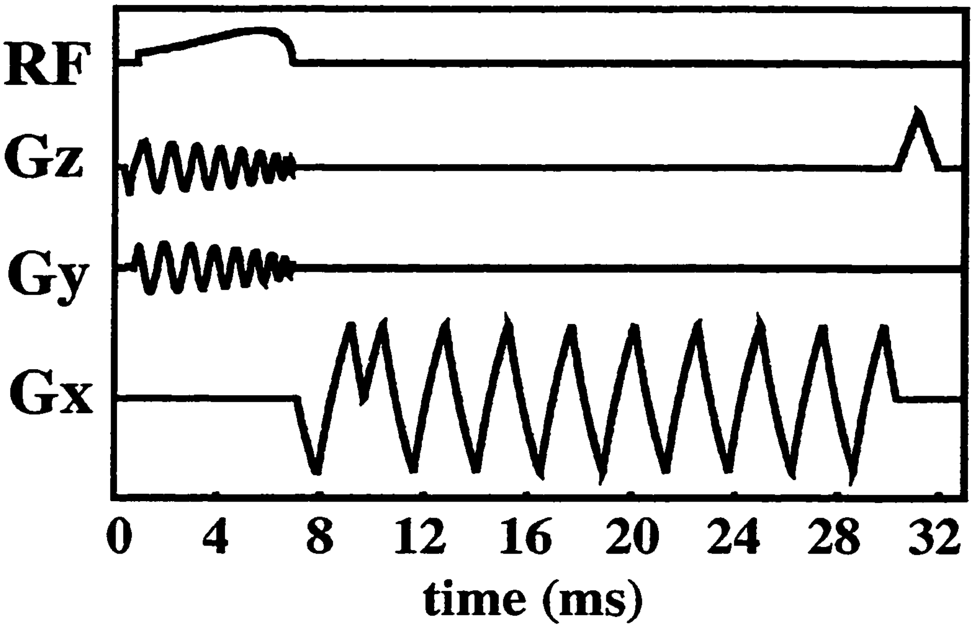

Figure 4.7: Pulse sequence diagram for one-shot imaging showing cylindrical excitation and oscillating readout gradient, G_x. In contrast to two-shot imaging, the prewinder before the oscillating readout gradient is bipolar.

For all of the one-shot images shown, the image-reconstruction method is described in Appendix B. This method assumes a real-valued object in x-v space and attempts to correct for off-resonance- and motion-induced phase which can compromise this assumption. We note that this same algorithm, when used to reconstruct partial-Fourier EPI, produces artifacts since the velocity-induced phase in EPI is usually severe. We did not encounter such artifacts with one-shot bowtie imaging because the acceleration-induced phase was not severe.

4.3.1 Readout-gradient waveform

The design of the readout-gradient waveform involves tradeoffs among spatial resolution and field-of-view, velocity resolution and field-of-view, and temporal resolution. We used exponential ramps [44] and sampling on the G_x ramps to achieve greater resolution and field-of-view than with linear ramps and sampling only on the G_x plateaus. With exponential ramps, we achieved an average slew rate of 29 mT/m/ms which is about 50% greater than with linear ramps. We want to emphasize that bowtie imaging will work with any unipolar shape for the G_x lobes.

We designed gradient waveforms for imaging a flow phantom and the aorta. Readout-waveform parameters and performance measures are listed in Table 4.1 for flow-phantom imaging and in Table 4.2 for aorta imaging. The ∂x and ∂v performance measures are simply the inverse of the $k_{x,rect}$ and $k_{v,rect}$ parameters respectively but are listed for convenience. The t_{DAQ} performance measure gives a lower limit on the temporal resolution. The intersection FOV_x is the x-width of the intersection FOV at v=0 calculated using the largest G_x amplitude. The intersection FOV_v is the v-width of the intersection FOV at x=0 again calculated using the largest G_x amplitude.

We now consider the effects of the anti-aliasing filter. In the v direction, we don't expect any signal outside the sampling-density FOV_v. Therefore, the object being imaged is smaller than the intersection FOV_v and the anti-aliasing filter is irrelevant. In the x direction, however, the object being imaged is larger than the intersection FOV_x and we need to ensure that the sampling-density FOV_x is large enough to prevent aliasing into the intersection FOV. The extreme x values of the union FOV can be calculated by noting that we don't expect any signal outside the sampling-density FOV_v. Therefore, the extreme x values of the union FOV are at v=±(sampling-density FOV_v)/2 and, with reference to Fig. 4.4b, are given by

$$\text{union } FOV_x = (\text{intersection } FOV_x) + 2\, t_{DAQ}\, (\text{sampling-density } FOV_v)/2. \quad (4.8)$$

In all four cases in Tables 4.1-4.2, the union FOV_x is smaller than the sampling-density FOV_x so there will be no aliasing into the intersection FOV.

For flow phantom imaging, between one-shot and two-shot imaging, we kept the same data acquisition time per excitation, velocity field-of-view, spatial field-of-view and spatial resolution. Under these conditions, one-shot imaging has twice the temporal resolution as two-shot imaging but slightly worse velocity resolution. The velocity resolution would be the same if one-shot imaging only acquired 50% of k-space. However, slightly more than 50% of k-space has to be acquired otherwise the partial-Fourier reconstruction would not work well.

Imaging the aorta requires a velocity field-of-view of about 180 cm/s in normal subjects. It also requires high temporal resolution since systolic flow produces an abrupt peak in the velocity-time profile. Between one-shot and two-shot imaging, we kept the same spatial field-of-view, velocity field-of-view, spatial resolution and velocity resolution. Under these conditions, one-shot imaging achieves better temporal resolution than two-shot imaging.

The sampling-density velocity field-of-view, FOV_v, was reduced by allowing aliasing in the velocity direction. This works well in the case of aorta imaging since the maximum antegrade velocity is much larger than the maximum retrograde velocity. This aliasing was unwrapped by gridding to a larger FOV_v. Unwrapping should not use a circular shift in the velocity direction because the variable k_v-spacing between the spokes of the trajectory yields a sampling-density FOV_v that varies with k_x.

Parameter	Description	Two-shot imaging value	One-shot imaging value
N_{lobes}	no. lobes in sawtooth portion of waveform	25	25
$k_{x,lobe}$	area of each lobe in sawtooth (1/cm)	3.6	3.6
$k_{x,rect}$	k_x-width of rectangular k-space region (1/cm)	0.67	0.67
$k_{v,rect}$	k_v-width of rectangular k-space region (s/cm)	0.065	0.053
sampling-density FOV_x	sampling-density spatial field-of-view (cm)	32	32
intersection FOV_x	intersection spatial field-of-view (cm)	17	17

Performance measure	Description	Two-shot imaging value	One-shot imaging value
∂v	velocity resolution (cm/s)	15.4	18.7
∂x	spatial resolution (cm)	1.52	1.52
t_{DAQ}	duration of data-acq. window (ms)	27.2	27.2
sampling-density FOV_v	sampling-density velocity field-of-view (cm/s)	255	255
intersection FOV_v	intersection velocity field-of-view (cm/s)	618	618
∂t	time resolution (ms)	100	50
k_v fraction	fraction of k-space acquired	100%	58%

Table 4.1: Parameters and performance measures of the readout gradient waveforms used for imaging a flow phantom.

Parameter	Description	Two-shot imaging value	One-shot imaging value
N_{lobes}	no. lobes in sawtooth portion of waveform	15	17
$k_{x,lobe}$	area of each lobe in sawtooth (1/cm)	2.25	2.25
$k_{x,rect}$	k_x-width of rectangular k-space region (1/cm)	0.68	0.68
$k_{v,rect}$	k_v-width of rectangular k-space region (s/cm)	0.052	0.052
sampling-density FOV_x	sampling-density spatial field-of-view (cm)	33	33
intersection FOV_x	intersection spatial field-of-view (cm)	19	19

Performance measure	Description	Two-shot imaging value	One-shot imaging value
∂v	velocity resolution (cm/s)	19.2	19.2
∂x	spatial resolution (cm)	1.47	1.47
t_{DAQ}	duration of data-acq. window (ms)	18.2	20.7
sampling-density FOV_v	sampling-density velocity field-of-view (cm/s)	182	182
intersection FOV_v	intersection velocity field-of-view (cm/s)	1050	928
∂t	time resolution (ms)	56	33
k_v fraction	fraction of k-space acquired	100%	63%

Table 4.2: Parameters and performance measures of the readout gradient waveforms used for imaging the aorta.

4.3.2 Cylindrical excitation

In designing the cylindrical excitation, the most important goal is to maximize the signal from the vessel lumen while minimizing unwanted signal. Figure 4.8 shows the profile of the cylindrical excitation we used. Unwanted signal arises from two sources: (i) portions of the cylinder that are outside the vessel lumen and (ii) the sidelobes of the cylindrical excitation. Ideally, we want a cylinder diameter equal to the that of the vessel lumen and sidelobes that occur outside the body or the range of the receiver coil. However, because of the limitations of the gradient subsystem, there are tradeoffs among pulse duration, cylinder diameter and sidelobe proximity [19]. A shorter pulse reduces sensitivity to off-resonance and increases temporal resolution. However, it also means a larger diameter or closer sidelobes. For a given pulse duration, a smaller diameter requires larger spacing between the spiral turns which produces closer sidelobes.

We used a Gaussian-shaped cylinder whose diameter can be characterized by its full width at half-maximum (FWHM). For imaging the aorta, we used a FWHM of 2.0 cm which was reasonably close to the lumen diameters we encountered. To avoid placing the sidelobes in the cardiac chambers, we used a sidelobe distance of 16 cm. The resulting pulse duration was only 6.6 ms. Because of inflow effects, the optimal flip angle depends on several factors, two of which are velocity and how much upstream flow is excited by the cylinder. We empirically chose a flip angle of 30 degrees.

Even if unwanted signal is unavoidable, it can usually be distinguished from the desired velocity signal. Since the sidelobes can usually be placed to avoid flowing material, unwanted signal is typically from static tissue. Therefore, in the *v-t* images, it shows no time-variance and can be

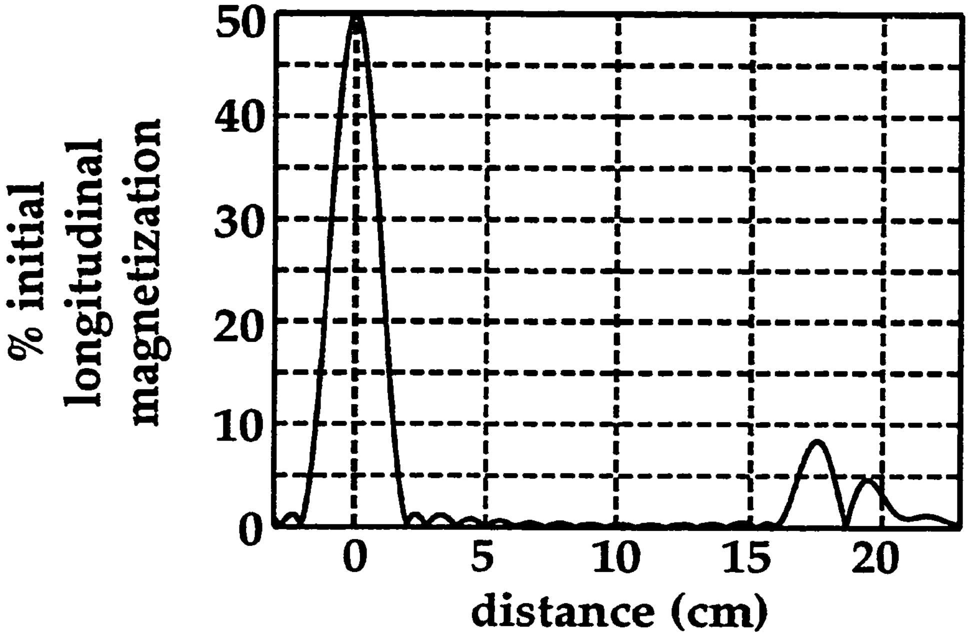

Figure 4.8: Excitation profile of cylindrical pulse used for imaging the aorta. Flip angle is 30 degrees. Full-width at half-maximum is 2.0 cm. First sidelobe ring begins at about 16 cm from the center. Pulse duration is 6.6 ms.

distinguished from the time-variant velocity signal. We note that static signal is not necessarily confined to v=0 since it can be off-resonant.

Nevertheless, we want to emphasize the importance of the cylindrical pulse design in suppressing unwanted signal. A badly designed cylindrical pulse can make the unwanted-signal amplitude much larger than the flow-signal amplitude, obscuring the flow signal.

4.3.3 Positive-negative lobe ghosting

In both one-shot and two-shot imaging, differences between the positive and negative gradient lobes can cause ghosting, as in echo-planar imaging [48]. These differences arise from infidelity in the gradient subsystem and asymmetry in the data acquisition filters and are described in Appendix A. To avoid this ghosting, we used only the positive-lobe data.

The resulting decrease in the velocity field-of-view is negligible since the negative-lobe trajectory is almost identical to the positive-lobe trajectory. The resulting decrease in SNR is tolerable since we can achieve adequate SNR with only the positive-lobe data.

Even when only the positive-lobe data are used, two-shot imaging presents a further complication. Because the polarity of the gradient waveform is reversed between the two shots, gradient subsystem infidelity produces differences in the prewinder lobe, as described in Appendix A. As a result, between the top and bottom halves of *k*-space, there is a difference in the phase and k_x location of the gradient echoes. In echo-planar imaging, these differences are corrected using calibration data that is acquired with the phase-encoding turned off [48]. In velocity imaging, we can "turn off the velocity phase-encoding" by imaging an object that has no flow. Our use of this calibration data is described in detail in Appendix A.

4.4 Results

Images of phantoms and the aortas of normal volunteers were obtained with the head coil and body coil respectively. The images were interpolated in two dimensions by zero-filling in *k*-space. We note that the bowtie technique has been validated by Hu *et al.* [63] who compared their velocity measurements with those from a calibrated flow pump.

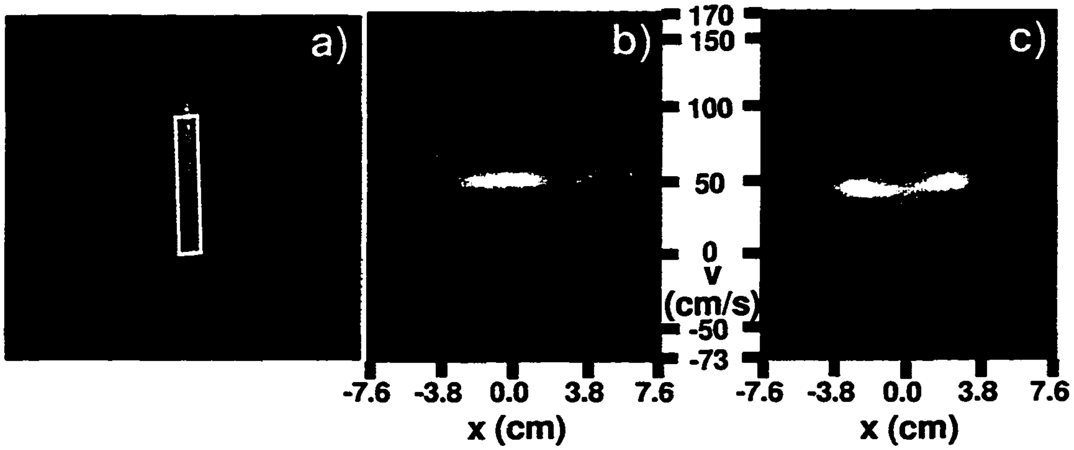

Figure 4.9: Images of pulsatile flow in a tube. (a) Coronal image with the white rectangle showing the placement of the cylindrical excitation. (b) Two-shot image of velocity vs. position. (c) One-shot image of velocity vs. position.

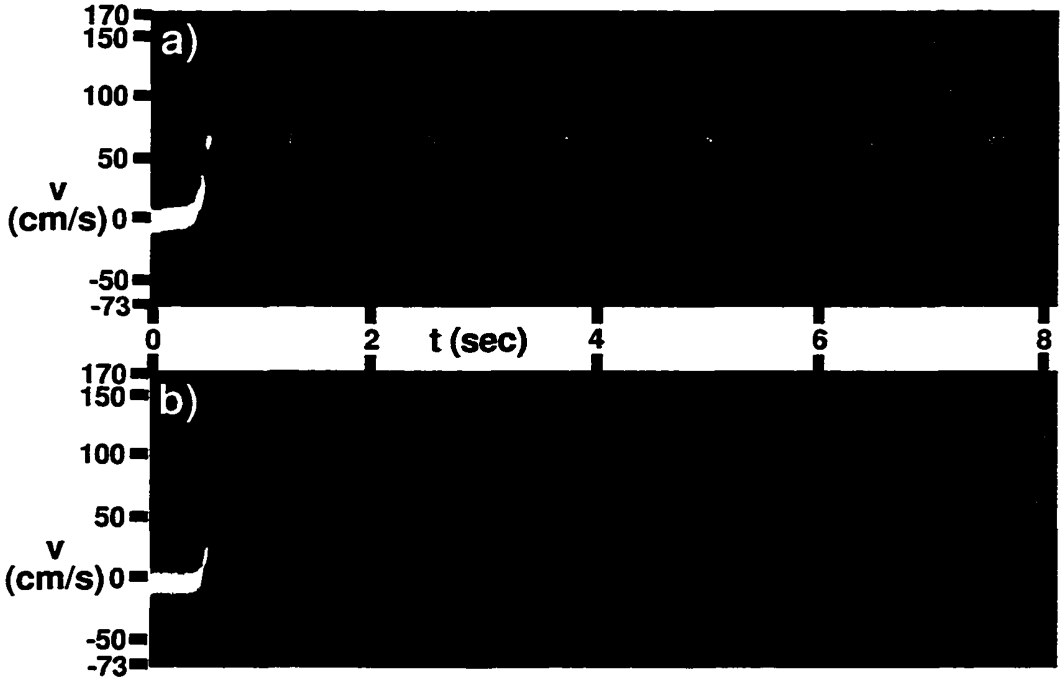

Figure 4.10: Velocity-time images at the spatial centers of the images in Figs. 4.9b and 4.9c. They show the pulsatile-flow pump initially off, being turned on and then settling into periodic behavior. (a) Two-shot image with 100 ms temporal resolution. (b) One-shot image with 50 ms temporal resolution.

Figure 4.9a is a coronal image of water flowing in a tube, as driven by a pulsatile pump. The white rectangle indicates the placement of the cylindrical excitation. Figures 4.9b and 4.9c show *x*-*v* images obtained with two-shot and one-shot imaging, respectively. The expected parabolic-flow profile would be discernible with better velocity resolution. The two-shot image shows blurring caused by off-resonance. In the one-shot image, this same off-resonance causes a shift along the *v* direction.

From the series of *x*-*v* images, we compiled *v*-*t* images for $x=0$, as shown in Fig. 4.10a and 4.10b. They show the flow pump initially off, then being turned on and settling into its steady-state pulsatile behavior. Under these ideal conditions of no extraneous static signal and good B_0 homogeneity, the two-shot and one-shot images are not very different. There is ringing or ghosting along the *v* direction because inadequate velocity resolution causes truncation of the *k*-space data.

Figure 4.11a shows a sagittal image of the thorax of a normal volunteer. The white rectangle indicates the placement of the cylindrical excitation on the descending aorta. Figures 4.11b and 4.11c show *x*-*v* images obtained with two-shot and one-shot imaging, respectively. Again, off-resonance has a much greater effect on the two-shot image than on the one-shot image.

From the series of *x*-*v* images, we compiled *v*-*t* images for $x=0$, as shown in Fig. 4.12a and 4.12b. Here, the adverse effects of off-resonance on two-shot imaging are shown. Both images show the periodic behavior of blood flow in the aorta. However, the one-shot image is much better at resolving the peak antegrade flow and showing the slight retrograde flow caused by the distensibility of the aortic wall.

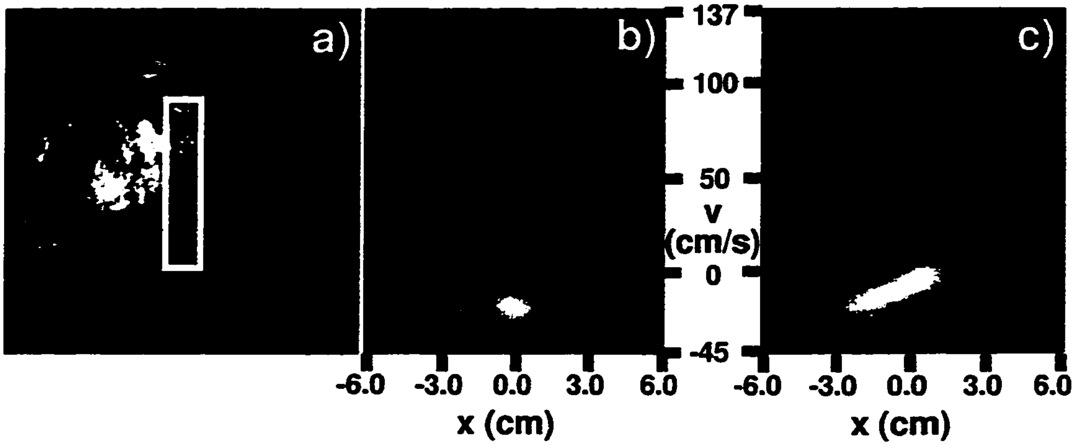

Figure 4.11: Images of the aorta of a normal volunteer. (a) Sagittal image of the thorax with the white rectangle showing the placement of the cylindrical excitation. (b) Two-shot image of velocity vs. position. (c) One-shot image of velocity vs. position.

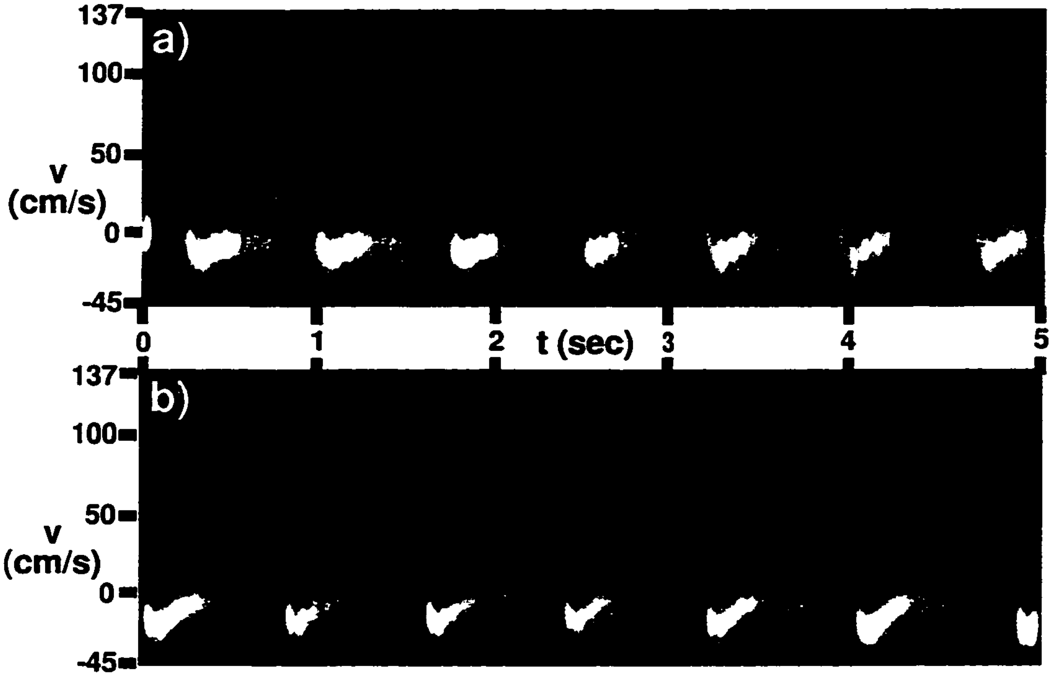

Figure 4.12: Velocity-time images at the spatial centers of the images in Figs. 4.11b and 4.11c. They show the peak flow during systole and retrograde flow during diastole. (a) Two-shot image with 56 ms temporal resolution. (b) One-shot image with 33 ms temporal resolution.

These results demonstrate that good B_0 homogeneity is essential for two-shot imaging. Unfortunately, for *in-vivo* situations, this is difficult to achieve and obtaining a field map for deblurring is also difficult, as described previously. On the other hand, one-shot imaging is much more tolerant of B_0 inhomogeneity, making off-resonance deblurring unnecessary.

4.5 Discussion

4.5.1 Distortion of the cylindrical pulse

The profile of the cylindrical excitation can be distorted by several sources of artifact. T_2-decay effects were minimized by keeping the pulse duration much shorter than the T_2-relaxation times of blood, muscle and fat. B_1-inhomogeneity effects are fairly benign, changing the flip angle but preserving the pulse shape. However, flow and off-resonance can have significant effects.

Flow effects were minimized by orienting the flow along the x direction which is the long axis of the cylinder. Displacement artifacts [65] along x are benign unless the readout field-of-view contains an abrupt change in vessel direction. Flow in the y-z plane is only significant inside the cardiac chambers. The resultant blurring of the profile [66] can be minimized by keeping the pulse duration short. The displacement artifacts can be minimized by keeping the TE short.

Off-resonance can cause blurring of the profile, increasing the amount of unwanted signal from outside the vessel lumen. For example, at 50 Hz off-resonance, the FWHM increases to 2.1 cm and, more significantly, the full-width-at-10%-of-maximum increases from 3.3 cm to 4.8 cm. At 220 Hz off-resonance, the resonant frequency of fat, the FWHM is 9 cm. A good shim can reduce blurring near the water frequency but cannot prevent blurring near the fat frequency. Therefore, excitation of the periadventitial fat seems inevitable, increasing the importance of the B_0 insensitivity of one-shot imaging.

4.5.2 Resolving along the spatial dimension

We found the velocity-time images to be the most useful way to view the bowtie-imaging data. It might therefore be considered unnecessary to resolve along the spatial dimension. However, spatial resolution is useful in distinguishing spatial variance of the velocity-time behavior and of the resonant frequency. When the resonant frequency is spatially variant, signal is presented with different v-shifts for one-shot imaging or different v-blurring for two-shot imaging. This effect can be particularly annoying when it is manifested by static signal with a large amplitude.

4.5.3 Acceleration

Acceleration effects can be analyzed by examining the 2nd moment of the readout-gradient waveform. There are two possible effects: (i) signal loss because the second moment is non-zero and (ii) ghosting because, along k_x=0, the second moment alternates polarity. In Hu et al. [63], the first effect is shown to be negligible when there is no prewinder. Even with prewinders, we did not observe this first effect. Neither did we observe the second effect.

4.5.4 Comparison of one-shot and two-shot imaging

Compared to two-shot imaging, one-shot imaging requires partial-Fourier reconstruction. However, it has important advantages over two-shot imaging. First, off-resonance causes a shift instead of blurring. This means that blurring will not compromise velocity resolution. It also means that off-resonant static signal will not obscure the $v=0$ region. Second, for a given velocity resolution, it has better temporal resolution. Third, it does not require correction for differences between the top and bottom halves of k-space. During the partial-Fourier reconstruction, application of the phase map corrects any differences between the acquired and synthesized data.

4.5.5 Comparison of bowtie imaging with other velocity-imaging techniques

There are some disadvantages to using the cylindrical excitation in bowtie imaging. First, only one spatial dimension is acquired. This makes it impossible to measure flow profiles that are spatially-variant in two dimensions or volumetric flow rates. Second, the minimum cylinder diameter is limited by the gradient subsystem. A cylinder diameter similar to the vessel diameter minimizes the static signal, improving the dynamic range of the flow signal. With current gradient performance, bowtie imaging may be unsuitable for small vessels such as the coronary arteries.

Nevertheless, data acquisition during a time-variant gradient invests bowtie imaging with compelling advantages over other velocity-imaging techniques. First, its short imaging time provides high temporal resolution without the use of cardiac gating. Second, it acquires a full velocity spectrum which, unlike in phase-contrast imaging, can show a range of velocities at each spatial location. Therefore, with sufficient velocity resolution, static signal will not corrupt the velocity measurement.

4.5.6 One-shot imaging with higher-performance gradients

Higher-performance gradients than the ones we used in acquiring our images are becoming available, for example, gradients with an amplitude of 40 mT/m and a slew rate of 150 mT/m/ms. These higher-performance gradients would have improved our imaging performance in three ways. First, since less time would have been required to reach a given point in *k*-space, off-resonance and flow effects would have been reduced since off-resonance- and flow-induced phase would have had less time to evolve. Second, for a given pulse duration, the cylinder diameter could have been reduced or the sidelobe distance increased. Alternatively, for a given cylindrical-excitation profile, the pulse duration could have been shortened, increasing temporal resolution. Third, for a given data-acquisition time, the field-of-view or resolution could have been increased. For example, for the one-shot imaging sequence in Table 4.2, the velocity field-of-view could have been increased from 189 cm/s to 589 cm/s.

4.6 Conclusions

We have presented a velocity imaging technique, which we call one-shot bowtie imaging, that can produce a full velocity spectrum in real time with spatial resolution in one-dimension.

Compared to two-shot bowtie imaging, one-shot bowtie imaging requires partial-Fourier reconstruction. However, it offers superior off-resonance properties, higher temporal resolution for a given velocity resolution, and does not require correction for differences between the top and bottom halves of *k*-space.

Compared to other velocity-imaging techniques, bowtie imaging does not provide images with two spatial dimensions. Furthermore, since the diameter of the cylindrical excitation should be similar to that of the vessel being imaged, it is unsuitable for small vessels such as the coronary arteries. However, unlike Fourier velocity-encoding, it has a short imaging time, and, unlike phase-contrast imaging, it can image a range of velocities at each spatial location. Finally, bowtie imaging requires only one excitation per image, allowing high temporal resolution without cardiac gating.

Chapter 5

High-Resolution Three-Dimensional *In-Vivo* Imaging of Atherosclerotic Plaque

5.1 Introduction

Atherosclerosis is the leading cause of death in the United States and other industrialized nations. In the United States in 1994, cardiovascular diseases claimed over 955,000 lives, or 42% of all deaths [1], of which atherosclerosis is believed to account for a very large fraction.

Clinical assessment of atherosclerosis primarily involves estimates of the degree of stenosis using ultrasound or X-ray angiography. Ultrasound requires suitable acoustic windows and it suffers from speckle noise and considerable operator dependence. X-ray angiography requires ionizing radiation and invasive catheterization. Furthermore, a significant degree of stenosis is not necessarily a good predictor of myocardial infarction or stroke [67, 68]. These acute clinical events occur when atherosclerotic lesions rupture or are eroded, producing thrombus which leads to vessel occlusion.

An alternative assessment of atherosclerosis is to distinguish between vulnerable and stable lesions by examining their internal structure and contents. While X-ray CT can elucidate the surface morphology of a lesion, it cannot provide sufficient contrast to distinguish among the various plaque components [69, 70]. Ultrasound imaging has also been used in attempts to characterize plaque lesions but can be compromised by the echogenicity (acoustic opacity) of calcium which is a common component of plaque [71]. Furthermore, the signal processing required to reliably discriminate plaque components is still the subject of ongoing research [72, 73].

MRI is a promising method for interrogating the internal structure and contents of atherosclerosis. In the early 1980s, it was shown that black-blood MRI demonstrates atherosclerosis as wall thickening, luminal narrowing and discrete lesions [74, 75]. Post-mortem studies which showed increasing lipid content with disease progression [76, 77] motivated lipid imaging of plaque using NMR or chemical-shift MRI [78-84]. However, such lipid imaging has much lower SNR than water imaging because the water signal of plaque is much larger than its lipid signal [79, 82, 85, 86]. It also has poor spectral resolution and low SNR because plaque lipids have T_2s of less than 20 ms [79, 80, 82-84].

As an alternative to chemical-shift imaging, several studies have shown that plaque components such as the vessel wall, cap and lipid, fibrous or calcified core can be distinguished with contrast generated by T_1, T_2 and proton-density weighting [85-93]. In particular, it was shown that T_2-weighted imaging of the water signal can distinguish plaque components [85, 86, 92]. Such morphological imaging achieves better SNR than chemical-shift imaging and can distinguish various types of atherosclerotic lesions. For example, it is believed by some investigators that lesions with large lipid-rich cores and thin caps are unstable, with rupture leading to thrombosis, whereas lesions with thick caps and calcified cores tend to be stable [67].

In-vivo characterization of plaque lesions using T_2-weighted imaging of the water signal presents several challenges. First, high spatial resolution is required since plaque components can have sub-millimeter dimensions. This means that SNR must be carefully managed since it decreases as resolution increases. Second, three spatial dimensions are required because of the typically irregular geometry of the blood vessels and their lesions. Third, excellent off-resonance properties are necessary to avoid compromising the high spatial resolution. Fourth, a long TE is necessary for T_2 contrast. Multi-slice 2D RARE [94] has been found to satisfy most of these requirements [89, 92, 93]. Unfortunately, its resolution in the slice-select direction is limited by the profile of the selective excitation. Therefore, we employed 3D GRASE [95] because it offers better resolution in the slice-select direction, better SNR efficiency, arbitrarily-oriented views and better flow suppression.

Two important aspects of our imaging sequence are flow suppression and cardiac gating. Flow suppression is important in preventing flow artifacts which can severely affect image quality. Cardiac gating is important in avoiding systolic vessel motion which can compromise high spatial resolution. Unfortunately, with high resolution and three spatial dimensions, cardiac gating can make the imaging time very long. Therefore, to obtain imaging times of about 10 minutes, we restricted the FOV in all three dimensions: in the x direction, a lowpass filter was used and, in the y and z directions, a rectangular excitation [96] was used.

This chapter presents high-resolution, three-dimensional *in-vivo* imaging of atherosclerotic plaque using a rectangular excitation pulse to achieve reasonable scan times. Section 5.2 describes the 3D GRASE trajectory, the rectangular excitation used to reduce the imaging time, the flow-suppression technique and our careful management of SNR. Section 5.3 presents *ex-vivo* and *in-vivo* results. The discussion in Section 5.4 includes a comparison of 3D GRASE and 2D RARE.

5.2. Method

We implemented our sequence on a GE Signa 1.5 T system with a maximum gradient amplitude of 22 mT/m, a slew rate of 20 mT/m/ms and a maximum data-acquisition sampling rate of 125 kHz. The pulse sequence

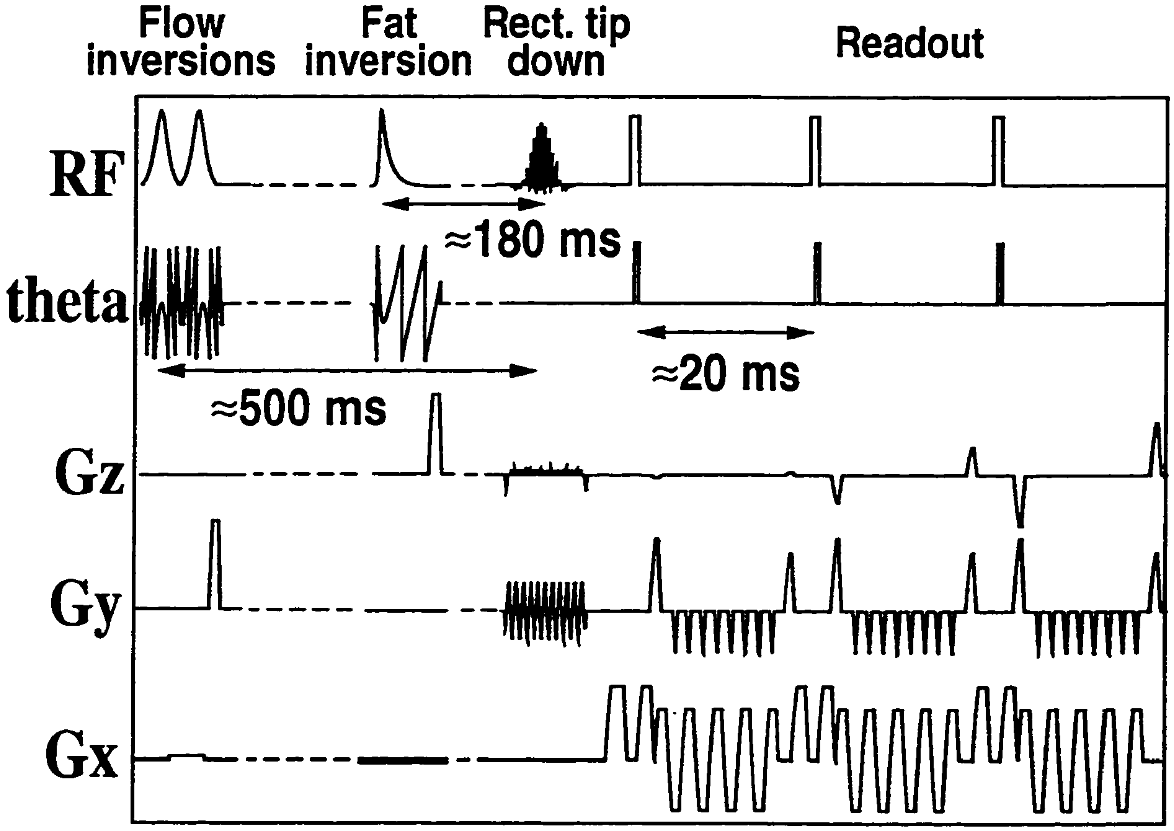

Figure 5.1: Pulse sequence diagram showing the two flow-inversion pulses, the fat-inversion pulse, the rectangular-tip-down pulse and the 3D GRASE readout. The long inversion times do not increase scan time since cardiac gating is used.

diagram in Fig. 5.1 shows (i) the two inversions used for flow suppression, (ii) the single inversion used for fat suppression, (iii) the tip-down pulse with a rectangular excitation profile used to reduce imaging time and (iv) the 3D GRASE waveforms. The 'theta' axis shows the phase of the RF pulses. The long inversion times did not increase the imaging time since we used cardiac gating with a TR of 1 to 2 cardiac cycles. This section describes the pulse sequence diagram, our careful management of SNR and the reduction of artifacts from EPI, RARE and transverse coherence.

5.2.1 3D GRASE imaging

We found the following observations useful in choosing a *k*-space trajectory. First, excellent resistance to off-resonance artifacts are provided by trajectories that acquire data on a Cartesian grid. Second, for imaging with a long TE, spin-echoes are needed to refocus the signal. Third, to achieve a reasonable scan time with high-resolution 3D imaging, a fast imaging trajectory is need to acquire the desired *k*-space region efficiently. Because of these three observations, we chose 3D GRASE because it acquires *k*-space more efficiently than 3D spin-echo imaging or 3D RARE. Originally conceived as a 2D trajectory, GRASE [97] is a combination of RARE and EPI [25]. While 2D GRASE [97] is sensitive to ghosting caused by off-resonance or by T_2 decay, this 3D version of GRASE [95] suffers from neither since it decouples the off-resonant phase evolution and T_2 decay.

Figure 5.2 shows that, in the k_x-k_y plane, the 3D GRASE trajectory is similar to EPI where off-resonant phase evolution is significant only along k_y, producing shifts along the y direction [40]. Two interleaves are shown: the 1st as a solid line and the 2nd as a dashed line. As shown in Fig. 5.1, the k_y and

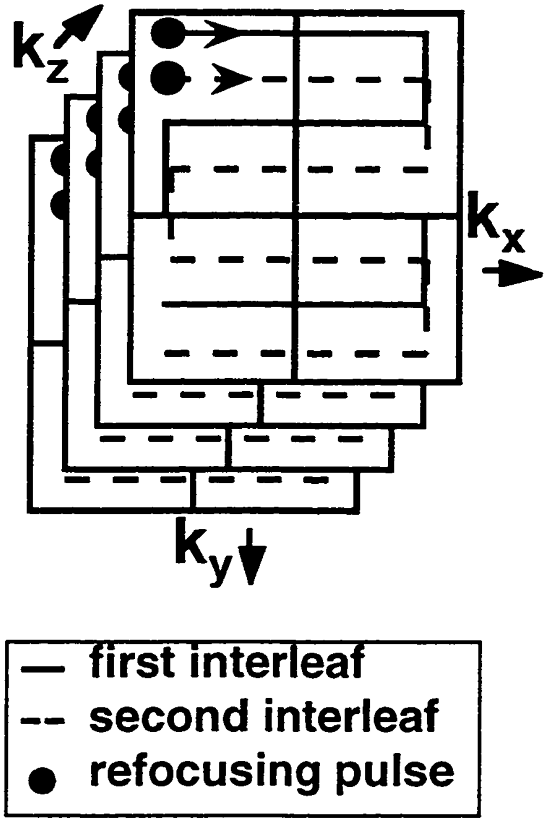

Figure 5.2: 3D GRASE k-space trajectory as viewed from k_x-k_y plane resembles EPI. Two interleaves are shown: the 1st as a solid line and the 2nd as a dashed line. Each interleaf begins with a refocusing pulse then acquires several lines in a given k_x-k_y plane. After another refocusing pulse, it jumps to a k_x-k_y plane with a different k_z value and acquires several lines in that plane, and so on.

k_z phase-encoding is rewound just before each refocusing 180° pulse to avoid transverse-coherence artifacts [97].

Figure 5.3 shows that, in the k_y-k_z plane, 3D GRASE is similar to RARE imaging where T_2 decay is significant only along k_z. The 1st and 2nd interleaves of an eight-interleaf sequence are shown. The 3rd and 4th interleaves acquire the rows in the bottom half of k-space not acquired by the 1st and 2nd interleaves. The 5th through 8th interleaves acquire the top half. To avoid accumulation of B_1 inhomogeneity effects on the refocusing 180s,

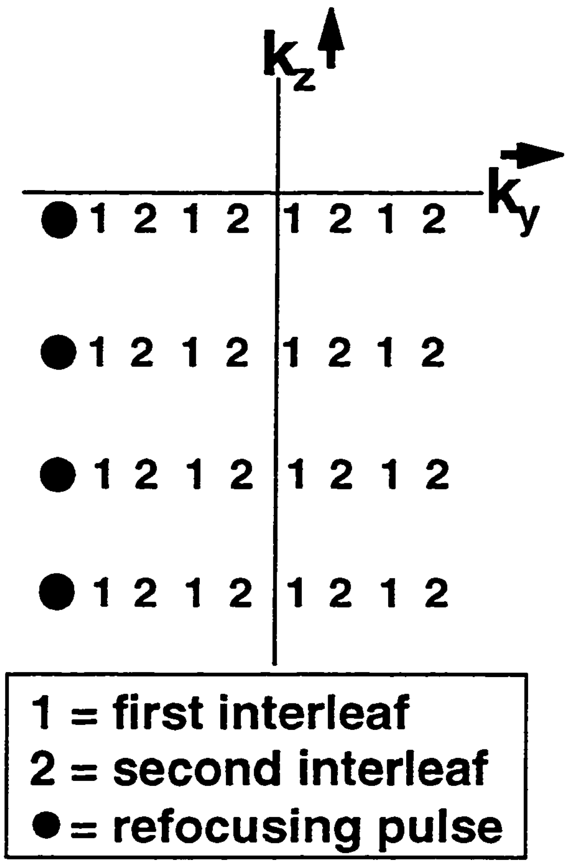

Figure 5.3: 3D GRASE *k*-space trajectory as viewed from k_y-k_z plane resembles RARE imaging. The 1st and 2nd interleaves of an eight-interleaf sequence are shown. After each refocusing pulse, one row is acquired from left-to-right. The 1st interleaf acquires all echoes labelled '1'. The 2nd interleaf acquires all echoes labelled '2'. The 3rd and 4th interleaves acquire the rows in the bottom half of *k*-space not acquired by the 1st and 2nd interleaves. The 5th through 8th interleaves acquire the top half.

the rotation axis of the tip-down pulse is oriented 90° with respect to the axis of rotation of the refocusing 180s; this is the well-known CPMG prescription [97]. An even-symmetric k_z-ordering is used to avoid amplitude discontinuities along k_z and the T_2 weighting can be altered by a circular shift of this k_z-ordering [98].

For the data-acquisition gradients, Fig. 5.1 shows that the G_x prewinders and rewinders were combined with the crushers for the refocusing pulses to reduce the time between refocusing pulses. To reduce the duration of the gradient waveforms, we used exponential ramps based on an L-R circuit model of the gradient subsystem [44].

5.2.2 Field-of-view restriction

Even with the fast 3D GRASE trajectory, imaging time can be long because we are acquiring a three-dimensional image at high resolution with cardiac gating. In Table 5.1, the "slab-select excitation" column lists the parameters for an image with resolution of 1.1 mm x 0.5 mm x 0.5 mm and a 15 cm field-of-view (FOV) in each direction. In Table 5.1, "data-acquisition per TR" is defined as the delay between the start of data-acquisition after the first refocusing 180 and the end of data-acquisition after the last refocusing 180. With 3888 interleaves, a heart-rate of 70 bpm and a TR of 2xRR, the scan time is 112 minutes which is clinically infeasible.

We reduced this imaging time by restricting the FOV. In the x direction, we used the data acquisition filter to restrict the FOV, as in 2DFT imaging. In the y and z directions, it is possible to use "inner-volume" imaging to restrict the FOV [99, 100]. Unfortunately, with this approach, long refocusing pulses are needed to avoid degradation of the slice profiles in the presence of B_1 inhomogeneity. Therefore, we used a two-dimensional excitation instead which has a rectangular excitation profile [96]. In Table 5.1, the "rectangular excitation" column lists the parameters for an image with a 5-cm FOV in each direction. Compared to the "slab-select excitation" column, the number of interleaves is reduced from 3888 to 432 and the imaging time is reduced from 112 minutes to 12 minutes.

	slab-select excitation	rectangular excitation
FOV (cm)	15	5
x resolution (mm)	1.09	1.09
y resolution (mm)	0.46	0.46
z resolution (mm)	0.46	0.46
data acq. per TR (ms)	85	85
heartbeats per excitation	2	2
no. excitations	3888	432
scan time (min) at 70 bpm	112	12

Table 5.1: 3D GRASE scan time. Scan time is dramatically reduced by using a rectangular excitation and the anti-aliasing filter to restrict the FOV in all three dimensions.

Figure 5.4 shows our rectangular excitation pulse with a duration of 13.8 ms. Along the y axis, there are no sidelobes but, along the z axis, the distance between the centers of the ghost sidelobe and the main lobe is 11.4 cm. The main-lobe magnetization falls to less than 2% beyond $y = +/- 2.75$ cm and $z = +/- 3.1$ cm. With a FOV of 5 cm (+/- 2.5 cm), there is no aliasing in the central 4.5 cm along y and the central 3.8 cm along z.

We chose a rectangular pulse which uses an EPI trajectory in excitation k-space [96] instead of a cylindrical pulse which uses a spiral trajectory [19] because off-resonance produces blurring of the cylindrical pulse but a relatively benign spatial shifting of the rectangular pulse.

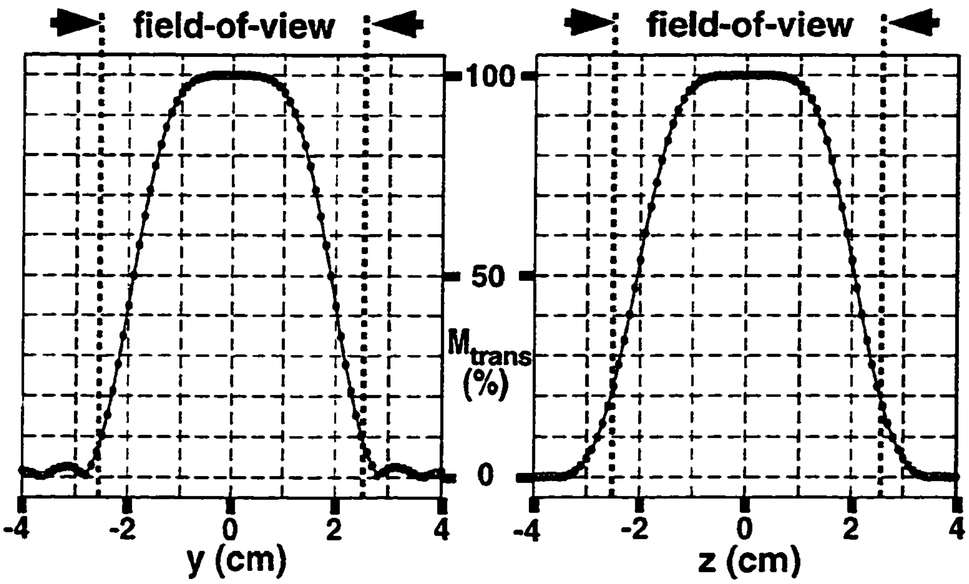

Figure 5.4: Profile of rectangular pulse used to reduce imaging time, showing the transverse magnetization vs. y and z position. With a 5-cm field-of-view, there is no aliasing in the central 4.5 cm along y and the central 3.8 cm along z. The pulse duration is 13.8 ms. There are no y sidelobes but the z-ghost sidelobes are 11.4 cm from the center.

In designing the rectangular-pulse, an important goal is to place the sidelobes beyond the view of the receiver coil or even outside the body. In theory, the sidelobe distance is determined by the density of the k-space trajectory. However, because of EPI ghosting [48], there are ghost sidelobes which are halfway between the k-space-density sidelobes and the main lobe. Fortunately, we were able to place these ghost sidelobes sufficiently far away from the main lobe.

5.2.3 Signal refocusing

For the refocusing 180° pulses, we used composite pulses [101] to achieve insensitivity to B_1 inhomogeneity. The duration of each of these pulses is only 1.5 ms. These composite pulses do not have excitation profiles with sharp transition regions but this is unimportant since the refocusing is not spatially selective.

5.2.4 Fat suppression

Fat suppression is important for preventing chemical-shift artifacts. Since our tip-down pulse that is selective in two spatial dimensions, it was infeasible to also make it spectrally selective. Therefore, to suppress fat in the presence of B_1 inhomogeneity, we chose inversion nulling using fat-selective adiabatic inversion pulses [102] since this is more compact than fat saturation using a CHESS sequence [103]. We avoided inverting the water signal otherwise incomplete recovery of the longitudinal magnetization would reduce SNR and increase the T_1 contrast.

The adiabatic pulses of Rosenfeld *et al.* [102] provided insensitivity to B_1 inhomogeneity. These pulses have one transition region that is much narrower than the other, allowing the narrower region to be more compact than that of a hyperbolic-secant pulse of similar duration. The delay, TI_{fat}, between the effective centers of the fat inversion and the rectangular tip-down depends on the heart rate, as shown in Fig. G.1b of Appendix G.

5.2.5 Flow suppression

Flow suppression is important for improving the visibility of the media and the atherosclerotic lesions. It increases the dynamic range available to display the media or lesion since the flow signal has a relatively high intensity. Also, it avoids ghosting or blurring of the flow signal which may obscure the plaque. To suppress flow in the presence of B_1 inhomogeneity, we chose "velocity-selective" inversion nulling over flow

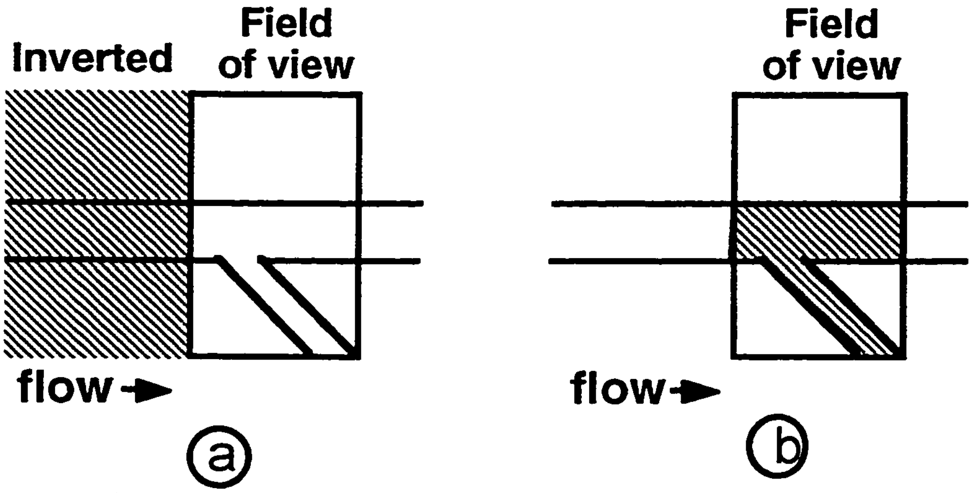

Figure 5.5: Velocity-selective inversion nulling in a typical imaging situation shown at: (a) the time of the inversion pulse and (b) the time of the cylindrical tip-down pulse.

saturation using a CHESS sequence [103] because (a) it is more compact and (b) it uses a longer delay until the tip-down pulse, allowing more inflow of suppressed blood. We avoided inverting the static signal since this would reduce SNR and increase T_1 contrast.

Figure 5.5 depicts how the inversion nulling is made velocity-selective [104]. Figure 5.5a shows a typical imaging situation at a time when the inversion is applied upstream of the FOV. After an appropriate delay, the tip-down pulse is applied. During this delay, non-inverted blood flows out of the FOV and is replaced by inverted blood, as shown in Figure 5.5b. Therefore, inverted blood is suppressed by inversion nulling and non-inverted blood is suppressed by outflow. With sufficient outflow, there will only be inverted blood in the imaging FOV at the time of the rectangular tip-down.

Since we wanted to suppress both arterial and venous flow, the flow-selective inversion needs to invert regions on both sides of the imaging FOV. To accomplish this, two inversions are used: a non-selective inversion followed immediately by a selective inversion. The selective inversion cancels the effects of the non-selective inversion in the imaging FOV. We used hyperbolic-secant adiabatic pulses [105] which provide excellent insensitivity to B_1 inhomogeneity. The delay, TI_{flow}, between the effective centers of the first flow inversion and the rectangular tip-down depends on the heart rate, as shown in Fig. G.1a of Appendix G which contains an extensive discussion of the flow-suppression timing. We placed the flow inversions before the period of fast flow and placed data acquisition during the period of slow flow. This maximized the flow suppression due to outflow and minimized the artifacts due to vessel motion.

One potential problem is the interaction of the flow and fat inversion pulses. Since the location of the region reverted by the second flow inversion varies with resonant frequency, as shown in Fig. 5.6, the second flow inversion may revert the fat signal in only part of the imaging FOV. In this case, the fat inversion will suppress the fat signal in only part of the imaging FOV. We avoided this problem by increasing the spatial width of the second flow-inversion so that, at the fat frequency, the entire imaging FOV is

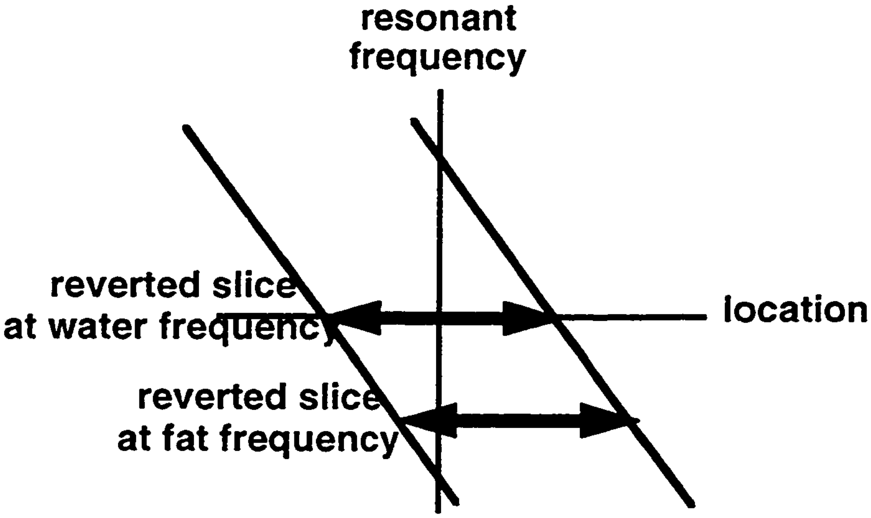

Figure 5.6: Location of the second flow inversion varies with resonant frequency. Fat suppression will fail in that part of the field-of-view unaffected by the second flow-inversion. This can be avoided by increasing the spatial width of the second flow-inversion.

reverted. We note that velocity-selective inversion nulling and fat-selective inversion nulling were previously combined by Simonetti *et al.* [106].

In addition to flow-selective inversion, there is another flow suppression mechanism which is inherent to spin-echo imaging sequences such as GRASE. The differences in gradient moments between the stimulated echoes and the spin-echoes produce dephasing of the flow signal [107]. Since the G_x waveform is the busiest gradient waveform in Fig. 5.1, this dephasing was encouraged by aligning the x axis with the direction of flow.

5.2.6 SNR improvement

In our imaging technique, great care had to be taken to achieve adequate SNR. Compared to magnetic resonance angiographic (MRA) images, SNR is reduced because of two reasons. First, the signal from flowing blood is the largest-amplitude signal in MRA images. Unfortunately, in our imaging technique, this signal is suppressed because it interferes with visualization of the atherosclerotic lesions. Second, our imaging technique typically uses much higher resolution than MRA imaging because we want to resolve the internal structure of the atherosclerotic lesions. To achieve adequate SNR, we used the following procedures.

5.2.6.1 Shimming

Careful shimming avoided broadening of the rectangular-excitation profile and reduced the subsequent aliasing of the excitation profile into the imaging FOV. With a poor shim, the rectangular-pulse profile may be broader than the imaging FOV and produce unwanted aliasing of signal from outside the FOV.

We adjusted the center frequency and linear shims in two steps. The first step used standard software provided by GE Medical Systems which obtains field maps in the axial, sagittal and coronal planes then calculates a least-squares linear fit for a specified region of interest. This first step is necessary to produce a reasonable rectangular-pulse profile for the second step. The second step used a field map obtained with a 3D GRASE scan with an 8-cm FOV, 2.5-mm resolution and the same rectangular pulse as in imaging. For this second field map, the FOV was larger than the rectangular-pulse profile to avoid spatial aliasing in the field map. A least-squares linear fit over the entire 8-cm FOV was used to refine the shim. This shimming procedure typically required about 15 minutes.

We note that off-resonance effects on the readout trajectory are insignificant; for example, with 20 ms data acquisition per spin-echo, 50 Hz off-resonance produces only a one-pixel shift.

5.2.6.2 Surface coil

A 7.6-cm diameter surface coil reduced the noise volume seen by the receiver. Careful placement of the surface coil minimized the distance between the coil and the carotid bifurcation, maximizing the signal from the imaging FOV.

5.2.6.3 Anisotropic resolution

The voxel size was increased by using anisotropic resolution where the voxel width was increased only in the x direction. To avoid SNR losses from a reduced data-acquisition time, we kept the same data-acquisition time as with isotropic resolution by reducing the gradient amplitude of the G_x readout lobes.

5.2.6.4 Repetition time

Whenever the average heart rate allowed a scan time of 12 minutes or less, we used a TR of 2 cardiac cycles. This allowed more T_1 recovery than a TR of 1 cardiac cycle and reduced the T_1 contrast in the image.

5.2.6.5 Homodyne detection

Homodyne detection was used to display the real part of the image [108] which yields a better SNR than magnitude display in low-SNR regions of the image. This works because the real part of the noise has a distribution with a mean value of zero whereas the magnitude of the noise has a distribution with a non-zero mean.

5.2.6.6 Minimizing T_2 decay

Figure 5.7 shows the T_2 values reported for components of atherosclerotic lesions at a field strength of 1.5 T [85, 86, 92]. There is variation in these values because the contribution of various short-T_2 components varies with the echo-time (TE) used for measurement and the composition of the core is heterogeneous [92]. Given these T_2 values, the total data-acquisition window per TR was restricted to about 90 ms to avoid excessive SNR losses from T_2 decay. Also, the *k*-space origin was acquired just after the first refocusing pulse. Acquiring the *k*-space origin after later refocusing pulses would increase the T_2 contrast but would also reduce the SNR.

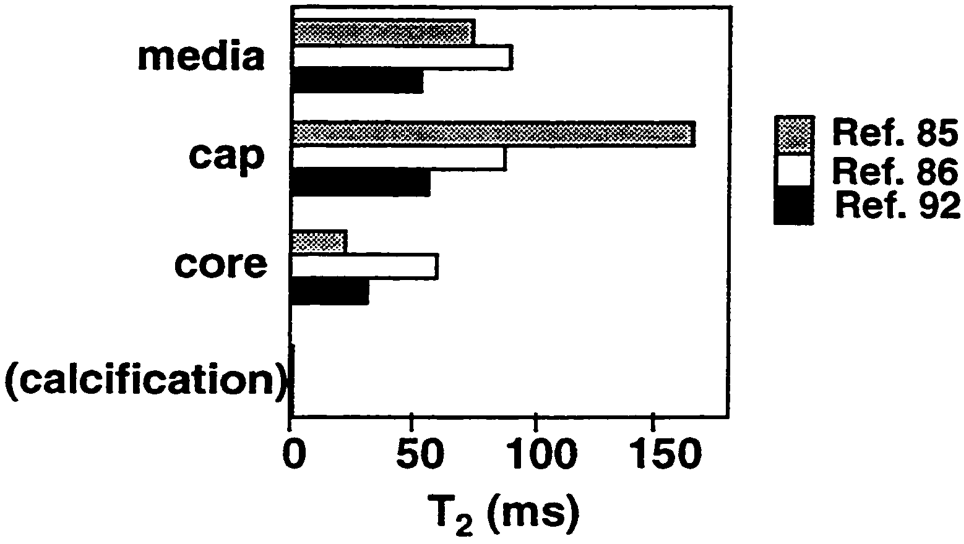

Figure 5.7: T_2 values at 1.5 T of tissue associated with plaque lesions. T_2-weighted imaging can distinguish among media, cap, core and calcification.

5.2.7 Ghost reduction

As in EPI, ghosting can be produced in GRASE by differences between data acquired during the positive and negative readout-gradient lobes. To correct these differences, we used calibration data acquired with the k_y and k_z phase-encoding turned off [48]. Our use of this calibration data is described in detail in Appendix A.

As in RARE, ghosting can be produced in GRASE by differences between the odd and even spin-echoes [109]. To reduce this RARE ghosting, we modified the EPI calibration process, allowing it to measure the differences between the odd and even spin-echoes. This is described in detail in Appendix A.

Ghosting can also be caused by off-resonance. To avoid, this, we used sliding readout delays [27, 30] in the k_y direction. The time between the refocusing 180s was kept constant but, for a given k_z value, each data-acquisition window was delayed by a progressively longer time. This slightly increased the time between the refocusing pulses but was essential to reduce ghosting caused by off-resonance.

5.2.8 Transverse-coherence artifact reduction

Stimulated echoes from the previous TR and from the flow and fat inversions can cause artifacts. To avoid this, we used crushers after the inversions, putting them on gradient axes that are different from each other and from those of the crushers for the refocusing 180s. We chose the crusher area so that it depends on the minimum width of the image voxel as given by $\max(1/\Delta x, 1/\Delta y, 1/\Delta z) \,/\, (\gamma / 2\pi)$ where Δx, Δy and Δz are the voxel widths in the x, y and z directions, respectively.

5.3 Results

Using a surface coil with a 7.6-cm diameter, we acquired images of the carotid bifurcations of normal volunteers and patients; and of human aorta specimens. Image parameters are given in Table 5.2.

Figure 5.8 shows images of a human aorta specimen immersed in attapulgite [110]. Attapulgite was used to avoid air-tissue susceptibility differences and was chosen because it contributes very little MR signal. (Attapulgite clay is a mineral containing aluminum-magnesium-silicate crystals. It is easily obtained as an anti-diarrheal medicine.) After autopsy, the aorta specimen was kept at about 4°C for 4 days and, before imaging, re-warmed to 37°C. A TR of 1000 ms was used to simulate cardiac gating. Hematoxylin-and-eosin staining was used for the histologic section shown in

Fig. 5.8a. Figures 5.8b-5.8d are views from the 3D GRASE image with arrows pointing to the lesion. The signal void in the core suggests calcification which was confirmed by the histology. The axial view in Fig. 5.8c corresponds to Fig. 5.8a. This axial view and the sagittal view in Fig. 5.8b show the cap thickness and core size. Figure 5.8d is a coronal view. Figures 5.8e-5.8f show ultra-short-TE spectroscopic images [83] both corresponding to Fig. 5.8c, with arrows pointing to the lesion. They were obtained with 0.2 ms TE, 70 ms TR, 3.5 mm slice thickness and a resolution of 0.55 mm and 61 Hz. The lipid spectroscopic image shows signal in areas corresponding to signal void in Fig. 5.8c, confirming successful lipid suppression in the 3D GRASE image.

	ex-vivo image		*in-vivo* images	
	field-of-view (cm)	resolution (mm)	field-of-view (cm)	resolution (mm)
x (superior-inferior)	6	0.50	4 (5 in Fig. 5.11)	1.11 (1.09 in Fig. 5.11)
y (posterior-anterior)	6	0.50	5	0.46
z (left-right)	6	0.50	5	0.46
gradient echoes per spin-echo	6		9	
spin-echoes per TR	3		3	
data acq. per spin-echo (ms)	19		20	
data acq. per TR (ms)	90		85 (90 in Fig. 5.11)	
TE (ms)	33		31 (33 in Fig. 5.11)	
no. excitations	800		432	

Table 5.2: Parameters for atherosclerotic-plaque images.

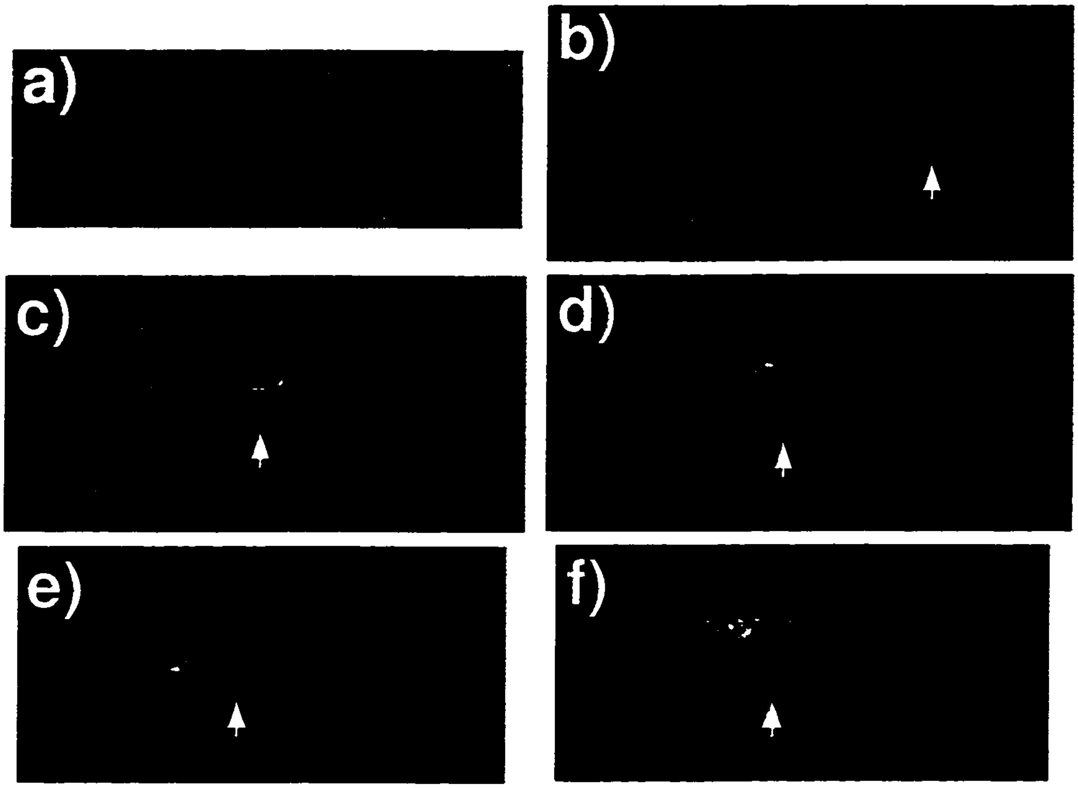

Figure 5.8: 3D GRASE images of a human aorta specimen suspended in attapulgite shows calcified lesion. Arrows point to the lesion. (a) Histologic slice (H&E staining), (b) sagittal view, (c) axial view corresponding to Fig. 5.8a, (d) coronal view, and (e) spectroscopic water and (f) spectroscopic lipid images both corresponding to Fig. 5.8a.

Figure 5.9 shows images of the left carotid bifurcation of a normal volunteer. Figure 5.9a is an axial localizer image with a 16-cm FOV. The box shows the 5-cm FOV used for the 3D GRASE image which was obtained with a TR of 1 heartbeat and an average heart rate of 40 bpm. Figures 5.9b-5.9c are axial and sagittal views from the 3D GRASE image showing uniform wall thickness and excellent flow suppression. Figure 5.9d is an oblique view from the 3D GRASE image obtained with software and computing resources kindly provided by Yen *et al.* [111]. It shows unobstructed carotid-artery lumens in the region of the bifurcation.

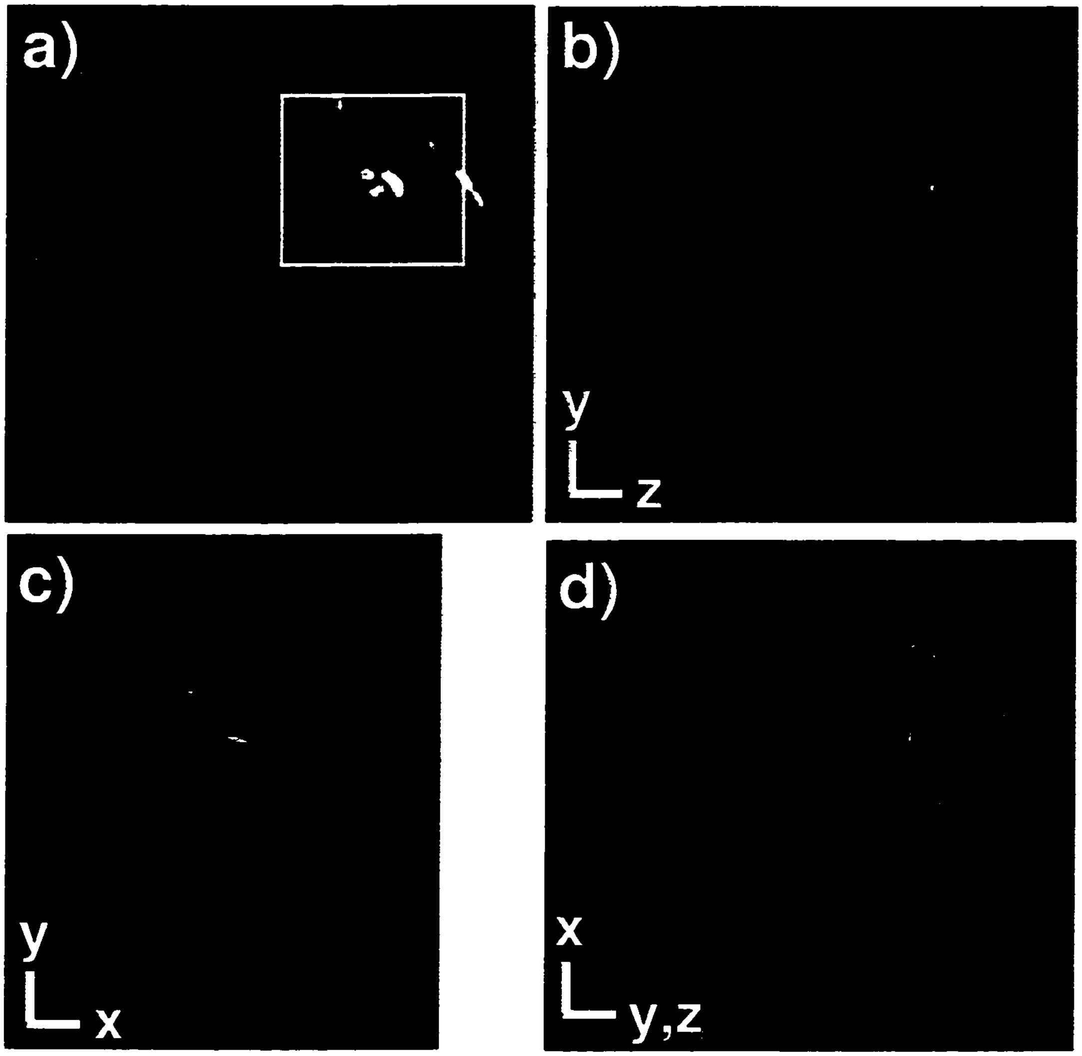

Figure 5.9: 3D GRASE images of the left carotid bifurcation of a normal volunteer. Axes are described in Table 5.2. (a) 2DFT axial localizer, box corresponds to Fig. 5.9b, (b) axial, (c) sagittal and (d) oblique views show excellent flow suppression, uniform wall thickness and an unobstructed lumen.

Figure 5.10 shows images of a patient whose ultrasound indicated 50% stenosis of the right internal carotid artery (ICA). Figure 5.10a is an axial localizer image with a 16-cm FOV. The box shows the 5-cm FOV used for the 3D GRASE image which was obtained with a TR of 2 heartbeats and an average heart rate of 75 bpm. Figures 5.10b-5.10d are views from the 3D GRASE image with arrows pointing to the lesion. Figure 5.10b is an axial view showing the ICA lumen narrowed by plaque. Figure 5.10c is a sagittal view, showing the media, the cap thickness and the core size. Figure 5.10d is an oblique view of a long section of the ICA, showing the longitudinal extent of the lesion. It also shows approximately 50% narrowing which is in agreement with the ultrasound data.

Figure 5.11 shows images of another patient whose ultrasound also indicated 50% stenosis of the right internal carotid artery. Figure 5.11a is an axial localizer image with a 16-cm FOV. The box shows the 5-cm FOV used for the 3D GRASE image which was obtained with a TR of 2 heartbeats and an average heart rate of 65 bpm. Figures 5.11b-5.11d are views from the 3D GRASE image with arrows pointing to the lesion. Figure 5.11b is an axial view showing the ICA lumen narrowed by plaque. Figures 5.11c-5.11d are sagittal and oblique views showing that the lesion is located at the bifurcation. The distinct regions of signal void within the lesion suggest a heterogeneous plaque perhaps due to prior ulceration. Figure 5.11d shows approximately 50% narrowing of the ICA, in agreement with the ultrasound data.

In Figs. 5.10-11, we note that blood generally appears bright in the axial localizer images because of inflow enhancement but generally appears dark in the corresponding axial views of the GRASE images because of the flow-suppression pulses. There are some vessels for which blood appears bright in the GRASE images because the flow in these vessels is perpendicular to the direction of the flow suppression.

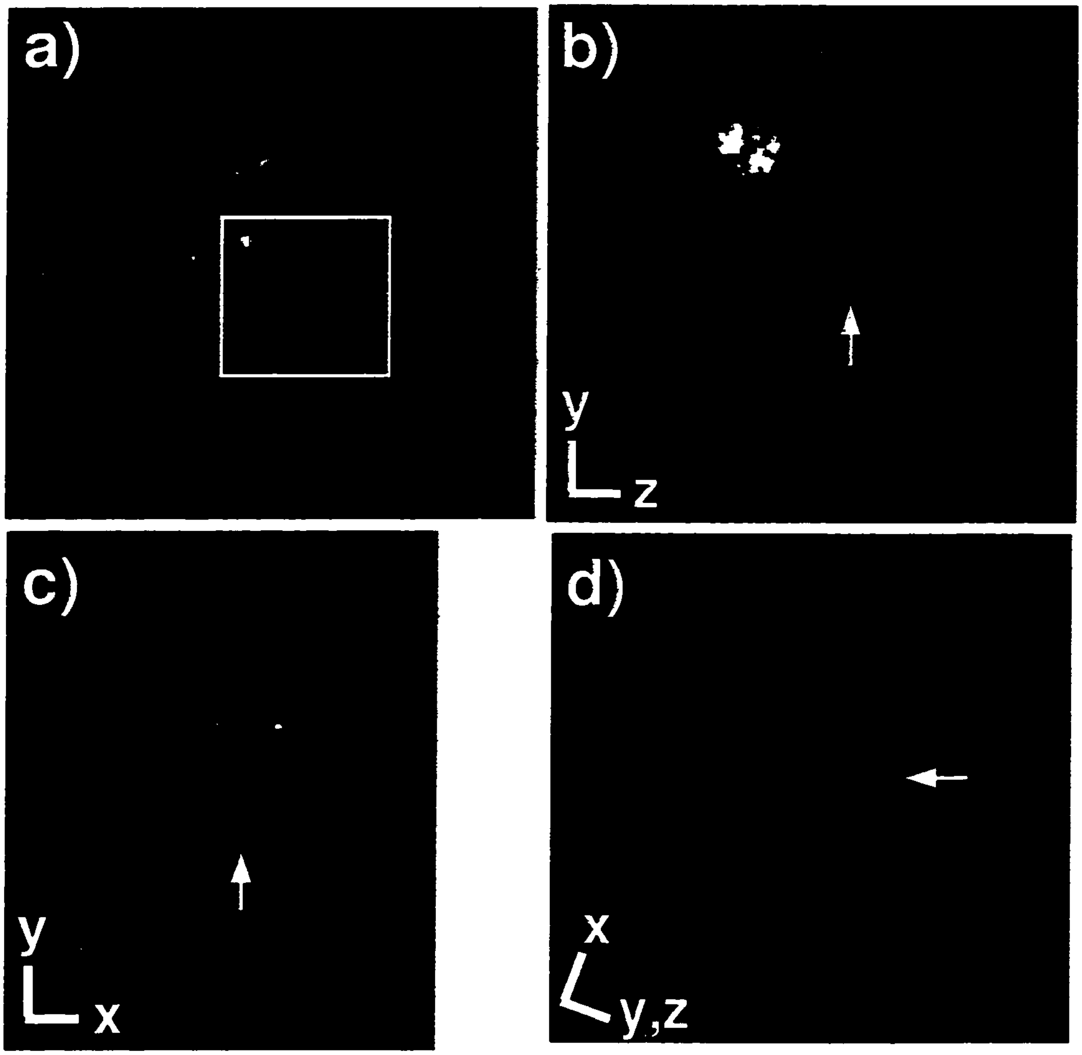

Figure 5.10: 3D GRASE images of a patient whose ultrasound indicated 50% stenosis of the right ICA. Arrows point to the lesion. Axes are described in Table 5.2. (a) 2DFT axial localizer, box corresponds to Fig. 5.10b, (b) axial view shows the ICA lumen narrowed by plaque, (c) sagittal view shows the cap thickness and core size and (d) oblique view shows the longitudinal extent of the lesion; it also shows 50% stenosis which agrees with the ultrasound findings.

5.4 Discussion

5.4.1 SNR

A comparison of the SNR in our images demonstrates the importance of using a small surface coil and of minimizing its distance from the imaging FOV. The SNR is best in the *ex-vivo* image since the noise volume consisted mostly of the specimen itself; the attapulgite contributed very little noise. The SNR is better in the normal-volunteer image than in the patient images because, in the volunteer image, the bifurcation was about 2.5 cm from the center of the surface coil whereas, in the patient images, because of larger neck circumferences that distance was about 4.3 cm and 3.4 cm respectively.

5.4.2 Motion

Motion during the scan is a potential problem, particularly since the scan time is on the order of 10 minutes. We were concerned with three types of motion: (i) Swallowing motion was avoided by asking volunteers and patients not to swallow during the scan. If they had to swallow, they could signal the operator and the scan would be paused [91]. (ii) Bulk motion of the head was avoided by bracing the head with sponges. (iii) Artifacts caused by motion of the blood-vessel walls were reduced by limiting data acquisition to a period of about 100 ms during diastole.

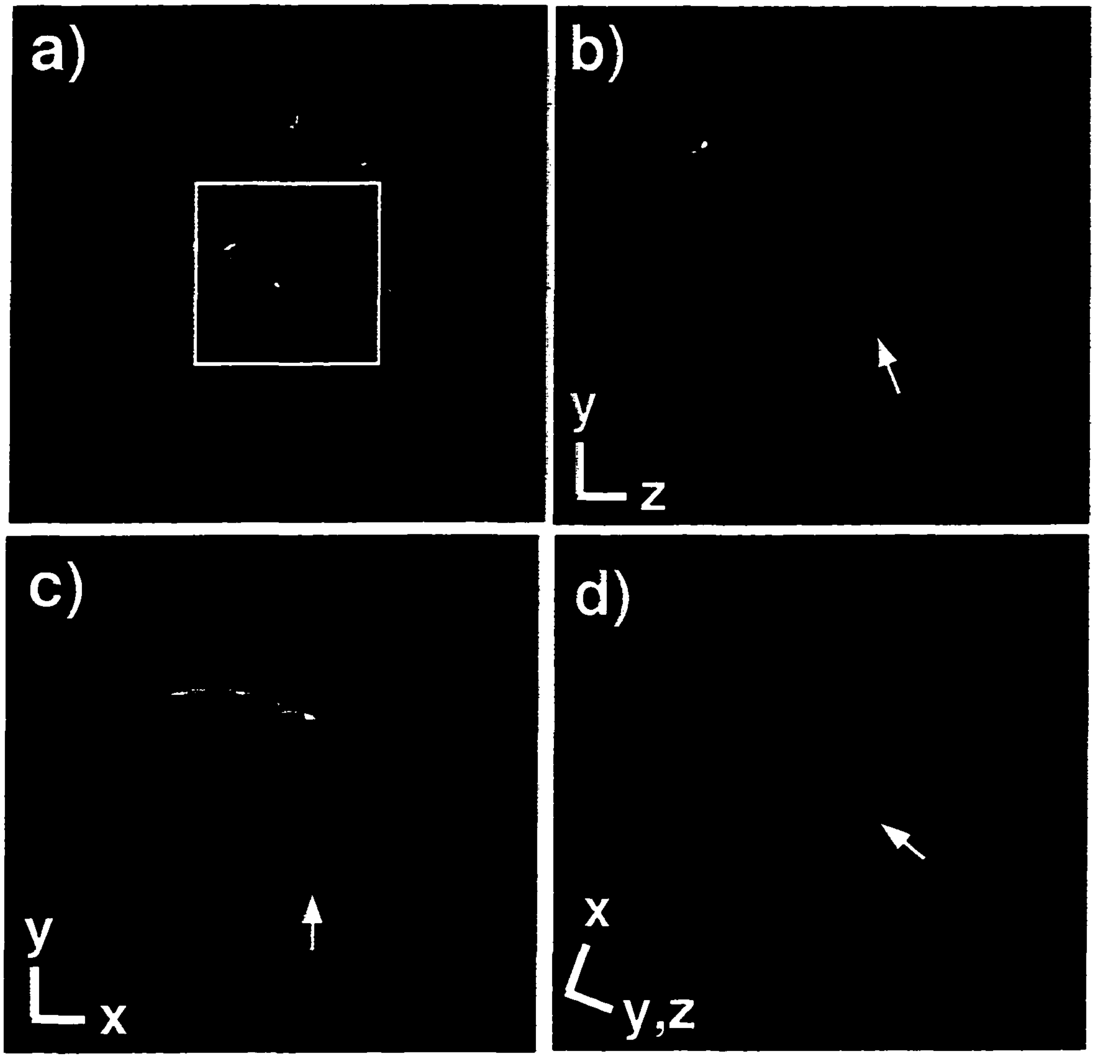

Figure 5.11: 3D GRASE images of another patient whose ultrasound also indicated 50% stenosis of the right ICA. Arrows point to the lesion. Axes are described in Table 5.2. (a) 2DFT axial localizer, box corresponds to Fig. 5.11b, (b) axial view shows the ICA lumen narrowed by plaque, (c) sagittal and (d) oblique views show that the lesion is located at the bifurcation producing 50% stenosis in agreement with the ultrasound results. The distinct regions of signal void within the lesion suggest a heterogeneous plaque perhaps due to prior ulceration.

5.4.3 Comparison with multi-slice 2D RARE

Multi-slice 2D RARE has been used by several investigators for T_2-weighted imaging of plaque [85-87, 89-93]. It can be compared to 3D GRASE in terms of SNR, scan time, viewing angle and flow suppression. SNR efficiency, which is defined as $\mathrm{SNR}/\sqrt{\text{scan time}}$, normalizes the SNR comparison for differences in scan time. To compare SNR efficiency, we will first separately compare SNR and scan time.

5.4.3.1 SNR comparison

The following factors distinguish the SNR of multi-slice 2D RARE and 3D GRASE: readout time, T_1 recovery and the shape of the tip-down excitation profile. We will assume that (i) both techniques use the same voxel size, (ii) both techniques use the same data-acquisition window per TR so that T_2 decay has similar effects and (iii) multi-slice 2D RARE acquires the same FOV as 3D GRASE by, for example, using its refocusing pulses to restrict the FOV in the y direction [99, 100].

Multi-slice 2D RARE has a shorter total readout time for any given voxel than 3D GRASE. Suppose there are N_z slices in 2D RARE or, equivalently, N_z voxels in 3D GRASE. In 3D GRASE, signal is received from a given voxel during the entire readout time. However, in multi-slice 2D RARE, signal is received from a given voxel for only $1/N_z$ of the total readout time. Since SNR is proportional to the square root of readout time [23], for N_z on the order of 100, readout-time differences impart a 10-fold SNR advantage to 3D GRASE.

3D GRASE allows less T_1 recovery than 2D RARE since all of its refocusing and tip-down pulses affect the entire 3D volume. However, in multi-slice 2D RARE, excitation of the slices can be interleaved, allowing a longer effective TR. Let M_z be the steady-state longitudinal magnetization just before the tip-down and M_0 be the equilibrium magnetization. With three refocusing 180s per TR, it can be shown that M_z is given as follows:

$$M_z = M_0\left[1 - e^{-(TR-\frac{5}{2}TE)/T_1}\left(2 - 2e^{-TE/T_1} + 2e^{-2TE/T_1} - e^{-\frac{5}{2}TE/T_1}\right)\right]. \tag{5.1}$$

For 2D RARE, we assume a best-case TR of infinity. This is achieved by interleaving acquisition of the slices so that TR >> T_1. In this case, M_z/M_0 is 1. For 3D GRASE, we assume a worst-case TR of 750 ms and a TE of 30 ms. This is achieved when the heart rate is 80 bpm and the TR is one cardiac cycle. In this case, for muscle with a T_1 of 850 ms [112], M_z/M_0 is about 0.5. Therefore, T_1-recovery differences impart a 2-times SNR advantage to multi-slice 2D RARE. We note that M_z does not depend strongly on the number of refocusing 180s if the delay between the tip-down pulse and the final refocusing 180 is much less than TR.

For 3D GRASE, the tip-down excitation profile is less uniform than for 2D RARE. For 2D RARE, ripples in the slice-select profile are typically only on the order of 0.01 of the maximum value. However, for 3D GRASE, the portion of the rectangular profile in the FOV can be as low as 0.6 of the maximum value.

In summary, considering the three effects discussed above, the SNR of 3D GRASE is larger than the SNR of multi-slice 2D RARE by a factor of about 10 x 0.5 x 0.6 = 3.

5.4.3.2 Scan-time comparison

Multi-slice 2D RARE uses more refocusing and excitation pulses than 3D GRASE to acquire the same region of *k*-space. To acquire the same amount of data with only one slice per cardiac cycle, multi-slice 2D RARE requires a longer scan time. With multiple slices in each cardiac cycle, multi-slice 2D RARE becomes more susceptible to slice misregistration because of blood-vessel motion.

The scan-time comparison can be quantified by considering the duty cycle,

$$DC = (\text{data-acquisition time})/(\text{total time}). \qquad (5.2)$$

In Appendix H, the ratio of duty cycles is given by Eq. H.5:

$$\frac{\mathrm{DC}_{\mathrm{GRASE}}}{\mathrm{DC}_{\mathrm{RARE}}} = \frac{(R+2C)+(A-P)}{\left(\frac{R+2C+S}{N}+P\right)+(A-P)} \qquad (5.3)$$

where

A = time for one gradient-echo lobe,

N = no. gradient echoes per spin echo,

R = time for refocusing 180,

C = time for one crusher,

P = time for G_y blips in GRASE (a G_y blip coincides with each transition of the G_x sawtooth)

S = time for sliding readout delay in GRASE,

For the imaging parameters in Table 5.1, we have the following values: A = 2.30 ms, N = 9, R = 1.54 ms, P = 0.87 ms, C = A (crusher area is equal to the readout-lobe area) and S = A (as given by Cho et al. [27] and Farzaneh et al. [30]). The resulting duty-cycle ratio of 2.3 means that multi-slice 2D RARE requires more than twice the scan time of 3D GRASE. An even larger duty-cycle ratio would result if we did not make assumptions (ii)-(iv) in Appendix H. In particular, multi-slice 2D RARE uses spatially-selective refocusing pulses which are longer than the non-selective refocusing pulses used by 3D GRASE.

Therefore, RARE can have a shorter scan time if it acquires data from 3 or more slices per cardiac cycle. However, as the number of slices per cardiac cycle increases, the spatial misregistration among slices increases.

5.4.3.3 SNR-efficiency comparison

From the previous two sub-sections, we have a GRASE-to-RARE SNR ratio of 3 and a GRASE-to-RARE scan-time ratio of n/2.3 where n is the number of slices for which 2D RARE acquires data in each cardiac cycle. Therefore, the GRASE-to-RARE SNR-efficiency ratio is $3 \times \sqrt{2.3/n} = 4.5/\sqrt{n}$. For the SNR efficiency of RARE to exceed that of GRASE, we must have $n \geq 21$. That is, 2D RARE must acquire data for more than 21 slices in each cardiac cycle, which is clearly impractical.

5.4.3.4 Viewing-angle comparison

3D imaging offers isotropic resolution and the ability to view the image in an arbitrary scan plane. Multi-slice 2D images can be reformatted to arbitrary scan planes but there are two problems. First, motion during data acquisition can cause spatial misregistration among the slices. Assuming that both techniques use the same data-acquisition window per TR, if 2D RARE acquires multiple slices in each cardiac cycle, the entire multi-slice data set will be acquired over a larger portion of the cardiac cycle and therefore experience more motion than the 3D GRASE data set. Second, there is blurring in the slice-select direction because the slice profile is typically not a 'sinc'. In multi-slice imaging, it can be said that *k*-space data is multiplied by the Fourier transform of the slice profile [113]. If the slice profile is a 'sinc' then *k*-space data is multiplied by a 'rect'. However, since the slice profile is typically not a 'sinc' there is uneven weighting of the spatial frequencies which produces blurring.

5.4.3.5 Flow-suppression comparison

Suppose that, in each cardiac cycle, two flow inversions (or a single flow-saturation pulse) precede all tip-down pulses. For multi-slice 2D RARE, the T_1-nulling of blood cannot be optimized for all slices and flow suppression will vary from slice to slice. 3D GRASE can achieve better flow suppression since the T_1-nulling only needs to be optimized for a single tip-down pulse.

However, with high-grade stenoses which reduce the velocity through the carotids, there may be insufficient outflow for uniform flow suppression through the entire 3D GRASE volume. In such cases, multi-slice 2D RARE can achieve better flow suppression since it requires less outflow. However, uniform flow suppression requires preceding each tip-down pulse with a saturation pulse, resulting in a longer total scan time or a longer data-acquisition window per TR.

5.4.4 Higher-performance gradients

Higher-performance gradients than the ones we used in acquiring our images are becoming available, for example, gradients with an amplitude of 40 mT/m and a slew rate of 150 mT/m/ms. These new gradients would have improved our imaging performance in two ways.

First, for a given tip-down-pulse profile, improvements in gradient performance would have allowed greater speed through excitation *k*-space, making the tip-down pulse less susceptible to off-resonance distortion. Furthermore, for a given pulse duration, improvements in gradient performance would have allowed more excitation *k*-space area to be covered, producing a more sharply-defined pulse profile.

Second, for a given data-acquisition window, improvements in gradient performance would translate into slightly higher SNR. With the cardiac scanner's gradients, we could have shortened the durations of the crushers and the phase-encode prewinders and rewinders. For the parameters in Table 5.1, the time saved could have been used to increase the data-acquisition time and therefore the SNR by about 17%. Alternatively, imaging time could have been reduced albeit with an accompanying decrease in SNR.

5.5 Conclusions

Multi-slice 2D RARE has been used for *in-vivo* black-blood imaging of atherosclerotic plaque because it provides good off-resonance properties and flexible T_2 contrast. We employed 3D GRASE because it offers better resolution in the slice-select direction, better SNR efficiency, arbitrarily-oriented views and better flow suppression. While 2D GRASE is sensitive to ghosting caused by off-resonance or by T_2 decay, 3D GRASE suffers from neither since it decouples the T_2 decay and the evolution of the off-resonant phase.

Cardiac gating is important in achieving good flow suppression and avoiding systolic vessel motion. Unfortunately, with high resolution and three spatial dimensions, cardiac gating can make the imaging time very long. To achieve reasonable scan times, we used a rectangular pulse to restrict the field-of-view.

For *in-vivo* imaging of atherosclerotic plaque, SNR is the current bottleneck in achieving higher resolution and shorter scan times. For imaging the carotid bifurcation, we used a 7.6-cm-diameter surface coil and found that SNR was very sensitive to the distance of the bifurcation from the surface coil. We also found that off-resonance distortion of the rectangular pulse could effectively reduce SNR through aliasing of signal from outside the field-of-view. Therefore shimming was very important in achieving adequate SNR.

With the rectangular pulse, we obtained 3D images with a field-of-view of 5 cm x 5 cm x 5 cm, resolution of 0.5 mm x 0.5 mm x 1.1 mm, cardiac gating, fat suppression and excellent flow suppression in scan times of about 12 minutes. We obtained *in-vivo* morphologic images of atherosclerotic plaque lesions showing the cap thickness and core size.

Chapter 6

Summary

6.1 Conclusions

Cardiovascular imaging requires fast MRI to avoid artifacts from respiratory and cardiac motion; voluntary and involuntary forms of bulk motion, such as fidgeting or twitching; and motion of the blood vessels themselves caused by pulsatile blood flow. Fast MRI is also required to achieve reasonable scan times for three-dimensional imaging which is useful for interrogating the irregular geometries shown by atherosclerotic-plaque lesions.

Unfortunately, while fast MRI is less sensitive than conventional MRI to artifacts caused by motion, it is more sensitive to artifacts caused by blood flow, off-resonance and imperfections in the MRI scanner. In this thesis, novel imaging sequences have been designed to reduce the sensitivity of fast MRI to these artifacts and to achieve reasonable scan times for high-resolution, three-dimensional imaging. This imaging-sequence design encompassed both image-acquisition schemes and excitation schemes.

Image acquisition is a linear process since it can be viewed as sampling the Fourier transform of the image or, in the lexicon of MRI, sampling readout *k*-space. While this sampling can be achieved in many different ways, this thesis employed a linear-systems approach to: (i) design readout *k*-space trajectories that reduce artifacts caused by motion, flow and off-resonance and (ii) analyze artifacts caused by imperfections in the MRI scanner and correct them during image reconstruction. In general, artifacts are produced because any imaging technique traverses a path in a multi-dimensional *k*-space and images are made by projecting the data acquired along that path onto only a few of those dimensions. It is this collapse of many dimensions into a few dimensions which results in artifacts.

While excitation is, in general, a non-linear process, there is a rich literature describing excitation pulses based on exact solutions and linear approximations of the Bloch equation which governs MRI [19, 102, 105]. This thesis employed several excitation schemes to reduce imaging time and to suppress the signal from fat and flowing blood, even in the presence of spatial inhomogeneity of the main magnetic field, B_0, and the excitation magnetic field, B_1.

6.2 Contributions

My contributions in this thesis are summarized here.

Reducing flow artifacts in echo-planar imaging

I modified the echo-planar imaging (EPI) trajectory to dramatically reduce its sensitivity to signal dropouts and ghosting caused by blood flow. Specifically: (i) inside-out EPI reduces artifacts caused by flow in the phase-encode direction, and (ii) partial-flyback EPI reduces artifacts caused by flow in the readout direction; it can be applied to any EPI trajectory whether inside-out EPI, partial-Fourier EPI or conventional top-down EPI.

Real-time velocity imaging

For velocity imaging, bowtie imaging acquires data in the presence of time-variant gradients to achieve several advantages over phase-contrast imaging. It acquires a full velocity spectrum, obviating the assumption of a single velocity per spatial location, in real time (30 frames/sec) without cardiac gating. I modified the bowtie imaging trajectory to almost double its time resolution and greatly reduce its sensitivity to blurring caused by off-resonance.

Atherosclerotic-plaque imaging

For imaging of atherosclerosis, I have shown how to acquire three-dimensional images with sub-millimeter resolution and cardiac gating, using two inversions for flow suppression and a rectangular excitation to reduce scan times to about 10 minutes. I have used these images to demonstrate the cap thickness and core size of the lesions; it is hoped that such morphologic features can predict which lesions will rupture and thereby cause sudden events such as stroke.

6.3 Future work

All of the images in this thesis were acquired on a commercially available, GE Signa 1.5 Tesla scanner with gradient performance no better than 22 mT/m amplitude and 20 mT/m/ms slew rate. New gradients which can improve both excitation and data-acquisition performance are becoming available, for example, gradients with an amplitude of 40 mT/m and a slew rate of 150 mT/m/ms. These gradients would provide greater speed through *k*-space, allowing less evolution of off-resonance- and flow-induced phase, making the excitation profile or the image less sensitive to distortion from off-resonance and flow. Furthermore, for a given RF-pulse duration or data-acquisition time, the faster gradients allow more excitation *k*-space area to be covered, producing a more sharply-defined excitation profile or increasing the achievable image resolution.

For echo-planar imaging, future work may include the following:

(a) modifications of the EPI trajectory which exploit higher-performance gradients, as described in Section 3.10.3,

(b) modifications of the EPI which improve flow properties without degrading off-resonance properties,

(c) exploiting the unused time in partial-flyback EPI to produce a field map, navigator data or other useful data.

Items (b) and (c) are discussed further in Appendix I.

One future application for bowtie imaging is assessing cardiac-valve disease. For this situation, the velocity field-of-view will have to be increased from the 2 m/s of the images shown in this thesis to about 5 or 6 m/s. This can be achieved by using the faster gradients or by using multishot bowtie imaging where the shots are interleaved along the velocity-encoding direction. A potential problem is unwanted signal from the myocardium and epicardial fat, particularly if this signal is of greater intensity than the signal from the flowing blood and causes a dynamic-range problem. This unwanted signal can be avoided by using the faster gradients to design a thinner cylindrical excitation or by using a contrast agent to increase the signal from flowing blood.

Here are some other issues for velocity imaging or, in general, motion imaging:

(a) Can we use a greater portion of the bowtie trajectory to produce an image?

(b) Can we use the bowtie trajectory or a similar trajectory to image acceleration?

(c) Can we simultaneously image two velocity directions?

(d) Can we find a useful *k*-space description of the effects of off-resonance on moving spins? Perhaps the multiple resonant-frequency dimensions alluded to in Section 4.2.5 can be used.

Issues (a) through (c) are considered in more detail in Appendix J.

For atherosclerotic-plaque imaging, the current bottleneck is SNR; there are several possibilities for pushing through this bottleneck. The first is the design of better receiver coils: the carotid images shown in this thesis were acquired with a 7.6-cm diameter surface coil. A better coil design might involve acquisition of the quadrature component of the MR signal and be less sensitive to the distance of the coil from the carotid bifurcation. The second possibility is the use of higher field strengths such as 3.0 or 4.0 T. While the SNR gain resulting from the increase in field strength is discounted by the increase in T_1 values, there will still be a net gain. A third possibility is the development of contrast agents that are selectively taken up by the core of the plaque lesion. A fourth possibility is time-interleaving the acquisition of multiple slabs. However, it can be shown that the SNR reduction caused by the decrease in data-acquisition time per slab outweighs the SNR improvement caused by the increase in T_1-recovery time.

Other questions for atherosclerotic-plaque imaging are as follows:

(a) In addition to T_2-weighted images, can we obtain T_1-weighted images without increasing the scan time? It may be possible with two tip-down excitations per heartbeat where the second image will be T_1-weighted.

(b) In addition to water-signal images, can we obtain lipid-signal images without increasing the scan time? Perhaps with two tip-down excitations per heartbeat, one which is water-selective and one which is fat-selective.

(c) Can we shorten the total scan time without sacrificing SNR?

Finally, it is interesting to consider the possibility of *k*-space trajectory design through optimization of some image-quality metric. There are several problems with this approach. First, as noted in Section 3.7's discussion of choosing the flyback ratio in EPI, the image quality produced by a given imaging technique depends strongly on the object being imaged. This issue may be addressed by establishing standard objects such as a carotid flow phantom. Second, it is difficult to reduce the human visual system to a few numbers. Differences between actual and ideal images may be computed in many different ways and it would be challenging to correlate computed numbers with subjective ratings.

6.4 Coda

MRI has already made inroads in vascular imaging where it is prescribed in conjunction with, and even instead of, X-ray angiography. It remains to be seen whether MRI will be clinically feasible and economically viable for cardiac imaging. I hope that the work in this thesis will contribute in some way to the success of MR in cardiovascular imaging.

Appendix A

EPI and RARE ghosts

This appendix describes how EPI and RARE ghosting is reduced by using calibration data acquired before the image. EPI ghosting is an issue in Chapters 3-5 and RARE ghosting is an issue in Chapter 5.

A.1 EPI ghosts

In EPI and in GRASE, ghosting can be produced by differences between data acquired during the positive and negative readout-gradient lobes. These differences can be corrected prior to imaging by adjusting the delay between data-acquistion and the readout-gradient waveforms [26] or adding a phase offset to data acquired during the negative readout-gradient lobes [39]. Alternatively, corrections can be applied in post-processing using calibration data acquired before or during imaging [48, 114-119]. Our correction technique follows this post-processing approach.

Our correction method acquires calibration data using two TRs with the phase-encoding turned off. Our method is different from those described in Refs. [26, 39, 48, 114-116] because it combines corrections for phase errors, delay errors and filter asymmetry while explicitly avoiding off-resonance effects on the correction factors. It does not attempt off-resonance correction because two calibration TRs cannot yield any meaningful estimate of the field map. A correction method that simultaneously removes positive-negative lobe differences, off-resonance effects and T_2 blurring is described by Wan *et al.* [119]. Unfortunately, this method requires many more calibration TRs than our method.

There are other methods that explicitly avoid off-resonance effects on the correction factors [117, 118]. Hu *et al.* [118] acquire calibration data with the phase encoding on. The resulting calibration data has lower SNR than with the phase encoding turned off and can yield unreliable corrections. While Mandeville *et al.* [117] use a single calibration TR, we use two calibration TRs for the following reasons. First, a single calibration TR requires the time-evolution of the off-resonant phase to be linear, which is not so when projecting over a volume with spatially-variant off-resonance. A single calibration TR also requires eddy-current effects to have the same periodicity as the readout-gradient waveform, which is not so in the presence of readout-gradient prewinders, rewinders and crushers. Second, two calibration TRs are useful for reducing RARE ghosts, as will be described later. Third, our correction method was originally designed for the inside-out EPI trajectory described in Chapter 3 which requires two calibration TRs to correct differences between the top and bottom halves of *k*-space, as will be described later.

More accurate correction techniques, which do not require many of the assumptions we will make, measure the *k*-space trajectory [120] or use a linear-systems model to predict the eddy currents [121]. Unfortunately, these techniques require extensive measurement of the particular waveforms [120] or the particular scanner [121] being used.

A.1.1 Theory

The differences between data acquired during the positive and negative readout-gradient lobes can have several causes, including: (a) a delay between data acquisition and G_x waveform, (b) error in prewinder area, (c) eddy currents, (d) off resonance and (e) a data-acquisition filter with an asymmetric impulse response.

We use two extra TRs to obtain calibration data. The 1st calibration TR is the same as an imaging TR except that the phase-encoding pulses are turned off. For this 1st calibration TR, a comparison of each echo to the first echo yields the inter-echo differences. However, it also yields phase differences caused by off-resonance. We do not want the off-resonant phase differences because they are produced by an object that is a projection along the y and z directions. Because the resonant frequency varies along the projection directions, these off-resonant phase differences are unrelated to any one resonant frequency and are therefore meaningless.

To remove these off-resonant phase differences, a 2nd calibration TR is acquired which is identical to the 1st calibration TR but with all gradient waveforms negated. Since off-resonance affects the two calibration TRs in the same way, comparison of the jth echo in the 1st and 2nd calibration TRs yields all of the positive-negative lobe differences for the jth echo except those caused by off-resonance.

The following discussion pertains to the jth gradient echoes of the two calibration TRs. For simplicity, the index, j, will be omitted from the expressions. Let $s_1(t)$ and $s_2(t)$ be the received signal for jth echoes of the 1st and 2nd calibration TRs respectively. With the error sources listed above, these signals can be written as follows:

$$s_1(t) = \int m(x,y,z)\, e^{-i[2\pi(k_x(t+t_d)+k_p)x+\phi_e(x,t)+\phi_f(x,y,z,t)]} * H(t)\, dx\, dy\, dz \qquad (A.1)$$

$$s_2(t) = \int m(x,y,z)\, e^{-i[2\pi(-k_x(-t+t_d)-k_p)x-\phi_e(x,-t)+\phi_f(x,y,z,-t)]} * H(-t)\, dx\, dy\, dz \qquad (A.2)$$

where '$*$' denotes convolution,

t_d = delay between data acquisition and G_x waveform,

k_p = error in prewinder area,

$\phi_e(x,t)$ = phase due to eddy currents,

$\phi_f(x,y,z,t)$ = phase due to off resonance,

$H(t)$ = impulse response of data-acquisition filter,

$$k_x(t) = \frac{\gamma}{2\pi} \int G_x(t)\, dt, \qquad (A.3)$$

and $s_2(t)$ has already been time-reversed.

We now make the following assumptions:

(a) The delay between data acquisition and G_x waveform produces only a k_x shift, k_d. This is true if data is acquired with a constant value for G_x. From this assumption, it follows that $k_x(t+t_d) = k_x(t) + k_d$ and $k_x(-t+t_d) = k_x(t) - k_d$. While this can be shown rigorously, it is easier to consider Fig. A.1 which shows that a delay between data acquisition and G_x waveform will move the gradient echo to the left of the center of the data-acquisition window in s_1 and to the right the center of the data-acquisition window in s_2.

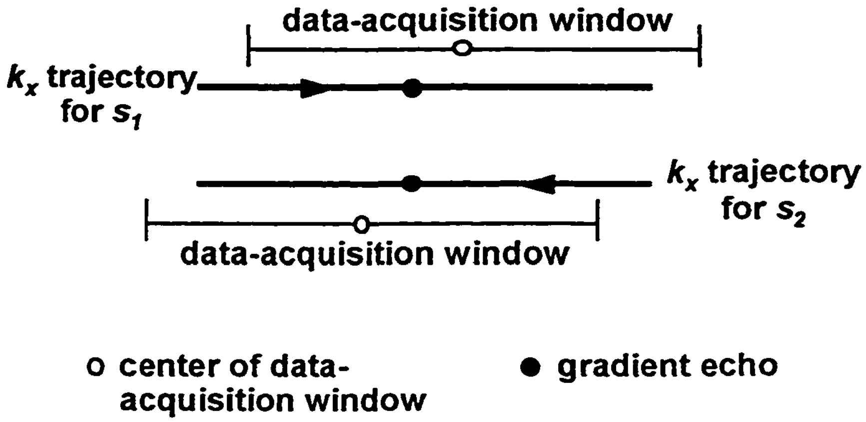

Figure A.1: Effect of a delay between the data-acquisition window and the G_x waveform.

(b) The eddy-current effects produce only a k_x shift, k_e, and a phase error, e_0. This is true if we consider only one k_x location, in particular, k_x=0. From this assumption, it follows that $\o_e(x,t) = 2\pi k_e x + e_0$ and $-\o_e(x,-t) = -2\pi k_e x - e_0$. While the effects of k_e, can be shown rigorously, it is easier to note that eddy-current effects oppose the actions of G_x, retarding the k_x trajectory. Therefore, they will move the gradient echo to the left the center of the data-acquisition window in s_1 and to the right of the center of the data-acquisition window in s_2.

(c) The off-resonance effects produce only a phase error, r_0. This is true if we consider only one k_x location, in particular, k_x=0.

(d) $H(t)$ is purely real.

With these simplifications, the k-space signal can be written as follows:

$$s_1(t) = \int m(x,y,z)\, e^{-i\left[2\pi\left(k_x(t)+k_d+k_p+k_e\right)x+\left(e_0+r_0\right)\right]} * H(t)\; dx\, dy\, dz, \qquad \text{(A.4)}$$

$$s_2(t) = \int m(x,y,z)\, e^{-i\left[2\pi\left(k_x(t)-k_d-k_p-k_e\right)x+\left(-e_0+r_0\right)\right]} * H(-t)\; dx\, dy\, dz \qquad \text{(A.5)}$$

We now Fourier-transform along k_x to produce data in "p-space", so called because it is a projection space in which the signal has been integrated along y and z. The p-space signals can be written as follows:

$$c_1(x) = c(x)\, e^{-i\left[2\pi\left(k_d+k_p+k_e\right)x+\left(e_0+r_0\right)\right]}\, h(x) \tag{A.6}$$

$$c_2(x) = c(x)\, e^{-i\left[-2\pi\left(k_d+k_p+k_e\right)x+\left(-e_0+r_0\right)\right]}\, h(-x) \tag{A.7}$$

where $c(x)$ is the ideal unfiltered data and $h(x)$ is the inverse Fourier transform of $H(t)$. Since $H(t)$ is real, the magnitude of $h(x)$ is even and the phase of $h(x)$ is odd. Therefore, we can write the p-space signal as follows:

$$c_1(x) = c(x)\, e^{-i\left[2\pi\left(k_d+k_p+k_e\right)x+\left(e_0+r_0\right)\right]}\, \left|h(x)\right|\, e^{i\phi_h(x)} \tag{A.8}$$

$$c_2(x) = c(x)\, e^{-i\left[-2\pi\left(k_d+k_p+k_e\right)x+\left(-e_0+r_0\right)\right]}\, \left|h(x)\right|\, e^{-i\phi_h(x)} \tag{A.9}$$

where $\phi_h(x)$ is the phase of $h(x)$. A phase correction, $f(x)$, can now be derived from the phase of the ratio, $c_2(x)\,/c_1(x)$:

$$\begin{aligned} f(x) &= \frac{\angle\left(c_2(x)/c_1(x)\right)}{2} && \text{(A.10)} \\ &= \left(k_d+k_p+k_e\right)x+e_0+\phi_h(x) && \text{(A.11)} \end{aligned}$$

where the '$\angle$' operation yields the phase. Multiplying $c_1(x)$ by $e^{if(x)}$ yields the desired result:

$$\begin{aligned}\underline{c_1}(x) &= c_1(x)\, e^{if(x)} && \text{(A.12)}\\ &= c_1(x)\, |h(x)|\, e^{-ir_0}. && \text{(A.13)}\end{aligned}$$

We note that, in areas of low SNR, $f(x)$ is unreliable and phase spikes may result, producing artifacts in the image. To avoid these spikes, we approximated $f(x)$ by a cubic polynomial, using a least-squares fit weighted by $|c_1(x)|^2$.

For the inside-out EPI trajectory described in Chapter 3, data is acquired starting from the center of k-space with separate interleaves for the top and bottom halves. When the readout gradient waveforms for the top and bottom halves of k-space have opposite polarities, the top and bottom halves differ by a k_x shift of $2k_p$. Two calibration TRs are required for an estimate of k_p that is distinct from the other k_x shifts.

A.1.2 Unwrapping phase

Great care must be taken in deriving $f(x)$ otherwise there may be discontinuities of π. The exact derivation is as follows:

$$f(x) = \frac{1}{2}\, unwrap\left[\angle\left(c_2(x)\right) - \angle\left(c_1(x)\right)\right] \tag{A.14}$$

where the '$\angle$' operation yields the principal value of the phase and the '*unwrap*' operation removes discontinuities of 2π. Suppose that the phase of c_1 and c_2 has principal values of $\hat{p}_1$ and $\hat{p}_2$ respectively and unwrapped values of p_1 and p_2 respectively:

$$p_1(x) = \hat{p}_1(x) + 2\pi n_1(x) \tag{A.15}$$

$$p_2(x) = \hat{p}_2(x) + 2\pi n_2(x) \tag{A.16}$$

where $n_1(x)$ and $n_2(x)$ are integer-valued. If we divide by 2 before unwrapping, we would get

$$f(x) = \frac{\hat{p}_2(x) - \hat{p}_1(x)}{2} \tag{A.17}$$

$$= \frac{p_2(x) - p_1(x)}{2} - \pi\left(n_2(x) - n_1(x)\right) \tag{A.18}$$

where, in general, the $(n_2(x) - n_1(x))$ term would produce discontinuities of π at several x locations.

A.1.3 Offset adjustment

Because phase unwrapping can insert arbitrary offsets of 2π, it may be necessary to adjust the offset of $f(x)$ by π. Specifically, the following expressions are true for any integer values of m_1 and m_2:

$$e^{ip_1(x)} = e^{i\left(p_1(x)+2\pi m_1\right)} \tag{A.19}$$

$$e^{ip_2(x)} = e^{i\left(p_2(x)+2\pi m_2\right)} \tag{A.20}$$

Therefore, a general expression for $f(x)$ is as follows:

$$f(x) = \frac{\left(p_2(x) + 2\pi m_2\right) - \left(p_1(x) + 2\pi m_1\right)}{2} \tag{A.21}$$

$$= \frac{p_2(x)-p_1(x)}{2} + \pi(m_2-m_1). \tag{A.22}$$

If (m_2-m_1) is odd then $f(x)$ will contain a spurious factor of π. This causes problems if $f(x)$ contains spurious factors of π for some echoes but not for others.

This spurious factor can be removed by observing that the jth corrected calibration echo,

$$\underline{c}_{1,j}(x) = c_{1,j}(x)\, e^{if_j(x)}, \tag{A.23}$$

should have a similar phase to the $(j\text{-}1)$th corrected calibration echo,

$$\underline{c}_{1,j-1}(x) = c_{1,j}(x)\, e^{if_{j-1}(x)}. \tag{A.24}$$

We evaluate the phase difference between $\underline{c}_{1,j}(x)$ and $\underline{c}_{1,j-1}(x)$ by calculating the following quantity:

$$\int \left|c_{1,j}(x)\right| e^{i\angle\left(c_{1,j}(x)/c_{1,j-1}(x)\right)}\, dx. \tag{A.25}$$

This can be viewed as a weighted vector sum or as the Fourier transform of

$$\left|c_{1,j}(x)\right| e^{i\angle\left(c_{1,j}(x)/c_{1,j-1}(x)\right)} \tag{A.26}$$

evaluated at k_x=0. If the phase of this quantity is closer to π or $-\pi$ than to 0, we add π to $f_j(x)$. This assumes that off-resonance or motion does not cause the phase difference between $\underline{c}_{1,j}(x)$ and $\underline{c}_{1,j-1}(x)$ to be greater than $\pi/2$.

A.1.4 Image reconstruction

The image is reconstructed with the following steps: (i) The imaging data is first transformed along k_x only. (ii) The jth echo of each TR is multiplied by the jth phase correction, $e^{if_j(x)}$. (iii) The corrected data is transformed along k_y and k_z. Note that only two calibration TRs are required for each image. That is, if there are N echoes per TR, only N phase corrections are required. It is important to have different phase corrections for different echoes since, for a given gradient lobe, eddy-current effects depend on the cumulative effects of the preceding gradient lobes which may include prewinders, rewinders and crushers. The calibration data acquired with a particular image may be unsuitable if there are areas of low SNR. In this case, calibration data can be used from a phantom acquired with the same imaging parameters.

A.2 RARE ghosts

In GRASE, ghosting can be produced by differences between data acquired during the odd and even spin-echoes, as it is in RARE. The phase errors caused by these differences can be corrected in post processing using calibration data acquired before imaging [109, 122]. These odd-even spin-echo differences also cause k-space shifts. By modifying the EPI correction method described, we correct both k-space shifts and phase errors.

A.2.1 Theory

The differences between data acquired during the odd and even spin-echoes can have several causes: (a) eddy-current effects on the gradients, (b) a delay between the refocusing 180 and the crushers produces unequal crusher areas, (c) the RF subsystem does not faithfully produce a phase difference of $\pi/2$ between the tip-down excitation and the refocusing 180s and (d) the phase-difference between the refocusing 180s and the tip-down excitation is not exactly $\pi/2$ since the composite pulse of Levitt and Freeman converts B_1 inhomogeneity into phase errors in the transverse plane [101]. To correct these differences, we modified the EPI correction method in two ways. As in EPI correction, we assumed that the effects of these differences could be approximated by a phase offset and a k_x offset. First, crushers for the refocusing pulses were placed on G_x. Thereby eddy-current effects on the crushers or a delay between the refocusing 180 and the crushers produce a k_x error which can be measured with the calibration data. Second, in the 2nd calibration TR, all gradient waveforms are negated, including those used for tip-down excitation and refocusing. Additionally, the phase difference between the tip-down excitation and the refocusing 180s is negated to correct errors due to (c) and the RF waveforms for the refocussing 180s are negated to correct errors due to (d). This yields phase and k_x errors which have opposite polarity in the two calibration TRs.

One complication is that the phase and k_x errors are different for the spin echoes and the stimulated echoes. In each 180-180 interval, the received signal consists of three components: the spin echo, odd-order stimulated echoes and even-order stimulated echoes [109]. The odd-order stimulated echoes are produced by magnetization that has been stored on the longitudinal axis for an odd number of 180-180 intervals. Similarly, the even-order stimulated echoes come from magnetization that has been longitudinally stored for an even number of intervals. The phase and k_x errors are the same for the spin echoes and the even-order stimulated echoes. However, they are different for the odd-order stimulated echoes. Fortunately, for the first few 180-180 intervals, the signal from the odd-order stimulated echoes is much smaller than the combined signal of the spin echoes and the even-order stimulated echoes [109]. Since we only use three 180-180 intervals in each TR, the phase and k_x errors are determined mostly by the errors on the spin echoes and the even-order stimulated echoes.

In EPI correction, adjustment of the phase-correction offset is achieved by comparing the phases of the *j*th corrected calibration echo and the *(j-1)*th corrected calibration echo. However, for RARE correction, the refocusing pulse can 'reset' the phase of the corrected calibration data. Therefore, the 1st echo after each refocusing pulse is compared to the 1st echo after the 1st refocusing pulse.

A.2.2 Image reconstruction

Image reconstruction follows the same procedure as that described for reducing EPI ghosting. Therefore, with two calibration TRs, both EPI ghosting and RARE ghosting can be reduced in post-processing.

Appendix B

Partial-Fourier reconstruction for EPI

For all the partial-Fourier images shown (real and simulated; no-flyback EPI, partial-flyback EPI and one-shot bowtie imaging), a "conjugation reconstruction" method was used which follows the MoFIR method introduced by McGibney *et al.* [38]. A phase correction is constructed using the complete low-frequency data. This phase correction is applied before the merging filter. Then the conjugate of the k-space data is added to itself. After a Fourier transform, the positive real part is displayed.

Although we do not show the results, we also reconstructed the EPI images after zero-filling. This produced images with less signal loss than the conjugation reconstruction. However, the signal loss was still worse than for inside-out EPI. Furthermore, zero-filling severely compromised the spatial resolution. The zero-filled partial-Fourier EPI images were obviously more blurry than the inside-out EPI images. In essence, zero-filling reconstruction produces less signal loss than conjugation reconstruction but obliterates the off-resonance advantages of partial-Fourier EPI over inside-out EPI.

The zero-filling reconstruction suffers from spatial blurring since it can be viewed as the application of a rectangular window in *k*-space. The conjugation reconstruction asserts that the k-space data is Hermitian-symmetric. However, phase due to flow and off-resonance, errors in phase estimation and k_y-misalignment compromise this Hermitian symmetry, producing signal loss, blurring and ringing. We note that this algorithm produced negligible artifacts when used to reconstruct one-shot bowtie images because the acceleration-induced phase was not severe.

Appendix C

Sliding readout delays for EPI

Sliding readout delays are used to reduce ghosting due to off-resonance [27, 30] and phase-encode flow. Their locations in the EPI pulse sequences are shown in Figs. 3.11-3.13. Their values are given here. Let

T = time between successive echoes
i = interleaf number
N = total number of interleaves.

For partial-Fourier EPI, we have a single delay which is given by

$$\text{Readout delay} = \left(\frac{i-1}{N}\right)T. \tag{C.1}$$

For partial-flyback partial-Fourier EPI, two readout delays are used. These delays can be expressed as

$$\text{First readout delay} = \left(\frac{i-1}{N}\right)2T, \tag{C.2}$$

$$\text{Second readout delay} = \left(\frac{N-i}{N}\right)T. \tag{C.3}$$

For partial-flyback inside-out EPI, two readout delays are also used. Since half the interleaves are used to cover half of *k*-space, their durations are somewhat different than for partial-flyback partial-Fourier EPI:

$$\text{First readout delay} = \left(\frac{i-1}{N/2}\right)2T, \tag{C.4}$$

$$\text{Second readout delay} = \left(\frac{N/2-i}{N/2}\right)T. \tag{C.5}$$

Appendix D

Effects of the anti-aliasing filter in bowtie imaging

Besides the maximum spacing between *k*-space samples, the field-of-view is also limited by the effects of the anti-aliasing filter. For each spoke in the bowtie trajectory, applying the anti-aliasing filter limits the field-of-view in the direction of that spoke. To understand the effect of applying the filter in different directions, we will first explore a 2DFT imaging example.

Consider two 2DFT images where the readout-gradient axis in the 1st image is perpendicular to the readout-gradient axis in the 2nd image, as shown in Figs. D.1a and D.1c. Suppose the *k*-space sampling density yields a field-of-view of width, W, but the anti-aliasing filter truncates the readout-direction field-of-view to a width of W/2. The direction of field-of-view truncation in the 2nd image is perpendicular to the direction of field-of-view truncation in the 1st image.

Now suppose we make an image by filling the bottom half of the 1st image's *k*-space rectangle with data from the 2nd image, as shown in Fig. D.1e. There are now three regions in *x*-*y* space, as shown in Fig. D.1f. The first region is the intersection of the fields-of-view of Figs. D.1b and D.1d. It is referred to as the 'intersection FOV' and is shown as the darker shaded area in Fig. D.1f. Signal in the intersection FOV represents spins which were within the filter bandwidth for both the top and bottom halves of *k*-space. The second region is the union of the fields-of-view of Figs. D.1b and D.1d. It is referred to as the 'union FOV' and consists of the lighter and the darker shaded areas in Fig. D.1f. Signal in the lighter shaded area (inside the union FOV but outside the intersection FOV) represents spins which were within the filter bandwidth for only one half of *k*-space. This signal comes from an incomplete set of *k*-space data and has lower resolution. The third region is entirely outside the union FOV; it contributes no signal to the final image.

The anti-aliasing filter has similar effects in bowtie imaging.

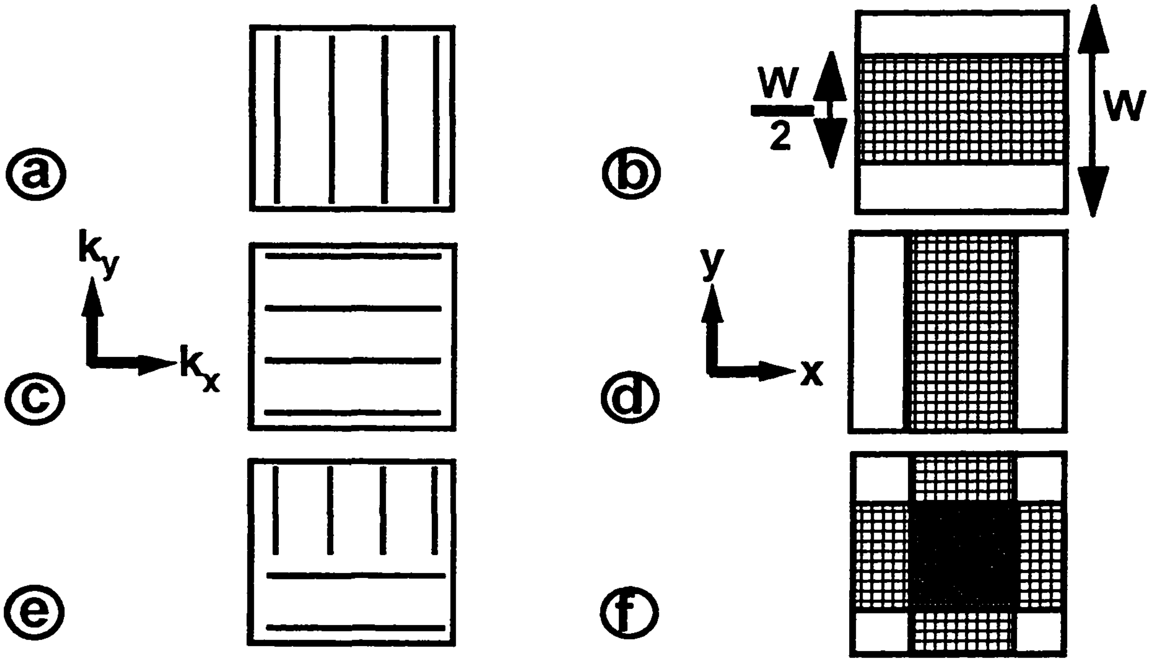

Figure D.1: Anti-aliasing filter effects on the 2DFT-imaging FOV. (a) and (c) k_x-k_y space: vertical or horizontal readout axes. (b) and (d) x-y space: FOV truncated vertically or horizontally. (e) k_x-k_y space with data from (a) and (c). (f) x-y space: the darker shaded area is the intersection of the FOVs; the lighter shaded area plus the darker shaded area is the union of the FOVs; only the intersection of the FOVs contains full-resolution signal.

Figure 4.4a shows a version of the k_x-k_v trajectory of Fig. 4.1 where each spoke has been approximated by a straight line and only the left-to-right spokes are shown, labelled 1 to 3. For each spoke, applying the anti-aliasing filter limits the field-of-view in the direction of that spoke. In Fig. 4.4b, the lines bounding the field-of-view of each spoke are labelled with that spoke's number. The resulting intersection FOV is shown as the darker shaded area and the union FOV consists of the lighter and darker shaded areas. Only signal in the intersection FOV is from spins which were within the filter bandwidth for the entire data-acquisition period.

The shape of the intersection FOV in Fig. 4.4b has the following physical interpretation. Each spoke acquires data from the same spatial region whose width, FOV_x, is determined by the filter bandwidth. However, a spin with non-zero velocity can enter or exit this spatial region during the data-acquisition period. Therefore, this spin is not seen by all of the spokes and it will yield an incomplete set of k-space data. Consider a spin which was at the left x-edge of the kite at t=0. For this spin to remain within FOV_x for the entire data-acquisition period, t_{DAQ}, it must have $0 \leq v \leq FOV_x/t_{DAQ}$. Now consider a spin which was at the right x-edge of the kite at t=0. For this spin to remain within FOV_x for the entire data-acquisition period, it must have $(-FOV_x/t_{DAQ}) \leq v \leq 0$. Similar arguments can be made for other x locations. Therefore, if Δx and Δv are the dimensions of the kite as labelled in Fig. 4.4b, we can write $\Delta x = FOV_x$ and $\Delta v = FOV_x/t_{DAQ}$.

This analysis of anti-aliasing filter effects applies to both one-shot and two-shot imaging. For one-shot imaging, the partial-Fourier reconstruction synthesizes the missing data by conjugating the acquired data: reflecting it about the k_x and k_y axes. Therefore, the union and intersection FOVs of the conjugated data are reflected about the x and v axes. Fortuitously, these reflected FOVs are the same as for the acquired data. In two-shot imaging, the *k*-space trajectory for the 2nd shot is the conjugate of the *k*-space trajectory for the 1st shot. Therefore, both shots have the same union and intersection FOVs.

Until now, we have assumed a constant gradient amplitude. However, bowtie imaging uses a time-variant gradient and the effects of the filter depend on this time variance. Let us define the time-width of the filter as the product of the sampling period and the number of filter taps. When the gradient amplitude varies slowly compared to the time-width of the filter, we can approximately say that the widths of the intersection and union FOVs are inversely proportional to the gradient amplitude. We can then define the intersection FOV as the intersection FOV produced by the largest gradient amplitude during the data-acquisition window.

In summary, for any *k*-space trajectory whatsoever, the field-of-view can be limited by the anti-aliasing filter since only signal in the intersection FOV comes from a complete set of *k*-space data. If the object being imaged is smaller than the intersection FOV then the effects of the anti-aliasing filter are irrelevant and the field-of-view is limited by the *k*-space sampling density. However, if the object being imaged is larger than the intersection FOV then the field-of-view is limited to the intersection FOV and the *k*-space sampling density should be large enough to prevent aliasing in this intersection FOV.

Appendix E

Effects of off-resonance on moving spins

For a constant velocity, *v*, and motion only along one dimension, *x*, assume that the off-resonance, *f*, can be expressed as a function of *x* as follows:

$$f(x)=\sum_{j=0}^{n}a_jx^j. \tag{E.1}$$

Now let x_0 be the value of *x* at $t=0$ such that

$$x(t)=x_o+vt. \tag{E.2}$$

Using Eq. E.2 in Eq. E.1 leads to

$$f(t)=\sum_{j=0}^{n}a_j(x_o+vt)^j. \tag{E.3}$$

The phase due to off-resonance evolves with time as given by

$$\varphi(t) = \int_{t_s}^{t} f(t)\, dt \,. \qquad \text{(E.4)}$$

Using Eq. E.3, we get

$$\varphi(t) = \int_{t_s}^{t} \sum_{j=0}^{n} \mathrm{a}_{\mathrm{j}} (x_o + vt)^j \, dt \,. \qquad \text{(E.5)}$$

Interchanging the order of summation and integration leads to

$$\varphi(t) = \sum_{j=0}^{n} \left[\frac{\mathrm{a}_{\mathrm{j}}}{(\mathrm{j}+1)\mathrm{v}} (x_o + vt)^{j+1} \right]_{\mathrm{t_s}}^{\mathrm{t}} \qquad \text{(E.6)}$$

$$= \sum_{j=0}^{n} \frac{\mathrm{a}_{\mathrm{j}}}{(\mathrm{j}+1)\mathrm{v}} \left[(x_o + vt)^{j+1} - (x_o + vt_s)^{j+1} \right]. \qquad \text{(E.7)}$$

Evaluating Eq. E.6 for each value of *j*:

$$\begin{aligned}
&\varphi(t) = \\
&\frac{\mathrm{a_o}}{\mathrm{v}}\left[v(t - t_s) \right] \; + \\
&\frac{\mathrm{a_1}}{2\mathrm{v}}\left[v(t - t_s)(2\mathrm{x_o}) + v^2(t^2 - t_s^2) \right] \; + \\
&\frac{\mathrm{a_2}}{3\mathrm{v}}\left[v(t - t_s)(3\mathrm{x}_o^2) + v^2(t^2 - t_s^2)(3x_o) + v^3(t^3 - t_s^3) \right] \; + \\
&\frac{\mathrm{a_3}}{4\mathrm{v}}\left[v(t - t_s)(4\mathrm{x}_o^3) + v^2(t^2 - t_s^2)(6x_o^2) + v^3(t^3 - t_s^3)(4x_o) + v^4(t^4 - t_s^4) \right] \; + \; \ldots \qquad \text{(E.8)}
\end{aligned}$$

Adding up the columns in Eq. E.8 leads to

$$\varphi(t)$$

$$= (t-t_s)\sum_{j=0}^{n} \mathrm{a}_\mathrm{j} x^j + v(t^2-t_s^2)\sum_{j=1}^{n} \frac{\mathrm{j}\mathrm{a}_\mathrm{j}}{2} x^{j-1} + v^2(t^3-t_s^3)\sum_{j=2}^{n} \frac{\mathrm{j}(\mathrm{j}-1)\mathrm{a}_\mathrm{j}}{2\cdot 3} x^{j-2} + \dots \tag{E.9}$$

$$= (t-t_s)f(x) + \frac{v(t^2-t_s^2)}{2!}\frac{df}{dx} + \frac{v^2(t^3-t_s^3)}{3!}\frac{d^2 f}{dx^2} + \dots \tag{E.10}$$

Therefore, when *v* is zero or *f* is constant, we get the phase evolution seen by *x*-*y* images. However, for non-zero *v* and spatially-variant *f*, the motion of a particular spin means that it sees a time-variant resonant frequency.

Appendix F

Designing the readout-gradient waveform in bowtie-imaging

In bowtie imaging, the design of the readout-gradient waveform has three stages: (i) choosing a bowtie, (ii) choosing a rectangular region of that bowtie, and (iii) centering the rectangular region at the k-space origin. These stages are described in this appendix.

F.1 Choosing a bowtie

The parameters that define a bowtie are:

N_{lobes} = number of lobes in the G_x waveform
$k_{x,lobe}$ = area of each lobe
FOV_x = spatial field-of-view

With $k_{x,lobe}$ and FOV_x fixed, a larger N_{lobes} produces a larger k_v width but a longer data-acquisition time. This means better velocity resolution but poorer temporal resolution and also, because of the time-of-flight effects described by Eqs. 4.7-4.8, possibly a smaller velocity field-of-view.

With N_{lobes} and FOV_x fixed, a larger $k_{x,lobe}$ produces larger k_x and k_v widths but larger spacing between the spokes and a longer data-acquisition time. This provides better spatial- and velocity-resolution but a smaller velocity field-of-view and poorer temporal resolution.

FOV_x is relevant only in the following situation. Consider the following equation:

$$f_s = \gamma G_{x,\max}\, FOV_x \tag{F.1}$$

where f_s is the sampling frequency, γ is the gyromagnetic ratio and $G_{x,max}$ is the maximum amplitude of G_x sawtooth. It is possible that FOV_x is so large that the required sampling frequency exceeds the maximum available sampling frequency. In this case, it would be necessary to reduce $G_{x,max}$ which, for a given $k_{x,lobe}$ and N_{lobes}, increases the duration of the G_x sawtooth.

Now that we have chosen our bowtie, the k-space origin is currently at one corner of the bowtie. We will now choose a rectangular region of the bowtie. Then we will move the bowtie so that the k-space origin is at the center of the rectangle.

F.2 Choosing a rectangle

For a given bowtie, many rectangles can be drawn. Here are the parameters that define a rectangle:

$k_{x,rect} = k_x$ width
$k_{v,rect} = k_v$ width
$k_{xo} = k_x$ location of the center
$k_{xo} = k_v$ location of the center

We can reduce the number of parameters from 4 to 2 by assuming that, for a given k_{xo} and k_{vo}, we draw the largest rectangle possible. This largest possible rectangle is defined as follows, with reference to Fig. F.1. First, note that a rectangle can only encompass one 'wing' of the bowtie. Therefore, assume that the rectangle is placed in the left wing. Now, given k_{xo} and k_{vo}, the largest possible rectangle has its left edge touching the left edge of the bowtie and its bottom-right corner touching the bottom-most spoke of the bowtie. For example, in Fig. F.1a, the point '1' is the center of the taller, thinner rectangle while the point '2' is the center of the shorter, wider rectangle. Therefore, choosing k_{xo} and k_{vo} specifies $k_{x,rect}$ and $k_{v,rect}$ and the rectangle can be described using only k_{xo} and k_{vo}.

When k_{vo} is fixed, choosing k_{xo} involves a tradeoff between spatial resolution and velocity resolution. Figure F.1a illustrates this tradeoff with two rectangles centered at k_{vo}=0. Compared to the rectangle centered at point 1, the rectangle centered at point 2 has a larger k_{xo} and hence a larger $k_{x,rect}$. However, it has a smaller $k_{v,rect}$.

When k_{xo} is fixed in two-shot imaging, k_{vo}=0 is a natural choice. Since it provides the maximum $k_{v,rect}$, there is no advantage in using any other

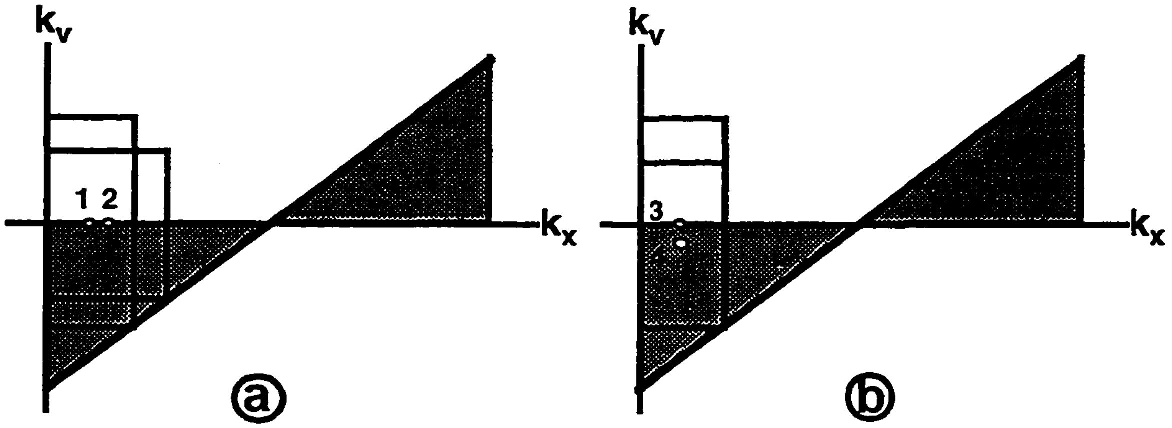

Figure F.1: Choosing a k-space rectangle. (a) k_v-position of the rectangle's center is fixed. Point '1' is the center of the taller rectangle. Point '2' is the center of the wider rectangle. (b) k_x-position of the rectangle's center is fixed. Point '3' is the center of the taller rectangle. Point '4' is the center of the shorter rectangle. (After the rectangle is chosen, the entire bowtie will be moved so that the rectangle's center is at the k-space origin.)

value of k_{vo}. However, when k_{xo} is fixed in one-shot imaging, choosing k_{xo} involves a tradeoff between velocity resolution and what fraction of k-space is acquired. Figure F.1b illustrates this tradeoff, showing two rectangles with the same k_{xo}. The point '3' is the center of the taller rectangle while the point '4' is the center of the shorter rectangle. The rectangle centered at point 3 has a larger $k_{v,rect}$ but only acquires 50% of k-space. The rectangle centered at point 4 has a smaller $k_{v,rect}$ but acquires a larger fraction of k-space, producing a more accurate partial-Fourier reconstruction.

We have chosen a rectangular region of the bowtie but the k-space origin is still at one corner of the bowtie. We will now move the bowtie so that the k-space origin is at the center of the rectangle.

F.3 Centering the rectangle

For one-shot imaging, to center the rectangle at the *k*-space origin, we need a prewinder with zeroth moment equal to $-k_{x,rect}$ and first moment equal to $-k_{v,rect}$. For two-shot imaging, $k_{v,rect}$ is zero and we can use a unipolar prewinder if we ignore its first moment. This is reasonable if we choose the time origin, $t=0$, to be near the center of the prewinder. For one-shot imaging, $k_{v,rect}$ is non-zero and we need a bipolar prewinder. When this prewinder lobe has been prepended to the G_x sawtooth waveform, the design process is complete.

Appendix G

Inversion timing for flow and fat suppression

This appendix discusses how the inversion timing affects flow suppression, the avoidance of vessel-wall motion and fat suppression. This inversion timing is embodied in three variables: (a) TD, the delay between the EKG trigger and the effective center of the first flow-inversion pulse, (b) TI_{flow}, the delay between the effective centers of the first flow-inversion and the rectangular tip-down pulse, and (c) TI_{fat}, the delay between the effective centers of the fat-inversion pulse and the rectangular tip-down pulse. We set TD and TI_{flow} to (i) optimize the T_1-nulling of blood, (ii) maximize outflow and (iii) acquire data during a period of slow flow, thereby avoiding artifacts caused by blood-vessel-wall motion. We set TI_{fat} to optimize the T_1-nulling of fat.

G.1 T_1-nulling of blood

We want to estimate a value for TI_{flow} assuming a constant heart rate and three refocusing 180s per TR. Let M_b be the steady-state longitudinal magnetization of upstream blood just before the 1st-flow inversion and M_0 be the equilibrium magnetization. To calculated the value of M_b, there are two scenarios which must be considered: (i) the upstream blood is affected by the all of the preceding 1st-flow inversions and all of the preceding refocusing 180s, and (ii) the upstream blood is affected by the all of the preceding 1st-flow inversions, all of the preceding refocusing 180s and the most recent tip-down pulse. Fortunately, the values of TI_{flow} are approximately equal for the two scenarios.

For the 1st scenario, it can be shown that M_b is given as follows:

$$\left(1-e^{-TR/T_1}\right)M_b = \\ M_0\left[\left(1+e^{-TR/T_1}\right)+2e^{-(TR-TI_{flow}-\frac{5}{2}TE)/T_1}\left(1-e^{-TE/T_1}+e^{-2TE/T_1}\right)\right]. \qquad (G.1)$$

It can also be shown that the optimal value of TI_{flow} is given as follows:

$$TI_{flow} = T_1 \ln\left(1+\frac{M_b}{M_0}\right). \qquad (G.2)$$

For TE << T_1, we can combine Eqs. G.1 and G.2 to obtain the following approximate value for TI_{flow}:

$$TI_{flow} = T_1 \ln\left(\frac{2}{1+e^{-TR/T_1}}\right). \qquad (G.3)$$

For the 2nd scenario, it can be shown that M_b is given as follows:

$$M_b = \\ M_0\left[1-e^{TI_{flow}/T_1}e^{-(TR-\frac{5}{2}TE)/T_1}\left(2-2e^{-TE/T_1}+2e^{-2TE/T_1}-e^{-\frac{5}{2}TE/T_1}\right)\right]. \qquad (G.4)$$

For TE << T_1, it can be shown that combining Eqs. G.4 and G.2 will yield Eq. G.3. If the delay between the tip-down pulse and the final refocusing 180 is much less than TR then M_b does not depend strongly on the number of refocusing 180s. Nor does it depend strongly on whether the upstream blood has been affected by any tip-down pulses.

Let us assume a blood T_1 of 1000 ms [112] and a TE of 30 ms and let RR be the delay between R-waves. For heart rates between 50 and 90 bpm, Fig. G.1a shows the the optimal values of TI_{flow}. For TR = 1xRR, we typically used TI_{flow} = 300 ms and, for TR = 2xRR, we typically used TI_{flow} = 420 ms. We will now consider whether these typical values of TI_{flow} allow sufficient outflow and data acquisition during slow flow.

G.2 Maximizing outflow

We want all non-inverted blood to flow out of the FOV and be replaced by inverted blood. Let FOV_{flow} = (FOV in the flow direction), and d_{flow} = (distance travelled during TI_{flow}). Flow can be suppressed by making $FOV_{flow} < d_{flow}$. For flow that does not recirculate within the FOV or re-enter it, d_{flow} can be estimated as the area under the velocity-time curve during TI_{flow}.

Unfortunately, there is recirculating flow in the carotid bifurcation [123]. Most flow is non-recirculating and typically exits the bifurcation within one cardiac cycle. However, some spins are swept into a recirculation region in the bulb, where they can remain for several cardiac cycles. This recirculation region briefly collapses with the sudden velocity increase during systole, flushing many, but not all, of the recirculating spins [123].

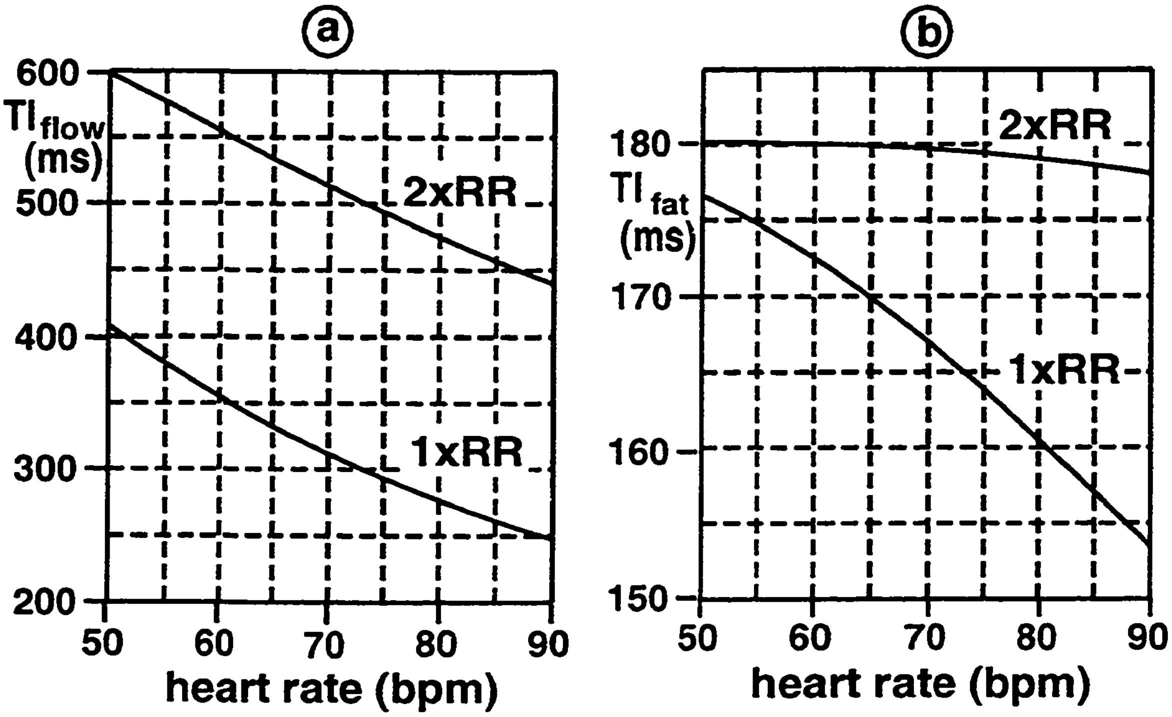

Figure G.1: Inversion-nulling times vs. heart rate for (a) the first flow inversion and (b) the fat inversion. Values are given for a blood T_1 of 1000 ms, a fat T_1 of 260 ms and TR = 1xRR and TR = 2xRR where RR is the interval between R-waves.

Therefore, most of the recirculating flow can be suppressed by placing the first flow inversion before the collapse of the recirculation zone. In lieu of a velocity-time measurement for each volunteer or patient, we used TD = 0. Given that the TI_{flow} delay contains the period of systolic flow, we will now show that choosing TI_{flow} = 300 ms for inversion-nulling of blood is also suitable for suppressing the non-recirculating flow. The velocity-time waveforms in Vanninen *et al.* [124] and Fürst *et al.* [20] suggest that d_{flow} is about 6 cm or more in all but the most severely-stenosed internal carotid artery. Since a 6-cm FOV is adequate to survey the carotid bifurcation, TI_{flow} = 300 ms is quite adquate for suppressing the non-recirculating flow.

Now we will consider whether these values of TD and TI_{flow} will allow data acquisition during slow flow.

G.3 Acquiring data during slow flow

In the carotid arteries, the period of slowest flow occurs around the time of the P-wave which precedes the R-wave by about 100 ms [125]. While the optimal values of TI_{flow} do not allow data acquisition during the P-wave, they are certainly long enough to avoid data acquisition during fast flow.

G.4 T_1-nulling of fat

We want to estimate a value for TI_{fat} given a constant heart rate. Let M_f be the steady-state longitudinal magnetization of fat just before the fat-inversion pulse. To calculate the value of M_f, we assumed that the fat is affected by all of the preceding fat-inversion pulses, all of the preceding refocusing 180s and the most recent tip-down pulse. This is similar to the 2nd scenario used to calculate TI_{flow}. Therefore, M_f is given by an equation that is similar to Eq. G.4:

$$M_f = M_0\left[1 - e^{TI_{fat}/T_1} e^{-(TR-\frac{5}{2}TE)/T_1}\left(2 - 2e^{-TE/T_1} + 2e^{-2TE/T_1} - e^{-\frac{5}{2}TE/T_1}\right)\right]. \quad \text{(G.5)}$$

As with the blood-nulling and GRASE vs. RARE SNR calculations, M_f does not depend strongly on the number of refocusing 180s if the delay between the tip-down pulse and the final refocusing 180 is much less than TR. The optimal value of TI_{fat} is given by an equation that is similar to Eq. G.2:

$$TI_{fat} = T_1 \ln\left(1 + \frac{M_f}{M_0}\right). \tag{G.6}$$

Let us assume a fat T_1 of 260 ms [112] and a TE of 30 ms and let RR be the delay between R-waves. For heart rates between 50 and 90 bpm, Fig. G.1b shows the the optimal values of TI_{fat}. For TR = 1xRR, we typically used TI_{fat} = 170 ms and, for TR = 2xRR, we typically used TI_{fat} = 180 ms.

Appendix H

GRASE vs. RARE scan time

Multi-slice 2D RARE uses more refocusing and excitation pulses than 3D GRASE to acquire the same region of *k*-space. We will now quantify the ratio of GRASE scan time to RARE scan time by considering the duty cycle,

$$DC = (\text{data-acquisition time})/(\text{total time}). \tag{H.1}$$

Let us define the following:

A = time for one gradient-echo lobe,
N = no. gradient echoes per spin echo,
R = time for refocusing 180,
C = time for one crusher,
P = time for G_y blips in GRASE (a G_y blip coincides with each transition of the G_x sawtooth)
S = time for sliding readout delay in GRASE,

The time for phase-encoding prewinders and rewinders can be ignored since these pulses overlap with the crushers. Since data acquired during the G_y blips is not used, the data-acquisition time per gradient-echo is *(A-P)*. The duty cycles for RARE and GRASE are as follows:

$$DC_{RARE} = \frac{(A-P)}{(R+2C)+(A-P)} \tag{H.2}$$

$$DC_{GRASE} = \frac{N(A-P)}{R+2C+NA+S} \tag{H.3}$$

$$= \frac{(A-P)}{\left(\frac{R+2C+S}{N}+P\right)+(A-P)} \tag{H.4}$$

While the numerators are identical, the denominators consist of dead time plus data-acquisition time. GRASE can be more efficient when it amortizes the dead time among many gradient echoes. The ratio of duty cycles is as follows:

$$\frac{DC_{GRASE}}{DC_{RARE}} = \frac{(R+2C)+(A-P)}{\left(\frac{R+2C+S}{N}+P\right)+(A-P)} \tag{H.5}$$

The above duty-cycle ratio contains these assumptions: (i) The crusher areas are the same for 3D GRASE and multi-slice 2D RARE since their voxel dimensions are the same. (ii) Multi-slice 2D RARE acquires the same FOV as 3D GRASE, for example, by using its refocusing pulses to restrict the FOV in the *y* direction [99, 100]. (iii) The dead time between the tip-down pulse and the first refocusing 180 can be ignored. (iv) The duration of the refocusing 180s is the same for multi-slice 2D RARE and 3D GRASE.

Appendix I

Future work in echo-planar imaging

This appendix describes some work on echo-planar imaging (EPI) which was not fruitful. I hope that it may provoke further development or at least provide signposts for dead ends and blind alleys. The impact of higher-performance gradients on EPI was discussed in Section 3.10.3.

I.1 Non-blipped EPI

In considering modifications of EPI, I first concluded that blipped EPI was better than non-blipped EPI because it sampled *k*-space more uniformly. As with all of the trajectories in Chapter 3, for the blipped EPI shown in Fig. I.1a, the G_y gradient is applied in short burts or "blips." For the non-blipped EPI shown in Fig. I.1b, the G_y gradient is continuously active during data acquisition. For the same number of k_x oscillations, the sampling density is lower for non-blipped EPI, for example, at $k_x = 0$ and at the left and right edges of *k*-space. Furthermore, non-blipped EPI can have twice as many ghosts as blipped EPI. In non-blipped EPI, there are two sets of parallel lines

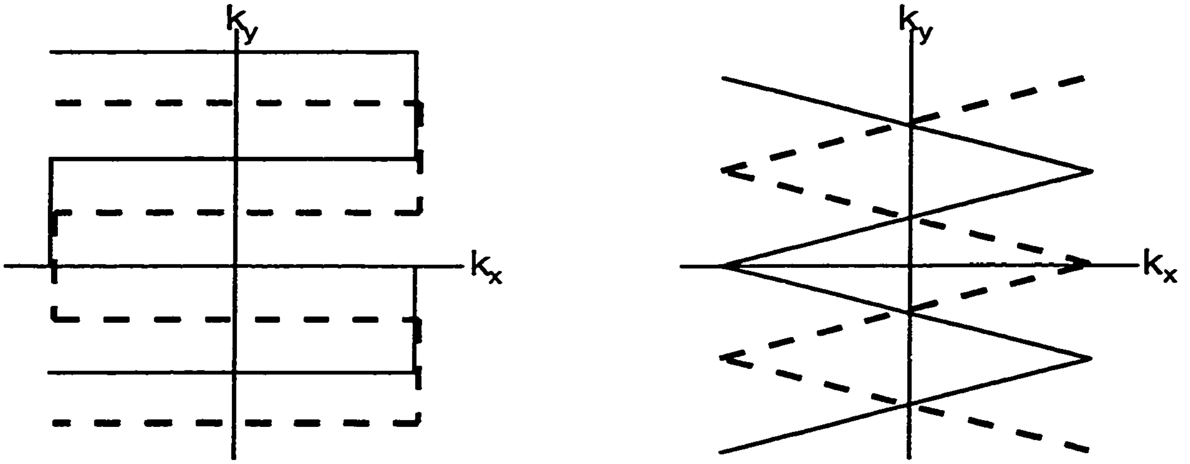

Figure I.1: Comparing (a) blipped EPI and (b) non-blipped EPI. For each trajectory, the first interleaf is shown as a solid line while the second interleaf is shown as a dashed line. For the same number of k_x oscillations, the sampling density is lower for non-blipped EPI.

in k-space; for each set, differences between data acquired during the positive and negative G_x lobes will cause ghosts. Blipped EPI has only one set of parallel lines.

I.2 Modifying blipped EPI for better readout-flow properties

Now restricted to modifications of blipped EPI, I tried to generalize the definition of blipped EPI, deciding on the following: It is any trajectory which acquires data only in the k_x direction, such that the anti-aliasing filter can be used to restrict the field-of-view in the x direction. This meant that I would modify blipped EPI by changing the order of the phase-encoding.

In searching for a blipped-EPI trajectory with better readout-flow properties, I found it useful to consider plots of k_u, the first moment of the readout gradient, versus k_y, the the zeroth moment of the phase-encode gradient. Such plots are shown in Fig. 3.4 and k_y and k_u are given by Eqs. 3.3-3.4. As explained in Section 3.4.1, while k_u varies with both k_x and k_y,

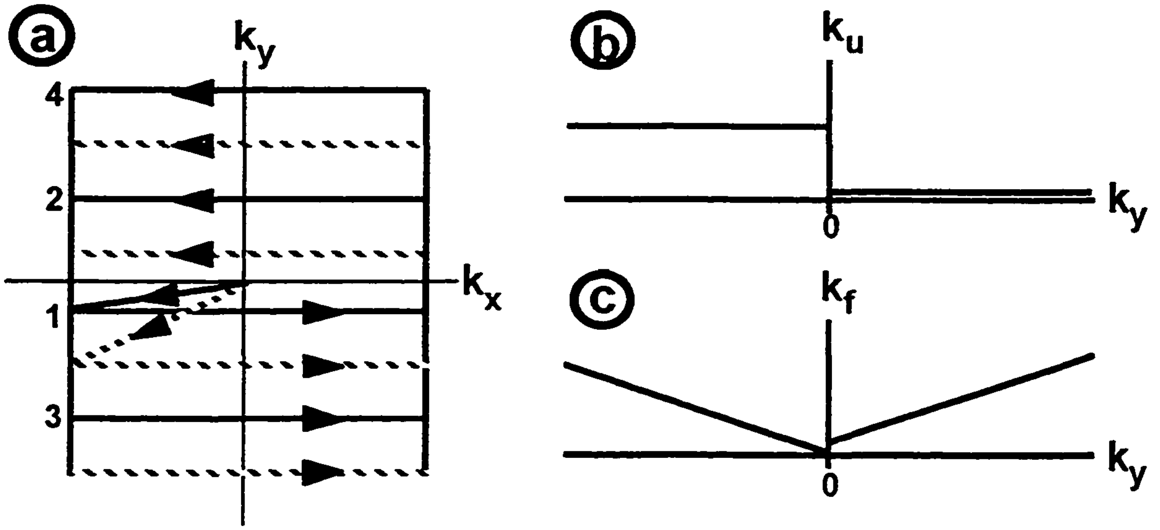

Figure I.2: Retracing square spiral: (a) k_x-k_y trajectory with first interleaf shown as a solid line and second interleaf shown as a dotted line. The phase-encode order for the first interleaf is denoted by the number to the left of each line. (b) k_u vs. k_y for k_x=0. (c) k_f vs. k_y for k_x=0.

the k_x variation is negligible compared to the k_y variation since the time to travel from top to bottom in k-space is much longer than the time to travel from left to right.

For these plots of k_u vs. k_y, I noted the following:

1. Periodicities of k_u produce ghosting in the image.
2. Discontinuities of k_u produce ringing in the image, particularly discontinuities near $k_y = 0$.
3. The non-zero values of k_u produce signal loss when there is a range of velocities in one voxel, particularly the non-zero values near $k_y = 0$.
4. The non-zero values of k_u produce ghosting when there are TR-to-TR variations in velocity.
5. For partial-Fourier trajectories, the reconstruction described in Appendix B is best accomodated by a k_u plot which is conjugate-symmetric.

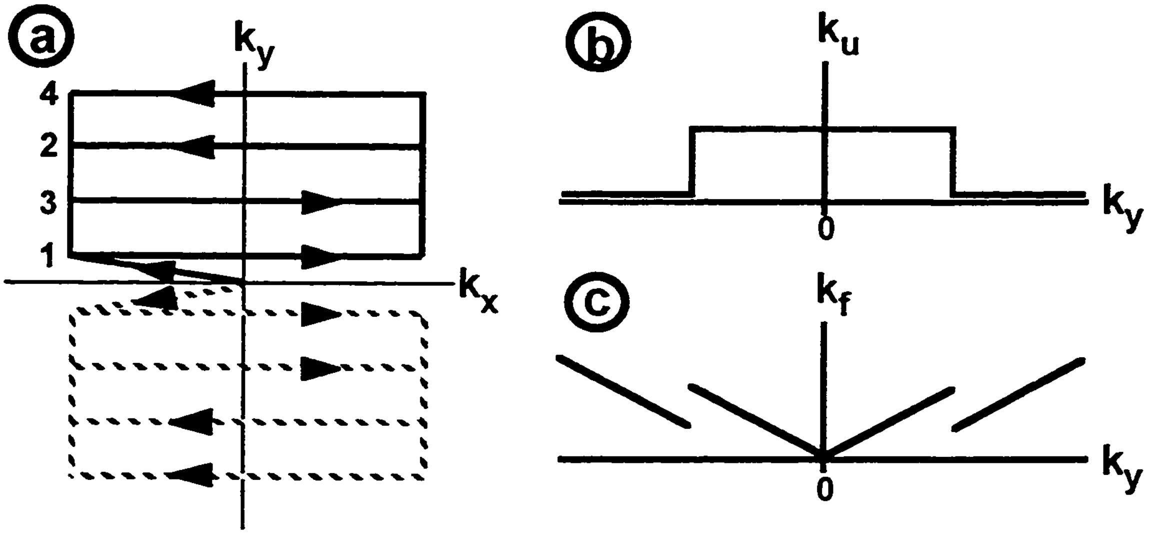

Figure I.3: Shifted retracing square spiral: (a) k_x-k_y trajectory with first interleaf shown as a solid line and second interleaf shown as a dotted line. The phase-encode order for the first interleaf is denoted by the number to the left of each line. (b) k_u vs. k_y for k_x=0. (c) k_f vs. k_y for k_x=0.

One intriguing trajectory is the "retracing square spiral" shown in Fig. I.2a. It is based on the square spiral [126] and the phase-encode order for the first interleaf is denoted by the number to the left of each line. Its k_u-k_y plot, sketched in Fig. I.2b, shows no periodicity and therefore readout flow will not produce ghosting. However, the discontinuity at k_y = 0 results in severe ringing. This discontinuity can be removed by a cyclic shift of the k_u-k_y plot producing the trajectory shown in Fig. I.3a where, again, the phase-encode order for the first interleaf is denoted by the number to the left of each line. However, off-resonance will now produce ghosts because of the discontinuities in k_f vs. k_y shown in Fig. I.3c. Furthermore, blip times are now longer.

In summary, readout-flow properties can be improved by re-ordering the phase encodes but the effects on off-resonance properties, phase-encode-flow properties and gradient duration must be checked.

Figure I.4: Obtaining a field map in partial-flyback inside-out EPI: (a) image of a flow phantom and (b) field map obtained by subtracting the negative-lobe data from the positive-lobe data in the flyback region is corrupted by phase-contrast data.

I.3 Using dead time in partial-flyback EPI

For the partial-flyback EPI trajectory described in Chapter 3, one drawback is that no data is acquired for half the time spent in the flyback region. One intiguing use for this time is to acquire a field map since consecutive negative and positive G_x lobes trace the same line in k_x-k_y space but at different TEs. Unfortunately, since these two lobes do not trace the same line in k_u-k_y space, the phase difference between these two sets of data is produced not only by off-resonance but also by readout flow. That is, the field map can be corrupted by a phase-contrast image as shown in Fig. I.4b.

I attempted to separate the field-map data and the phase-contrast data in the following way. In the flyback region, let us denote the positive-lobe data as the primary image and the negative-lobe data as the auxiliary image. As shown in Fig. I.5, the auxiliary image can be acquired before or after the primary image by altering the G_y-blip waveform. By acquiring the auxiliary image before the primary image in the top half of *k*-space and the auxiliary image after in the bottom half, we get the following equations. Let Ø_{pri} be the phase of the primary image and Ø_{aux} be the phase of the auxiliary image. In the top half of *k*-space, we have

$$\text{Ø}_{\text{top}} = \text{Ø}_{\text{pri}} - \text{Ø}_{\text{aux}} = \text{(field-map data)} + \text{(phase-contrast data)} \qquad \text{(I.1)}$$

and in the bottom half, we have

$$\text{Ø}_{\text{bot}} = \text{Ø}_{\text{aux}} - \text{Ø}_{\text{pri}} = \text{(field-map data)} - \text{(phase-contrast data).} \qquad \text{(I.2)}$$

We can then isolate the field-map data and the phase-contrast data in the following way:

$$(\text{Ø}_{\text{top}} + \text{Ø}_{\text{bot}})/2 = \text{field-map data,} \qquad \text{(I.3)}$$

$$(\text{Ø}_{\text{top}} - \text{Ø}_{\text{bot}})/2 = \text{phase-contrast data.} \qquad \text{(I.4)}$$

Unfortunately, since Ø_{top} and Ø_{bot} are derived from partial-Fourier data, there is blurring and other artifacts in the resultant field map and phase-contrast

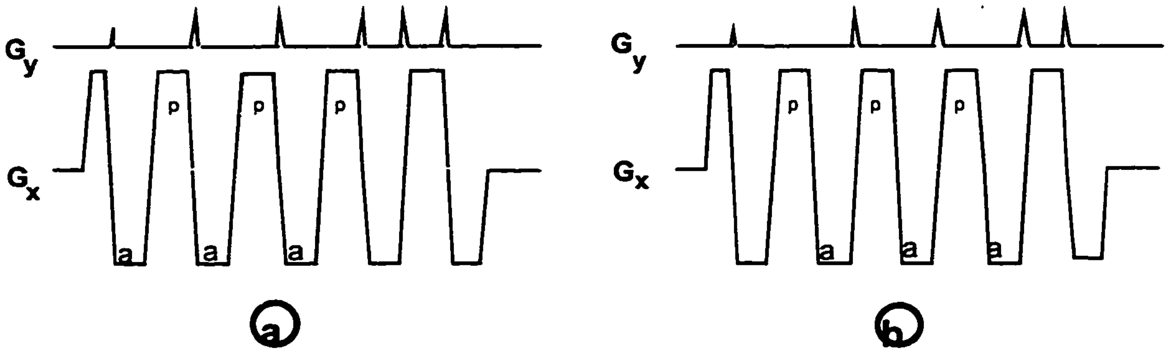

Figure I.5: Interchanging the order of the primary image, denoted as 'p,' and the auxiliary image, denoted as 'a,' in partial-flyback EPI: (a) auxiliary image obtained before primary image, (b) primary image obtained before auxiliary image.

Fig. I.6: Manipulating the primary and auxiliary images in partial-flyback EPI to obtain: (a) a field map and (b) a phase-contrast image.

image, as shown in Fig. I.6.

In summary, I was unsuccessful in using the dead time in partial-flyback EPI to obtain a field map or a phase-contrast image but these may be intriguing possibilities. Another possible use of the dead time is obtaining navigator projections or even a navigator image.

Appendix J

Future work in motion imaging

This appendix describes some work on velocity and motion imaging which was not fruitful. As with Appendix I, I hope that it may provoke further development or at least provide signposts for dead ends and blind alleys. The impact of higher-performance gradients on bowtie imaging was discussed in Section 4.5.6.

J.1 Using a greater portion of the bowtie trajectory

In bowtie imaging, only a small rectangular region of the trajectory is used; a greater portion of the bowtie would yield much better velocity and spatial resolution. It might be thought that modifying the readout-gradient waveform can produce a bowtie which offers a larger fraction of itself as a rectangle. I have tried many unsuccessful modifications of the gradient waveform:

(a) changing the amplitude envelope from a constant to various time-variant functions, for example, $1/t$ and $e^{-(|t|)}$,

(b) adding various waveforms such as a time-linear ramp,

(c) changing the frequency of the waveform to various time-variant functions,

(d) changing the repeatable waveform unit from {+A, -A}, where 'A' is the area of one gradient lobe, to other patterns such as {-A, +2A, -A} and {-A, 3A, -3A, +A}.

I believe that none of these modifications worked because of the implications of Eq. 4.4, $dk_v/dk_x = t$. Fundamentally, this equation arises because MRI measures position and then infers velocity from changes in position. Consider two spins which start in the same spatial location but which have different velocities. Differences in velocity can be resolved by waiting for the spins to separate in position. Therefore, the first implication of Eq. 4.4 is that we need longer observation times for better velocity resolution. The second is that, for a trajectory which oscillates about $k_x = 0$, it is impossible to prevent the trajectory from crossing itself and creating one or

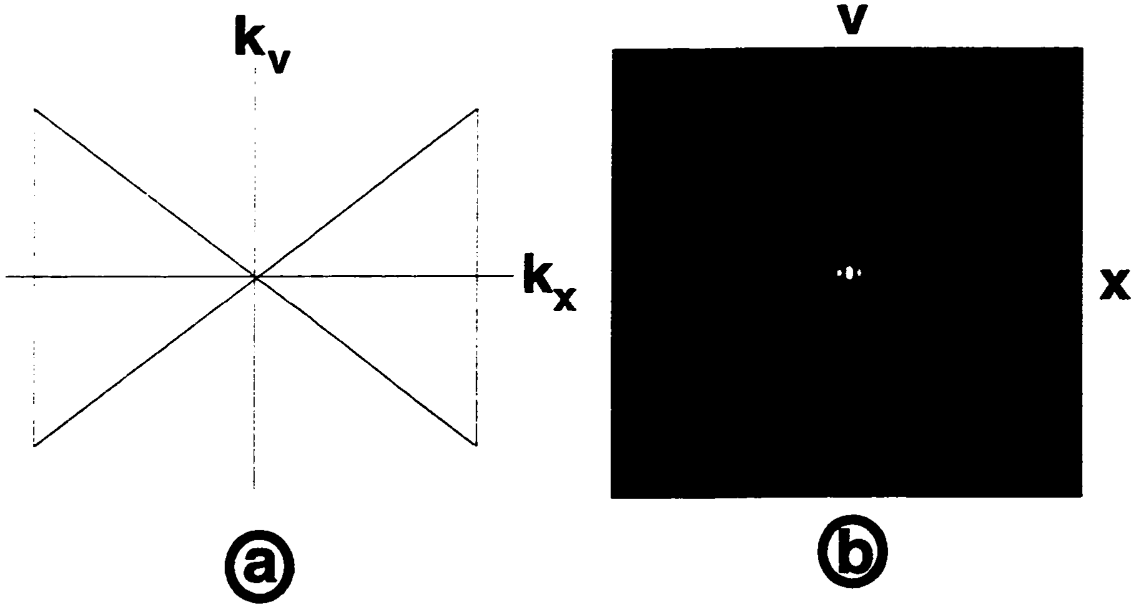

Figure J.1: Impulse response of the entire bowtie trajectory: (a) k-space trajectory, (b) impulse response.

more nodes, even if this k_x oscillation is in an irregular fashion.

It may be interesting to try using portions of the bowtie whose shape is not rectangular. For example, the entire bowtie might be used with the node centered at the k-space origin. For a bowtie where the time origin is chosen to be in the middle of the readout-gradient waveform, the trajectory and impulse response are shown in Fig. J.1. Note that such a trajectory would not be able to image an object whose transform is a vertical bar in k-space, that is, an object which is narrow in v but wide in x.

J.2 Multi-shot bowtie imaging

Bowtie imaging with multiple shots or excitations per image opens up many possibilities. In the discussions below, note that the long axis of the cylindrical excitation is denoted as x and the bowtie trajectory resolves spatial location and velocity along x.

1. Interleaving along k_v can increase the velocity field-of-view, as mentioned in Section 6.3, or can increase the velocity resolution.
2. Phase encoding along k_y and k_z can be used in three ways:
    a. Suppose the main lobe of the cylindrical excitation is thin enough to avoid unwanted signal but the sidelobes are not distant enough. We could phase encode in k_y and k_z using a large FOV and large voxels so that only the central spatial voxel contains the desired signal. If we are imaging the torso, it is conceivable that the sidelobes would only excite material in the left-right direction but not in the anterior-posterior direction. Therefore, we would only have to phase encode in the left-right direction.

b. Suppose the sidelobes of the cylindrical excitation are distant enough to avoid unwanted signal but the main lobe is not wide enough. We could phase encode in k_y and k_z to reduce this unwanted signal. Alternatively, we could use an EPI trajectory for the excitation and make a pulse that is thin in y but wide in z. Then we could just phase encode along k_z.

c. A slice-selective excitation could be used instead of a cylindrical excitation. Phase-encoding along k_y could be used to obtain two spatial dimensions, x and y; in fact, it is necessary otherwise static signal could obscure the flow signal.

3. Phase encoding along the y-velocity direction can yield an image of spatial location in x, velocity in x and velocity in y. In particular, with two excitations, we can do phase-contrast imaging of y velocity.

4. Tiling the k_x-k_v plane can increase the velocity resolution or the spatial resolution. In Fig. J.2a, four bowties provide the shaded rectangular area in k-space. However, the off-resonance properties are not very good as shown in Fig. J.2b.

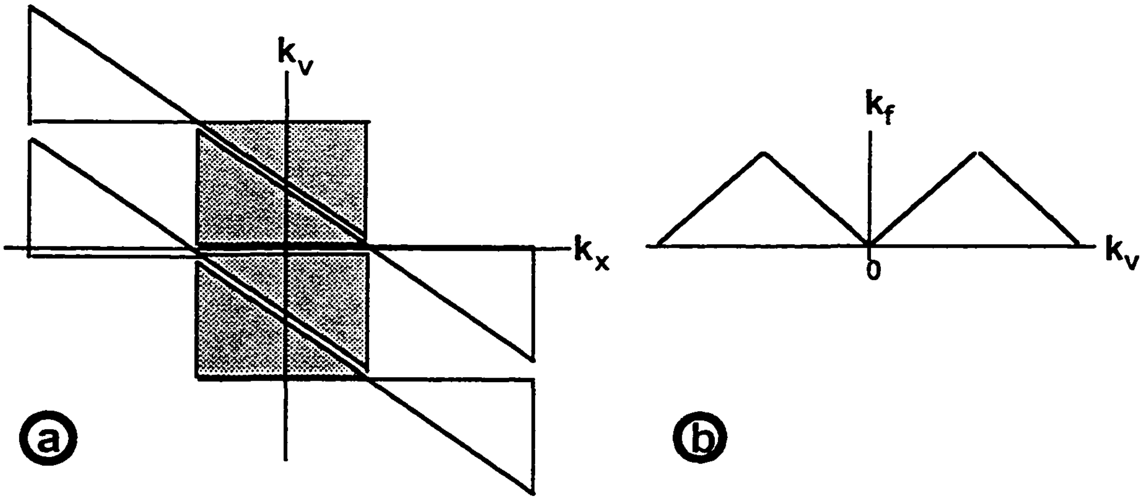

Figure J.2: Four-shot bowtie imaging. An image can be reconstructed using data from the shaded region. (a) k-space trajectory, (b) k_f vs k_v for $k_x = 0$.

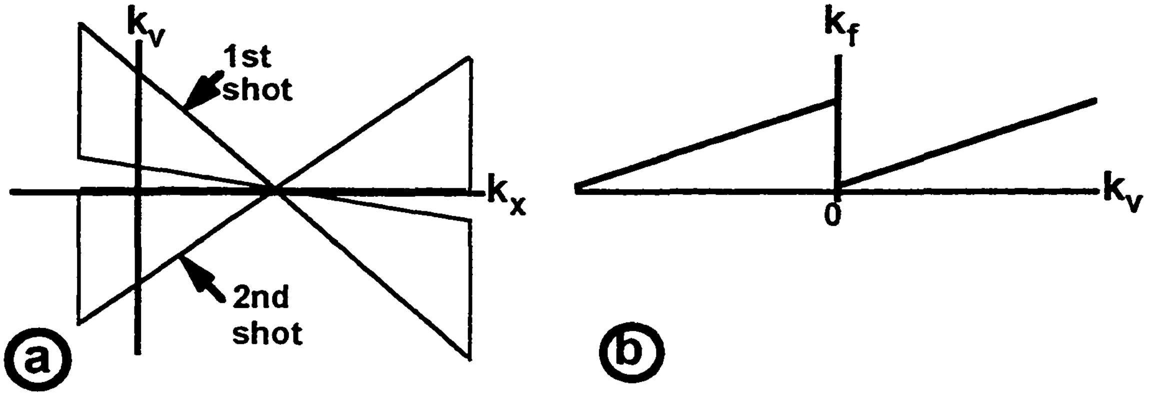

Figure J.3: Two-shot bowtie imaging with the time origin for both shots at the start of the readout-gradient waveform for the second shot: (a) k-space trajectory, (b) k_f vs k_v for $k_x = 0$.

The imaging techniques described above would require either gating or the assumption that the object is quasi-static over multiple excitations. A third possibility is using a single time origin for all shots in a given image. Figure J.3a shows a two-shot image where the time origin for both the first and second shots is at the start of the readout-gradient waveform for the second shot. This means that the first shot is acquired in 'negative time' as explained in Section 4.2.1. Unfortunately, the delay between data-acquisition windows produces a gap in k-space and a discontinuity in the off-resonant phase, as shown in Fig. J.3b.

J.3 Acceleration imaging

It is interesting to consider acceleration imaging which would use the second moment of the readout gradient and, more importantly, whether this would be at all useful when velocity imaging is available. For example, a high velocity with no acceleration would mean steady flow but a high velocity with a high acceleration would imply a jet. I explored two types of acceleration imaging.

Images of acceleration versus position can be made with the bowtie-imaging gradient waveform of Fig. J.4a. A plot of k_a, the second moment of that waveform, versus k_x is shown in Fig. J.4b. This bowtie is similar to the k_x-k_v bowtie except that the vertical spacing between spokes at the left and right edges increases with time. For data-acquisition times of about 20 ms, the acceleration resolution is about 2,000 cm/s^2 and the acceleration field-of-view is about 60,000 cm/s^2. For a healthy person, the velocity in the aorta rises from about 10 m/s to about 150 m/s in about 0.1 sec, giving an acceleration of 1,400 cm/s^2. For severe aortic-stenotic-jet velocities approaching 6000 cm/s [51], the acceleration is presumably 6000/0.1 = 60,000 cm/s^2. Therefore, the current values of acceleration resolution seem to be capable of revealing severe disease. One issue with this technique is whether accelerating spins will remain in the passband of the anti-aliasing filter for a sufficiently long time. Another issue is the effect of the first moment which is now treated as producing spurious phase.

Images of acceleration versus velocity can be made by multiplying the

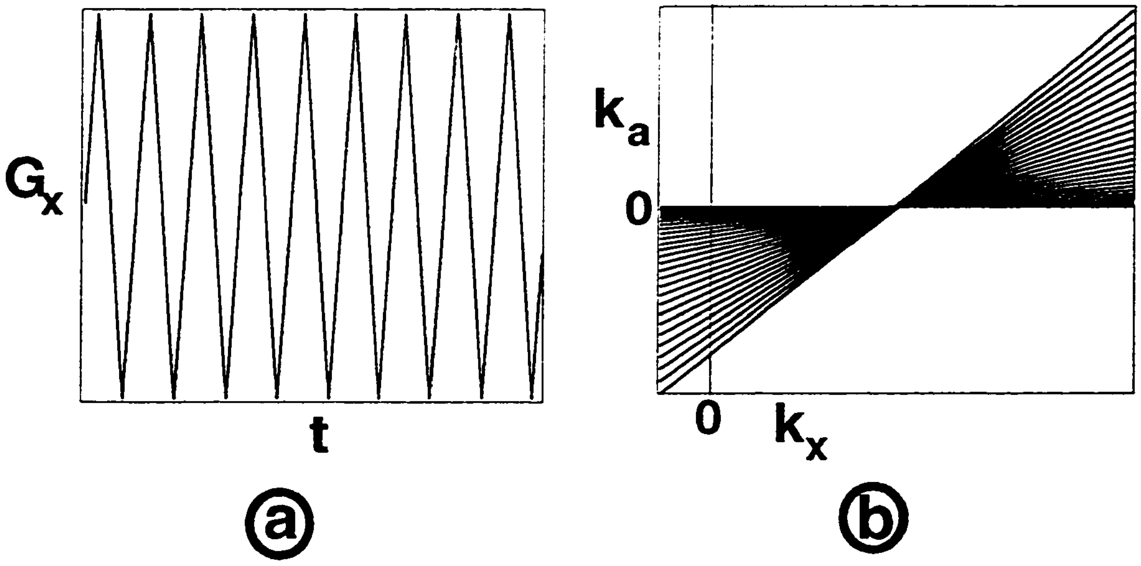

Figure J.4: Making images of acceleration vs. position: (a) 20-ms gradient waveform of which only 6 ms is shown (b) k_a vs. k_x.

gradient waveform in Fig. J.4a by $1/t$,. This would produce a k_v-k_a bowtie with uniform vertical spacing at its left and right edges: similar to the k_x-k_v bowtie produced by the gradient waveform in Fig. J.4a. A major concern for this technique is the reduced velocity resolution resulting from the $1/t$ multiplication. Another concern is the effect of the spurious phase produced by the zeroth moment.

J.4 Imaging two velocity directions

For simultaneously imaging velocity in the x and y directions, I was fascinated by experiments with two simultaneously oscillating gradient waveforms, one on the G_x axis and one on the G_y axis. Unfortunately, I found no practical use for this because the four-dimensional space is unwieldy. Nevertheless, I will present a few thoughts. Let velocity in the x direction be denoted as v and velocity in the y direction be denoted as u.

The gradient waveforms in Fig. J.5a traverse a circle in k_x-k_y space as shown in Fig. J.5b and, more interestingly, a spiral of reasonably uniform density in k_v-k_u space as shown in Fig. J.5c. To first order, we can say that a spiral in k_v-k_u space is achieved by multiplying the waveforms that produce a spiral in k_x-k_y space by $1/t$. There are several possibilities for such waveforms.

1. An image can be made in x-y-v-u space. However, it is difficult to visualize the four-dimensional k-space trajectory, one method is to inspect three of the four dimensions as shown in Figs. J.5d-e. Therefore, it is difficult to position interleaves to fill a desired region in that space; one candidate is to fill a region in k_x-k_y space with overlapping circles. A

larger obstacle to this four-dimensional imaging is the need for even longer scan times than in three-dimensional imaging.

2. An image can be made using only the k_v-k_u trajectory while ignoring the k_x-k_y trajectory. This is the dual of anatomical imaging where we use only the k_x-k_y trajectory and ignore the k_v-k_u trajectory. Since this is perilous for large values of x and y, a pencil excitation can be used with its long axis in the z direction.
3. An image can be made using only the k_y-k_v trajectory shown in Fig. J.5f while ignoring the k_x-k_u trajectorythe k_y-k_v trajectory. Note that we are considering spatial location along y and velocity along x. The k_y-k_v trajectory nicely samples an ellipse in that space. The biggest problem with this technique is that velocity along x also produces spatial displacement along y, resulting in spurious k_x phase. However, there may be a situation where this is not a concern.
4. Spatial resolution may be added to Possibility 2 by considering the dual of phase-contrast imaging. In phase-contrast imaging, we fully resolve spatial location and assume a single velocity per spatial location. This is achieved by fully acquiring a region in k_x-k_y space at two k_v locations. The phase difference between the two k_v locations gives an estimate of velocity. In the dual of phase-contrast imaging, we fully resolve velocity and assume a single spatial location per velocity. This might be achieved using the gradient waveforms of Fig. J.5a in the following way. Acquire two k_v-k_u spirals, each one with a k_x-k_y circle in a different k_x-k_y location. The difference in phase should give an estimate of the spatial location. Alternatively, the k_x-k_y trajectory can be ignored and G_x lobes can be used to encode x location.

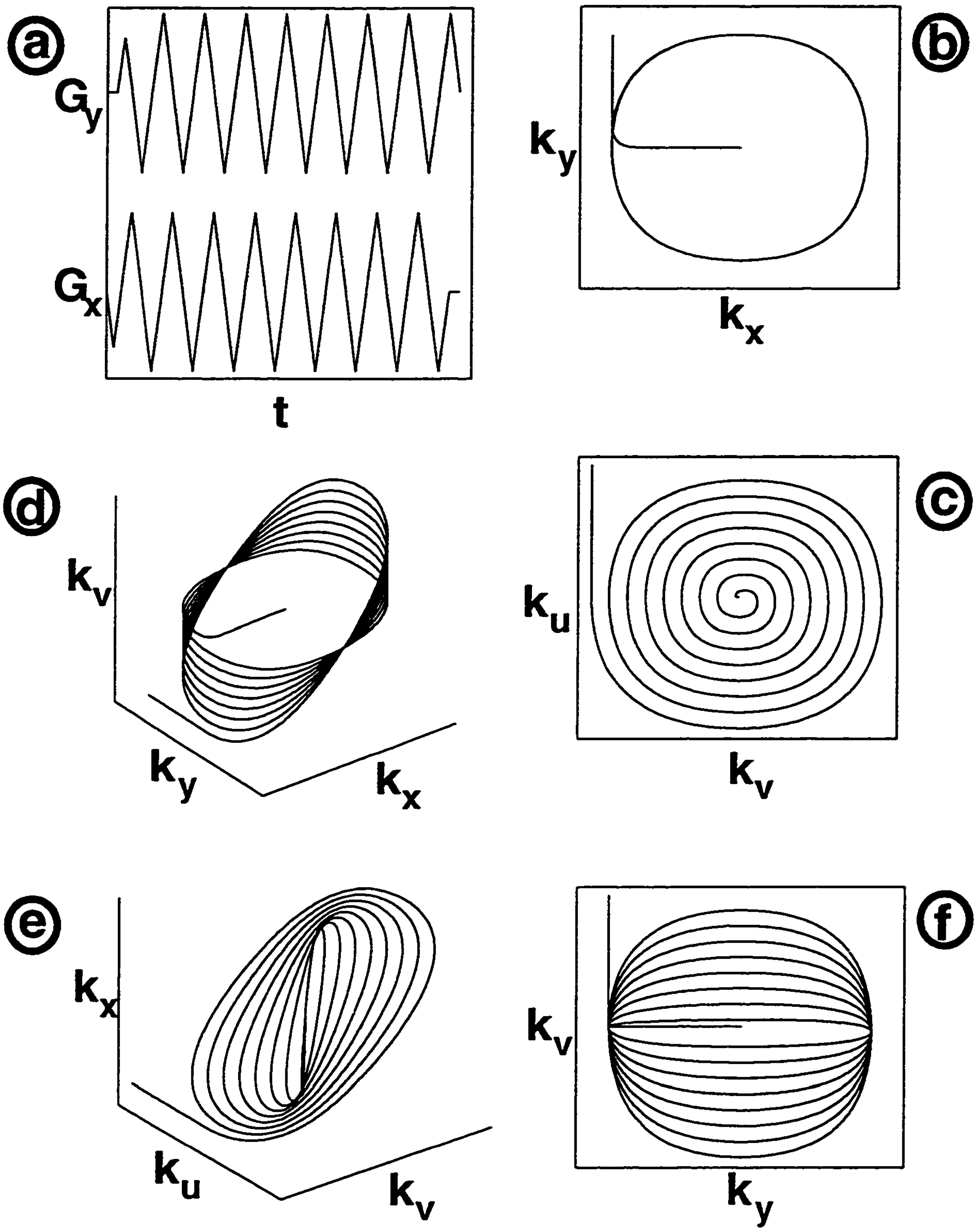

Figure J.5: Imaging two velocity directions: (a) gradient waveforms, (b) k_x-k_y trajectory, (c) k_v-k_u trajectory, (d) k_x-k_y-k_v trajectory, (e) k_v-k_u-k_x trajectory, (e) k_y-k_v trajectory.

Bibliography

1. "1997 Heart and Stroke Statistical Update," American Heart Association, Dallas, Texas, 1997.
2. R. A. Bell, Economics of MRI technology. *J. Magn. Reson. Imaging* **1**, 10-25 (1996).
3. R. N. Bracewell, "The Fourier Transform and Its Applications," 2nd ed., McGraw Hill, 1986.
4. G. T. Luk Pat, C. H. Meyer, J. M. Pauly, D. G. Nishimura, Reducing flow artifacts in echo-planar imaging. *Magn. Reson. Med.* 37, 436-447 (1997).
5. G. T. Luk Pat, J. M. Pauly, B. S. Hu, D. G. Nishimura, One-shot spatially-resolved velocity imaging. *Magn. Reson. Med.* (accepted for publication, March, 1998).
6. G. T. Luk Pat, G. E. Gold, E. W. Olcott, B. S. Hu, D. G. Nishimura, High-resolution three-dimensional *in-vivo* imaging of atherosclerotic plaque. *Magn. Reson. Med.* (submitted for publication, September, 1998).
7. W. F. Block, "Fast T_2-weighted abdominal magnetic resonance imaging," Ph. D. thesis, Stanford University, 1998.
8. A. B. Kerr, "Real-time interactive magnetic resonance imaging," Ph. D. thesis, Stanford University, 1998.

9. D. G. Nishimura, "Principles of Magnetic Resonance Imaging," *text in preparation,* 1996.
10. E. M. Purcell, H. C. Torrey, R. V. Pound, Resonance absorption by nulcear magnetic moments in a solid. *Phys. Rev.* **69**, 37-38 (1946).
11. F. Bloch, Nuclear induction. *Phys. Rev.* **70**, 460-473 (1946).
12. P. C. Lauterbur, Image formation by induced local interactions: Examples employing nuclear magnetic resonance. *Nature* **242**, 190-191 (1983).
13. A. Kumar, D. Welti, R. Ernst, NMR Fourier zeugmatography. *J. Magn. Reson.* **18**, 69-83 (1975).
14. A. C. Melissinos, "Experiments in Modern Physics," Academic Press, Inc., San Diego, California, 1966, pp. 351-357.
15. D. B. Twieg, The k-trajectory formulation of the NMR imaging process with applications in analysis and synthesis of imaging methods. *Med. Phys.* **10**, 610-621 (1983).
16. S. Ljunggren, A simple graphical representation of Fourier-based imaging methods. *J. Magn. Reson.* **54**, 338-343 (1983).
17. A. N. Garroway, P. K. Grannell, P. Mansfield, Image formation in NMR by a selective irradiative. *J. Phys. C* **7**, L457-L462 (1974).
18. D. Hoult, The solution of the Bloch equations in the presence of a varying B_1 field - An approach to selective pulse analysis. *J. Magn. Reson. Imaging* **35**, 69-86 (1979).
19. J. Pauly, D. Nishimura, A. Macovski, A *k*-space analysis of small-tip-angle excitation. *J. Magn. Reson.* **81**, 43-56 (1989).
20. G. Fürst, M. Sitzer, M. Hofer, H. Steinmetz, T. Hackländer, E. Müller, U. Mödder, Quantification of carotid blood flow velocity using MR phase mapping. *J. Comput. Assist. Tomogr.* **18**, 688-696 (1994).

21. G. R. Caputo, C. B. Higgins, Magnetic resonance angiography and measurement of blood flow in the peripheral vessels. *Invest. Radiol.* **27,** S98-S102 (1992).

22. D. G. Nishimura, P. Irarrazabal, C. H. Meyer, A velocity *k*-space analysis of flow effects in echo-planar and spiral imaging. *Magn. Reson. Med.* **33,** 549-556 (1995).

23. A. Macovski, Noise in MRI. *Magn. Reson. Med.* **36,** 494-497 (1996).

24. E. Hahn, Spin echoes. *Phys. Rev.* **80,** 580-594 (1950).

25. P. Mansfield, Multi-planar image formation using NMR spin echoes. *J. Phys. C* **10,** L55-L58 (1977).

26. G. Johnson, J. M. S. Hutchison, The limitations of NMR recalled-echo imaging techniques. *J. Magn. Reson.* **63,** 14-30 (1985).

27. Z. H. Cho, C. B. Ahn, J. H. Kim, Y. E. Lee, C. W. Mun, Phase error corrected interlaced echo planar imaging, *in* "Proc., SMRM, 6th Annual Meeting, New York, 1987," p. 912.

28. R. R. Rzedzian, MESH: A new approach to fast SE imaging. *Magn. Reson. Imaging* **6 (Supl. 1),** 25 (abstr. P50) (1988).

29. F. Farzaneh, S. J. Riederer, J. K. Maier, R. Vavrek, View-interleaved EPI on a commercial scanner, *in* "Proc., SMRM, 8th Annual Meeting, Amsterdam, 1989," p. 832.

30. F. Farzaneh, S. J. Riederer, Hybrid imaging with gradient-recalled sliding echos. *Magn. Reson. Imaging* **7 (Supl. 1),** 70 (abstr. 407) (1989).

31. C. D. Eccles, S. Crozier, W. Roffman, D. M. Doddrell, P. Back, P. T. Callaghan, Practical aspects of shielded gradient-coil design for localised in vivo NMR spectroscopy and small-scale imaging. *Magn. Reson. Imaging* **12,** 621-630 (1994).

32. D. N. Firmin, R. H. Klipstein, G. L. Hounsfield, M. P. Paley, D. B. Longmore, Echo-planar high-resolution flow velocity mapping. *Magn. Reson. Med.* **12**, 316-327 (1989).

33. R. M. Weisskoff, A. P. Crawley, V. Wedeen, Flow sensitivity and flow compensation in instant imaging, *in* "Proc., SMRM, 9th Annual Meeting, New York, 1990," p. 398.

34. K. Butts, S. J. Riederer, Analysis of flow effects in echo-planar imaging. *J. Magn. Reson. Imaging* **2**, 285-293 (1992).

35. J. L. Duerk, O. P. Simonetti, Theoretical aspects of motion sensitivity and compensation in echo-planar imaging. *J. Magn. Reson. Imaging* **1**, 643-650 (1991).

36. G. Cao, D. L. Parker, D. S. Sherrill, Y. P. Du, Abbreviated moment-compensated phase encoding. *Magn. Reson. Med.* **34**, 179-185 (1995).

37. G. C. McKinnon, Ultrafast interleaved gradient-echo-planar imaging on a standard scanner. *Magn. Reson. Med.* **30**, 609-616 (1993).

38. G. McGibney, M. R. Smith, S. T. Nichols, A. Crawley, Quantitative evaluation of several partial-Fourier reconstruction algorithms used in MRI. *Magn. Reson. Med.* **30**, 51-59 (1993).

39. R. J. Ordidge, A. Howseman, R. Coxon, R. Turner, B. Chapman, P. Glover, M. Stehling, P. Mansfield, Snapshot imaging at 0.5 T using echo-planar techniques. *Magn. Reson. Med.* **10**, 227-240 (1989).

40. F. Farzaneh, S. J. Riederer, N. J. Pelc, Analysis of T2 limitations and off-resonance effects on spatial resolution and artifacts in echo-planar imaging. *Magn. Reson. Med.* **14**, 123-139 (1990).

41. K. Sekihara, H. Kohno, Image restoration from nonuniform static field influence in modified echo-planar imaging. *Med. Phys.* **14**, 1087-1089 (1987).

42. D. C. Noll, C. H. Meyer, J. M. Pauly, D. G. Nishimura, A. Macovski, A homogeneity correction method for magnetic resonance imaging with time-varying gradients. *IEEE Trans. Med. Imaging* **10**, 629-637 (1991).
43. G. T. Luk Pat, A. B. Kerr, D. G. Nishimura, Inhomogeneity correction for echo-planar imaging with a polynomial estimate of the field map, *in* "Proc., SMR, 3rd Annual Meeting, Nice, 1995," p. 617.
44. K. F. King, T. K. F. Foo, C. R. Crawford, Optimized gradient waveforms for spiral scanning. *Magn. Reson. Med.* **34**, 156-160 (1995).
45. J. I. Jackson, C. H. Meyer, D. G. Nishimura, A. Macovski, Selection of a convolution function for Fourier inversion using gridding. *IEEE Trans. Med. Imaging* **10**, 473-478 (1991).
46. C. H. Meyer, J. M. Pauly, A. Macovski, D. G. Nishimura, Simultaneous spatial and spectral selective excitation. *Magn. Reson. Med.* **15**, 287-304 (1990).
47. Y. Zur, M. L. Wood, L. J. Neuringer, Spoiling of transverse magnetization in steady-state sequences. *Magn. Reson. Med.* **21**, 251-263 (1991).
48. H. Bruder, H. Fischer, H. E. Reinfelder, F. Schmitt, Image reconstruction for echo planar imaging with nonequidistant *k*-space sampling. *Magn. Reson. Med.* **23**, 311-323 (1992).
49. D. A. Feinberg, R. Turner, P. D. Jakab, M. von Kienlin, Echo-planar imaging with asymmetric gradient modulation and inner-volume excitation. *Magn. Reson. Med.* **13**, 162-169 (1990).
50. S. A. Rebergen, E. E. van der Wall, J. Doornbos, A. de Roos, Magnetic resonance measurement of velocity and flow: Technique, validation, and cardiovascular applications. *Am. Heart J.* **126**, 1439-1456 (1993).

51. P. J. Kilner, D. N. Firmin, R. S. O. Rees, J. Martinez, D. J. Pennell, R. H. Mohiaddin, S. R. Underwood, D. B. Longmore, Valve and great vessel stenosis: Assessment with MR jet velocity mapping. *Radiology* **178,** 229-235 (1992).
52. R. H. Mohiaddin, M. Amanuma, P. J. Kilner, D. J. Pennell, C. Manzara, D. B. Longmore, MR phase-shift velocity mapping of mitral and pulmonary venous flow. *J. Comput. Assist. Tomogr.* **15,** 237-243 (1991).
53. M. A. Galjee, A. C. Van Rossum, M. Hofman, F. C. Visser, J. Valk, Correlation of hemodynamic parameters and pulmonary venous flow in mitral regurgitation measured by magnetic resonance velocity mapping, *in* "Proc., SMRM, 11th Annual Meeting, Berlin, 1992," p. 2508.
54. M. Koch, S. E. Maier, I. Baumgartner, K. D. Hagspiel, C. von Weymarn, P. Boesiger, A. Bollinger, G. K. von Schulthess, Magnetic resonance angiography and flow quantification in peripheral vessel disease before and after percutaneous transluminal angioplasty (PTA), *in* "Proc., SMRM, 10th Annual Meeting, San Francisco, 1991," p. 137.
55. P. R. Moran, A flow velocity zeugmatographic interlace for NMR imaging in humans. *Magn. Reson. Imag.* **1,** 197-203 (1982).
56. T. W. Redpath, D. G. Norris, R. A. Jones, J. M. S. Hutchison, A new method of NMR flow imaging. *Phys. Med. Biol.* **29,** 891-898 (1984).
57. C. Dumoulin, S. P. Souza, C. J. Hardy, S. A. Ash, Quantitative measurement of blood flow using cylindrically localized Fourier velocity encoding. *Magn. Reson. Med.* **21,** 242-250 (1991).
58. P. van Dijk, Direct cardiac NMR imaging of heart wall and blood flow velocity. *J. Comput. Assist. Tomogr.* **8,** 429-436 (1984).

59. D. J. Bryant, J. A. Payne, D. N. Firmin, D. B. Longmore, Measurement of flow with NMR imaging using a gradient pulse and phase difference technique. *J. Comput. Assist. Tomogr.* **8**, 588-593 (1984).

60. J. D. Pearlman, J. R. Moore, M. J. Lizak, Real-time NMR beam-directed velocity mapping: V-mode NMR. *Circulation* **86**, 1433-1438 (1992).

61. M. O'Donnell, NMR blood flow imaging using multiecho, phase contrast sequences. *Med. Phys.* **12**, 59-64 (1985).

62. K. Butts, N. J. Hangiandreou, S. J. Riederer, Phase velocity mapping with a real time line scan technique. *Magn. Reson. Med.* **29**, 134-138 (1993).

63. B. S. Hu, J. M. Pauly, D. G. Nishimura, Localized real-time velocity spectra determination. *Magn. Reson. Med.* **30**, 393-398 (1993).

64. P. Irarrazabal, B. S. Hu, J. M. Pauly, D. G. Nishimura, Spatially resolved and localized real-time velocity distribution. *Magn. Reson. Med.* **30**, 207-212 (1993).

65. D. G. Nishimura, J. I. Jackson, J. M. Pauly, On the nature and reduction of the displacement artifact in flow images. *Magn. Reson. Med.* **22**, 481-492 (1991).

66. G. R. Crelier, K. P. Prüssmann, P. Boesiger, Numerical simulation of 2D-selective excitation pulses in the presence of motion, *in* "Proc., SMR, 3rd Annual Meeting, Nice, 1995," p. 1027.

67. E. Falk, P. K. Shah, V. Fuster, Coronary plaque disruption. *Circulation* **92**, 657-671 (1995).

68. M. C. Fishbein, R. J. Siegel, How big are coronary atherosclerotic plaques that rupture? *Circulation* **94**, 2662-2666 (1996).

69. J. A. Fallavollita, K. Kumar, A. S. Brody, I. L. Bunnell, J. M. Canty, Jr., Detection of coronary artery calcium to differentiate patients with early

coronary atherosclerosis from luminally normal arteries. *Am. J. Cardiol.* **78**, 1281-1284 (1996).

70. N. D. Wong, D. Kouwabunpat, A. N. Vo, R. C. Detrano, H. Eisenberg, M. Goel, J. M. Tobis, Coronary calcium and atherosclerosis by ultrafast computed tomography in asymptomatic men and women: relation to age and risk factors. *Am. Heart J.* **127**, 422-430 (1994).
71. D. E. Gutfinger, C. Y. Leung, T. Hiro, B. Maheswaran, S. Nakamura, R. Detrano, X. Kang, W. Tang, J. M. Tobis, In vitro atherosclerotic plaque and calcium quantitation by intravascular ultrasound and electron-beam computed tomography. *Am. Heart J.* **131**, 899-906 (1996).
72. T. Spencer, M. P. Ramo, D. M. Salter, T. Anderson, P. P. Kearney, G. R. Sutherland, K. A. Fox, W. N. McDicken, Characterisation of atherosclerotic plaque by spectral analysis of intravascular ultrasound: an in vitro methodology. *Ultrasound Med. Biol.* **23**, 191-203 (1997).
73. S. L. Bridal, P. Fornaes, P. Bruneval, G. Berger, Parametric integrated backscatter and attenuation images constructed using backscattered radio frequency signals 25-56 MHz from human aortae in vitro. *Ultrasound Med. Biol.* **23**, 215-229 (1997).
74. L. Kaufman, L. E. Crooks, P. E. Sheldon, W. Rowan, T. Miller, Evaluation of NMR imaging for detection and quantification of obstructions in vessels. *Invest. Radiol.* **17**, 554-560 (1982).
75. R. J. Herfkens, C. B. Higgins, H. Hricak, M. J. Lipton, L. E. Crooks, P. E. Sheldon, L. Kaufman, Nuclear magnetic resonance imaging of atherosclerotic disease. *Radiology* **148**, 161-166 (1983).
76. D. M. Small, Progression and regression of atherosclerotic lesions: insights from lipid biochemistry. *Arteriosclerosis* **8**, 103-129 (1988).

77. H. C. Stary, Evolution and progression of atherosclerotic lesions in coronary arteries of children and young adults. *Arteriosclerosis* 9, I19-I32 (1989).

78. K. Soila, P. Nummi, T. Ekfors, M. Viamonte, M. Kormano, Proton relaxation times in arterial wall and atheromatous lesions in man. *Invest. Radiol.* **20**, 411-415 (1986).

79. C. H. Maynor, H. C. Charles, R. J. Herfkens, S. A. Suddarth, G. A. Johnson, Chemical shift imaging of atherosclerosis at 7.0 Tesla. *Invest. Radiol.* **24**, 52-60 (1988).

80. J. D. Pearlman, J. Zajicek, M. B. Merickel, C. S. Carman, C. R. Ayers, J. R. Brookeman, M. F. Brown, High-resolution 1H NMR spectral signature from human atheroma. *Magn. Reson. Med.* 7, 262-279 (1988).

81. R. H. Mohiaddin, D. N. Firmin, S. R. Underwood, A. K. Abdulla, R. H. Klipstein, R. S. O. Rees, D. B. Longmore, Chemical shift magnetic resonance imaging of human atheroma. *Br. Heart J.* **62**, 81-89 (1989).

82. S. Vinitksi, P. M. Consigny, M. J. Shapiro, N. Janes, S. N. Smullens, M. D. Rifkin, Magnetic resonance chemical shift imaging and spectroscopy of atherosclerotic plaque. *Invest. Radiol.* **26**, 703-714 (1991).

83. G. E. Gold, J. M. Pauly, G. H. Glover, J. C. Moretto, A. Macovski, R. J. Herfkens, Characterization of atherosclerosis with a 1.5-T imaging system. *J. Magn. Reson. Imaging* 3, 399-407 (1993).

84. M. I. Altbach, M. A. Mattingly, M. F. Brown, A. F. Gmitro, Magnetic resonance imaging of lipid deposits in human atheroma via a stimulated-echo diffusion-weighted technique. *Magn. Reson. Med.* **20**, 319-326 (1991).

85. A. J. Martin, A. I. Gotlieb, R. M. Henkelman, High-resolution MR imaging of human arteries. *J. Magn. Reson. Imaging* 5, 93-100 (1995).

86. J. F. Toussaint, J. F. Southern, V. Fuster, H. L. Kantor, T2-weighted contrast for NMR characterization of human atherosclerosis. *Arterioscler. Thromb. Vasc. Biol.* **15**, 1533-1542 (1995).

87. M. B. Merickel, C. S. Carman, J. R. Brookeman, J. P. Mugler, M. F. Brown, C. R. Ayers, Identification and 3-D quantification of atherosclerosis using magnetic resonance imaging. *Comput. Biol. Med.* **18**, 89-102 (1988).

88. M. B. Merickel, S. Berr, K. Spetz, T. R. Jackson, J. Snell, P. Gillies, E. Shimshick, J. Hainer, J. R. Brookeman, C. R. Ayers, Noninvasive quantitative evaluation of atherosclerosis using MRI and image analysis. *Arteriosclerosis and Thrombosis* **13**, 1180-1186 (1993).

89. C. Yuan, J. S. Tsuruda, K. N. Beach, C. E. Hayes, M. S. Ferguson, C. E. Alpers, T. K. Foo, D. E. Strandness, Techniques for high-resolution MR imaging of atherosclerotic plaque. *J. Magn. Reson. Imaging* **4**, 43-49 (1994).

90. M. P. Skinner, C. Yuan, L. Mitsumori, C. E. Hayes, E. W. Raines, J. A. Nelson, R. Ross, Serial magnetic resonance imaging of experimental atherosclerosis detects lesion fine structure, progression and complications in vivo. *Nature Medicine* **1**, 69-73 (1995).

91. C. Yuan, J. W. Murakami, C. E. Hayes, J. S. Tsuruda, T. S. Hatsukami, K. S. Wildy, M. S. Ferguson, D. E. Strandness, Phased-array magnetic resonance imaging of the carotid artery bifurcation: preliminary results in healthy volunteers and a patient with atherosclerotic disease. *J. Magn. Reson. Imaging* **5**, 561-565 (1995).

92. J. F. Toussaint, G. M. LaMuraglia, J. F. Southern, V. Fuster, H. L. Kantor, Magnetic resonance images lipid, fibrous, calcified, hemorrhagic, and thrombotic components of human atherosclerosis in vivo. *Circulation* **94**, 932-938 (1996).

93. G. von Ingerseben, U. P. Schmiedl, T. S. Hatsukami, J. A. Nelson, D. S. Subrmaniam, M. S. Ferguson, C. Yuan, Characterization of atherosclerotic plaques at the carotid bifurcation: correlation of high-resolution MR imaging with histologic analysis - preliminary study. *Radiographics* **17**, 1417-1423 (1997).

94. J. Hennig, A. Nauerth, H. Friedburg, RARE imaging: a fast imaging method for clinical MR. *Magn. Reson. Med.* **3**, 823-833 (1986).

95. J. P. Mugler, J. R. Brookeman, An improved phase-encoding strategy for 3D GRASE, *in* "Proc., SMR, 3rd Annual Meeting, Nice, 1995," p. 479.

96. M. T. Alley, J. M. Pauly, F. G. Sommer, N. J. Pelc, Angiographic imaging with 2D RF pulses. *Magn. Reson. Med.* **37**, 260-267 (1997).

97. K. Oshio, D. A. Feinberg, GRASE (gradient- and spin-echo) imaging: a novel fast MRI technique. *Magn. Reson. Med.* **20**, 344-349 (1991).

98. P. S. Melki, R. V. Mulkern, L. P. Panych, F. A. Jolesz, Comparing the FAISE method with conventional dual-echo sequences. *J. Magn. Reson. Imaging* **1**, 319-326 (1991).

99. D. A. Feinberg, J. C. Hoenninger, L. E. Crooks, L. Kaufman, J. C. Watts, M. Arakawa, Inner volume MR imaging: technical concepts and their application. *Radiology* **156**, 743-747 (1985).

100. P. Mansfield, R. J. Ordidge, R. Coxon, Zonally magnified EPI in real time by NMR. *J. Phys. E* **21**, 275-280 (1988).

101. M. H. Levitt, R. Freeman, Compensation for pulse imperfections in NMR spin-echo experiments. *J. Magn. Reson.* **43**, 65-80 (1981).

102. D. Rosenfeld, S. L. Panfil, Y. Zur, Design of adiabatic pulses for fat-suppression using analytic solutions of the Bloch equation. *Magn. Reson. Med.* **37**, 793-801 (1997).

103. A. Haase, J. Frahm, W. Heanicke, D. Matthaei, 1H NMR chemical shift selective CHESS imaging. *Phys. Med. Biol.* **30**, 341-344 (1985).

104. R. R. Edelman, D. Chien, D. Kim, Fast selective black blood MR imaging. *Radiology* **181**, 655-660 (1991).

105. M. S. Silver, R. I. Joseph, D. I. Hoult, Selective spin inversion in nuclear magnetic resonance and coherent optics through an exact solution of the Bloch-Riccati equation. *Phys. Rev. A* **31**, 2735-2755 (1985).

106. O. P. Simonetti, J. P. Finn, R. D. White, G. Laub, D. A. Henry, "Black blood" T2-weighted inversion-recovery MR imaging of the heart. *Radiology* **199**, 49-57 (1996).

107. R. S. Hinks, R. T. Constable, Gradient moment nulling in fast spin echo. *Magn. Reson. Med.* **32**, 698-706 (1994).

108. D. C. Noll, D. G. Nishimura, A. Macovski, Homodyne detection in magnetic resonance imaging. *IEEE Trans. Med. Imaging* **10**, 154-163 (1991).

109. X. Wan, D. L. Parker, J. N. Lee, H. R. Buswell, G. T. Gullberg, Reduction of phase error ghosting artifacts in thin slice fast spin-echo imaging. *Magn. Reson. Med.* **34**, 632-638 (1995).

110. H. Cox, W. P. Dillon, Low-cost device for avoiding bulk susceptibility artifacts in chemical-selective fat saturation MR of the head and neck. *AJNR* **16**, 1367-1369 (1995).

111. S. Yen, G. Rubin, S. Napel, Fast sliding thin slab volume visualization, *in* "Proc., 1996 Symposium on Volume Visualization, San Francisco, CA, October, 1996," pp. 79-86.

112. G. Wright, "Magnetic resonance relaxation behaviour of blood: study and applications," Ph. D. thesis, Stanford University, 1991, p. 58.

113. D. C. Noll, F. E. Boada, W. F. Eddy, A spectral approach to analyzing slice selection in planar imaging: optimization for through-plane interpolation. *Magn. Reson. Med.* 38, 151-160 (1997).

114. D. Kelley, R. Ordidge, Techniques for phase correction of raw data for EPI with unshielded gradient coils, *in* "Proc., SMRM, 12th Annual Meeting, New York, 1993," p. 1237.

115. A. Jesmanowicz, E. C. Wong, J. S. Hyde, Phase correction for EPI using internal reference lines, *in* "Proc., SMRM, 12th Annual Meeting, New York, 1993," p. 1239.

116. K. F. King, C. R. Crawford, J. K. Maier, Correction for filter-induced ghosts in echo planar imaging, *in* "Proc., SMR, 3rd Annual Meeting, Nice, 1995," p. 105.

117. J. B. Mandeville, R. M. Weisskoff, L. Garrido, Reduction of eddy-current induced Nyquist ghosts and sampling artifact, *in* "Proc., SMR, 3rd Annual Meeting, Nice, 1995," p. 613.

118. X. Hu, T. H. Le, Artifact reduction in EPI with phase-encoded reference scan. *Magn. Reson. Med.* 36, 166-171 (1996).

119. X. Wan, G. T. Gullberg, D. L. Parker, G. L. Zeng, Reduction of geometric and intensity distortions in echo-planar imaging using a multireference scan. *Magn. Reson. Med.* 37, 932-944 (1997).

120. A. Takahashi, T. Peters, Compensation of multi-dimensional selective excitaiton pulses using measured *k*-space trajectories. *Magn. Reson. Med.* 34, 446-456 (1995).

121. A. Kerr, J. Pauly, D. Nishimura, Gradient measurement and characterization for spiral and echo-planar sequences, *in* "Proc., SMR, 4th Annual Meeting, New York, 1996," p. 364.

122. X. Zhou, G. P. Cofer, R. S. Hinks, J. R. MacFall, G. A. Johnson, On phase artifacts of high-field fast spin-echo images, *in* "Proc., SMRM, 12th Annual Meeting, New York, 1993," p. 1248.

123. D. A. Steinman, B. K. Rutt, On the nature and reduction of plaque-mimicking flow artifacts in black blood MRI of the carotid bifurcation. *Magn. Reson. Med.* **39**, 635-641 (1998).

124. R. L. Vanninen, H. I. Manninen, P. L. K. Partanen, P. A. Vainio, S. Soimakallio, Carotid artery stenosis: clinical efficacy of MR phase-contrast flow quantification as an adjunct to MR angiography. *Radiology* **194**, 459-467 (1995).

125. W. F. Ganong, "Review of Medical Physiology," 12th ed., Lange Medical Publications, Los Altos, California, 1985, pp. 461-462.

126. A. Macovski, C. Meyer, A novel fast-scanning system, *in* "Proc., SMRM, 5th Annual Meeting, Montreal, 1986," pp. 156-157 (Works in Progress).

IMAGE EVALUATION TEST TARGET (QA-3)

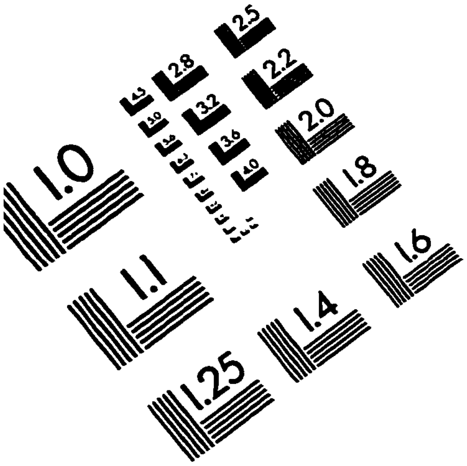

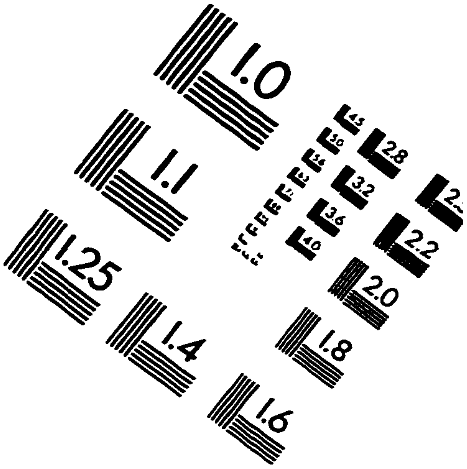

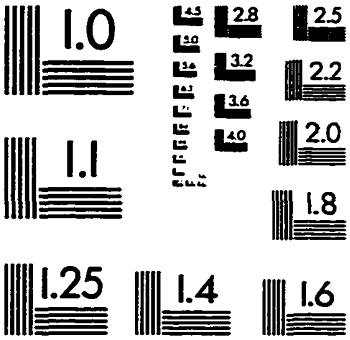

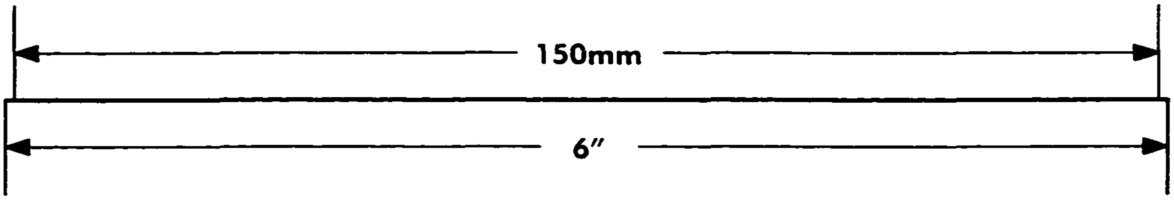

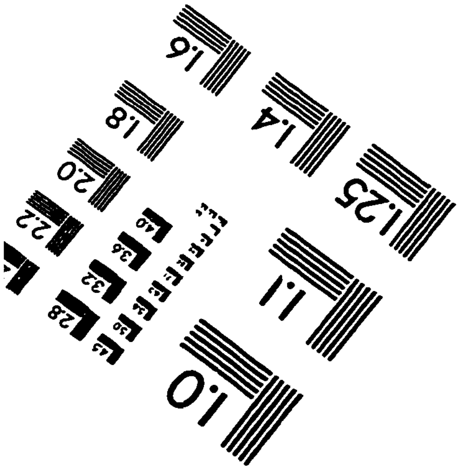

APPLIED IMAGE . Inc
1653 East Main Street
Rochester, NY 14609 USA
Phone: 716/482-0300
Fax: 716/288-5989